Emplacement conditions and exhumation of the Varvarco Tonalite and associated plutons from the Cordillera del Viento, Southern Central Andes

Journal:	*Geological Magazine*
Manuscript ID	GEO-21-2745.R2
Manuscript Type:	Original Article
Date Submitted by the Author:	n/a
Complete List of Authors:	Assis, Omar; Universidade de Brasilia, Instituto de Geociências Zaffarana, Claudia; Universidad Nacional de Río Negro, Instituto de Investigación en Paleobiología y Geología (IIPG-CONICET) Orts, Darío; Universidad Nacional de Rio Negro, Instituto de Investigación en Paleobiología y Geología (IIPG-CONICET) Puigdomenech Negre, Carla; Consejo Nacional de Investigaciones Cientificas y Tecnicas Ruiz González, Víctor; Consejo Nacional de Investigaciones Cientificas y Tecnicas, Gallastegui, Gloria; IGME, Oficina regional Oviedo Hauser, Natalia; Universidade de Brasilia, Instituto de Geociências Molina , JF ; Universidad de Granada , Mineralogy and Petrology Pernich, Sebastian; Universidad Nacional de Río Negro, Instituto de Investigación en Paleobiología y Geología (IIPG-CONICET)
Keywords:	granitoids, Andean orogeny, AMS, fission track dating, fast exhumation rate
Abstract:	During the Late Cretaceous Andean orogeny, the compressive deformation associated with the shallowing of the subducting slab caused the development of the arc-related igneous rocks known as the Naunauco Belt. This study presents petrographic, mineralogical, and anisotropy of magnetic susceptibility (AMS) data of the Varvarco Intrusives (the Varvarco Tonalite, Butalón Tonalite and Radales Aplite), which crop out in the Cordillera del Viento, Neuquén Province, Argentina. The assembly of plutons was formed by mafic magma episodic injection. Amphibole and biotite compositions suggest that the Varvarco Tonalite is related to calc-alkaline, I-type magmas, typical of subduction environments. Different geothermobarometers based on amphibole and plagioclase compositions on the Varvarco Tonalite suggest shallow emplacement conditions (~2-3 kbar, equivalent to ~12 km depth). Apatite fission track analyses give exhumation ages of 67.5 ± 8 Ma for the Varvarco Tonalite and 50.3 ± 5.9 Ma for the Butalón Tonalite. A calculated continuous fast exhumation rate of at least 330 °C/My is consistent with the shallow emplacement conditions, textural data and geobarometric estimations. In agreement with thermal profile, the magmatic system was exhumed by ~12 km within ca. 2.1 Ma implying a geothermal gradient of ~62.5 °C/km. The last step of exhumation occurred between ~65.3 Ma and 56.9 Ma. The magmatic fabrics observed in the studied plutons reflect mostly magma chamber processes. The Varvarco Intrusives represent satellite calc-alkaline plutons of the North Patagonian Batholith which were emplaced syn- to post-tectonically with respect to a major deformation stage of the Southern Central Andes.

Emplacement conditions and exhumation of the Varvarco Tonalite and associated plutons from the Cordillera del Viento, Southern Central Andes

Short title: Emplacement and exhumation of the Cordillera del Viento plutons

Category: Original Articles

Omar Sebastian ASSIS[1]*, Claudia Beatriz ZAFFARANA[2], Darío ORTS[2], Carla PUIGDOMENECH[3], Víctor RUIZ GONZÁLEZ[3], Gloria GALLASTEGUI[4], Natalia HAUSER[1], Ekaterina S. KISEEVA[5], José Francisco MOLINA[6] and Sebastián PERNICH[2]

[1]Instituto de Geociências, Universidade de Brasília, Laboratório de Geocronologia e geoquímica isotópica, Brasília, 70910 900, DF, Brasil.

[2]Universidad Nacional de Río Negro, Sede Alto Valle-Valle Medio, General Roca e Instituto de Investigación en Paleobiología y Geología (IIPG-CONICET).

[3]Instituto de Geociencias Básicas, Aplicadas y Ambientales de Buenos Aires (IGeBA); CONICET; Universidad de Buenos Aires.

[4]Instituto Geológico y Minero de España (IGME, CSIC), España.

[5] School of Biological, Earth and Environmental Sciences, University College Cork, Distillery Fields, North Mall, Cork, Ireland

[6]Departamento de Mineralogía y Petrología, Universidad de Granada, España.

*Corresponding author; E-mail: seba_assis@outlook.com, sebaoassis@gmail.com

Abstract

During the Late Cretaceous Andean orogeny, the compressive deformation associated with the shallowing of the subducting slab caused the development of the arc-related igneous rocks known as the Naunauco Belt. This study presents petrographic, mineralogical, and anisotropy of magnetic susceptibility (AMS) data of the Varvarco Intrusives (the Varvarco Tonalite, Butalón Tonalite and Radales Aplite), which crop out in the Cordillera del Viento, Neuquén Province, Argentina. The assembly of plutons was formed by mafic magma episodic injection. Amphibole and biotite compositions suggest that the Varvarco Tonalite is related to calc-alkaline, I-type magmas, typical of subduction environments. Different geothermobarometers based on amphibole and plagioclase compositions on the Varvarco Tonalite suggest shallow emplacement conditions (~2-3 kbar, equivalent to ~12 km depth). Apatite fission track analyses give exhumation ages of 67.5 ± 8 Ma for the Varvarco Tonalite and 50.3 ± 5.9 Ma for the Butalón Tonalite. A calculated continuous fast exhumation rate of at least 330 °C/My is consistent with the shallow emplacement conditions, textural data and geobarometric estimations. In agreement with thermal profile, the magmatic system was exhumed by ~12 km within ca. 2.1 Ma implying a geothermal gradient of ~62.5 °C/km. The last step of exhumation occurred between ~65.3 Ma and 56.9 Ma. The magmatic fabrics observed in the studied plutons reflect mostly magma chamber processes. The Varvarco Intrusives represent satellite calc-alkaline plutons of the North Patagonian Batholith which were emplaced syn- to post-tectonically with respect to a major deformation stage of the Southern Central Andes.

Keywords: granitoids, Andean orogeny, AMS, fission track dating, fast exhumation rate.

1. Introduction

Cordilleran batholiths are large magmatic bodies that result from the accumulation of many smaller plutons, spatially and chemically associated, which may or may not be temporally related. Most of these batholiths are composed of granodiorite and tonalite, such as the Sierra Nevada Batholith (Bateman & Eaton, 1967) and the North Patagonian Batholith (Ramos *et al*. 1982). The Patagonian Batholith represents a large granite intrusive complex that extends from 39º to 56º S, and is mainly composed of tonalites (Ramos *et al*. 1982). The main peak of intrusion relates to the development of the North Patagonian Batholith formed in Early Cretaceous, between 136 and 127 Ma (Pankhurst *et al*. 1999; Hervé *et al*. 2007), slightly before the onset of Late Cretaceous compression coeval with the Neuquén foreland basin development (Ramos, 1999). In addition, in Late Cretaceous-Paleogene, the magmatic arc was expanded into the retroarc region, including the present-day Cordillera del Viento range, by the intrusion of satellite igneous bodies at 130-150 km east of the present arc trend (Hervé *et al*. 2007; Fig. 1).

Here, we study the internal structure of some of these satellite igneous bodies, the Varvarco Intrusives (Varvarco Tonalite, Radales Aplite and Butalón Tonalite) that are exposed in the Varvarco-Butalón region in the Cordillera del Viento (Neuquén Andes, Fig. 1 and 2a). We applied the anisotropy of magnetic susceptibility (AMS) method, combined with petrographic and mineral chemistry data to define magmatic structures and, thus, to infer magma emplacement mechanisms. The AMS method has been proven to be a very useful tool to study the internal structure of weakly foliated bodies (e.g., Archanjo *et al*. 1995, 2002; de Saint Blanquat & Tikoff, 1997; Ferré & Améglio, 2000; McNulty *et al*. 2000; Neves *et al*. 2003; Žák *et al*. 2005; D'Eramo *et al*. 2006; Stevenson, 2009; Somoza *et al*. 2015; Nédélec &

Bouchez, 2015; Olivier *et al*. 2016; Zaffarana *et al*. 2017). In particular, the AMS method is relevant for the resolution of magmatic lineations, which are generally hard to measure in the field. The interpretation of the internal structure of plutons and their relationship with the country rock may be classified into three main types: reflecting internal magma chamber, regional deformation processes (Paterson *et al*. 1998), or a combination of both.

The timing of intrusion with respect to the exhumation of the Varvarco Tonalite and the Butalón Tonalite was also investigated by obtaining apatite fission track ages for these intrusives. Crustal thickness estimates at the time of magma generation were aided by geochemical data (mineral chemistry for amphibole, plagioclase, and biotite), with the aim of developing a model for emplacement and exhumation of the Varvarco Tonalite. Mineral compositions were used to constrain magma chamber temperature and depth through geothermobarometric analysis (Hammarstrom & Zen 1986; Hollister *et al*. 1987; Johnson & Rutherford 1989; Schmidt 1992; Holland & Blundy 1994; Anderson & Smith 1995; Ridolfi *et al*. 2010; Ridolfi & Renzulli 2012; Putirka 2016; Molina *et al*. 2015; 2021). The combination of these methods allows us to unravel the history of Varvarco satellite intrusives, from their emplacement to fast exhumation during the Late Cretaceous-Paleogene times of the Andean orogeny.

2. Geological and structural framework

The three plutons investigated in this work: the Varvarco Tonalite, the Butalón Tonalite, and the Radales Aplite, are located in the Varvarco and Butalón areas (Fig. 2a) and were originally named by Pesce (1981) as Varvarco Intrusives. They were later attributed to the Colipilli Formation (Franchini *et al*. 2003; Kay *et al*. 2006; Casé *et al*. 2008), the intrusive

part of the volcanic and plutonic Late Cretaceous Naunauco Belt (Llambías & Malvicini 1978; Zamora Valcarce *et al*. 2011).

Pesce (1981) had originally described the Varvarco pluton as a granodiorite body, but the average modal composition that we found in all our sites is more compatible with a tonalitic intrusive. Therefore, we renamed this pluton as Varvarco Tonalite. In the same way, the Radales Granite (Zanettini *et al*. 2001) is renamed here as Radales Aplite because its general texture is aplitic, typical of subvolcanic igneous bodies.

The Varvarco Tonalite has a K-Ar cooling age (whole-rock) of 64.7 ± 3.2 Ma (J.I.C.A./M.M.A.J., 2000 in Franchini *et al*. 2003), and an ^{40}Ar-^{39}Ar cooling age for biotite of 69.09 ± 0.13 Ma (Kay *et al*. 2006). A U-Pb SHRIMP zircon age of 67.8 ± 0.8 Ma was thoroughly documented by Assis (2019); thus the crystallisation age of Varvarco Tonalite coincides with the K-Ar cooling age. The geochemistry of the Butalón Tonalite was studied by Casé *et al*. (2008), who indicated these igneous rocks are meta- to peraluminous calc-alkaline with low to medium K_2O content, coincidental with I-type granitoids like other granitoids in the area (e.g., Cerro Nevazón; Franchini *et al*. 2003). The Radales Aplite is a granophyric granite intruding the Varvarco Tonalite (Zanettini *et al*. 2001). The Au-Ag veins which are intruding the Radales Aplite and Permian and Jurassic rocks were dated by the ^{40}Ar-^{39}Ar stepwise method in adularia and yielded the age of 65.68 ± 0.22 Ma (Zappettini *et al*. 2014). These ^{40}Ar-^{39}Ar data indicate that break between the emplacement of Varvarco Tonalite and the intrusion of the Radales Aplite was short.

The Varvarco Intrusives crop out in the Cordillera del Viento range in the Neuquén Andes of southwestern Argentina, which is a structurally complex area, with convergence of structures developed during different periods of time. The currently observed structural features in this region were mainly formed between the Late Cretaceous and Miocene (Giacosa *et al*. 2014;

Turienzo *et al*. 2018; Sánchez *et al*. 2018), when the main compressive structures were developed (Fig. 2a, b).

The Cordillera del Viento Fault is one of the main compressional structures formed by the inversion of N-S normal faults that controlled the Late Triassic to Early Jurassic rift sedimentation in the westernmost part of the Neuquén Basin (Vergani *et al*. 1995). During the Andean orogeny, in pre-Eocene times, the inversion of the extensional system occurred, and the Cordillera del Viento Fault became a reverse fault that uplifted Palaeozoic rocks to form the Cordillera del Viento Anticline (Giacosa *et al*. 2014).

The core of the Cordillera del Viento anticline (Giacosa *et al*. 2014) exposes a basement of Middle Palaeozoic metamorphic rocks (Fig. 2a), grouped together in the Guaracó Norte Formation (Zappettini *et al*. 1987; Zanettini *et al*. 2001). These rocks include quartz-rich metasandstones and laminated quartzite layers, with slates towards the top of the sequence which are all cut by numerous quartz and granitic veins (Giacosa *et al*. 2014). The sedimentary protolith is characterised by rhythmic alternation of sandstone and pelite layers showing current ripples (Giacosa *et al*. 2014). The age of the Guaracó Norte Formation is Late Devonian, considering a maximum depositional age, based on the youngest peak of 369 ± 5 Ma (younger than 374 and older than 326 Ma, U-Pb SHRIMP dating of detrital zircon, Zappettini *et al*. 2012).

The Carboniferous sedimentary rocks of the Cordillera del Viento crop out south of the study area, near the Andacollo locality (Fig. 2b), and they are grouped into the Andacollo Group (Digregorio, 1972; Digregorio & Uliana, 1980; Llambías *et al*. 2007). Volcanic and plutonic facies from the Permo-Triassic Choiyoi Group (Stipanicic, 1966; Digregorio, 1972) crop out in the Cordillera del Viento. In the Varvarco area, the Choiyoi Group is composed of two sections, where andesites and rhyolites predominate in the lower and upper sections, respectively (Digregorio, 1972; Zanettini *et al*. 2001).

An extensional deformation period, associated with Gondwana break-up is registered for the Cordillera del Viento. This extensional phase initiated N–S-trending and NNE–SSW in the northern part of the Cordillera del Viento to E–W-trending faults in the southern part, where interbedded shale strata and ignimbrites with wedge geometry are separated by normal faults (Giacosa *et al*. 2014). Magnetic and gravimetric data, combined with field observations, suggest that Late Triassic rifting in the Cordillera del Viento area would have taken place in a regional WNW-ESE to NW trend, with minor local NE structures (Sagripanti *et al*. 2014). Magnetic data revealed that basement rocks are segmented by nearly orthogonal structures (Sagripanti *et al*. 2014).

Between the Late Triassic and Cenozoic, the Neuquén Basin (Fig. 1) developed between 32º and 40º S (e.g., Howell *et al*. 2005). During the Jurassic and Early Cretaceous, the Paleo-Pacific Ocean transgressions produced marine strata which alternated with the deposition of continental sequences in the back-arc setting of this basin, which was affected by thermal subsidence (Legarreta & Uliana, 1991; Vergani *et al*. 1995; Howell *et al*. 2005; Arregui *et al*. 2011).

On the eastern flank of the Cordillera del Viento, the Early to Late Jurassic syn-rift deposits of the early phase of the Neuquén Basin crop out, characterised by variable thickness and normal fault association (Sagripanti *et al*. 2014). The Pre-Cuyo Group (Hettangian-Sinemurian) is represented by the Cordillera del Viento and Milla Michicó formations (Gulisano *et al*. 1984; Riccardi & Stipanicic, 2002). The Jurassic Cuyo and Lotena groups crop out in the northeastern corner of the studied area (Suárez & de la Cruz, 1997; Leanza *et al*. 2005; Llambías *et al*. 2007; Fig. 2).

We discovered that an igneous body, previously assigned to the Radales Aplite, has an Early Jurassic age (185 ± 3 Ma). This aplite is here referred by the informal designation Jurassic Host Granite (Fig. 2a, 3a-b). These felsic intrusives are coeval with the Pre-Cuyo Group. The

provisional name highlights that they are a part of the host rocks for the Late Cretaceous granites studied in this work.

As mentioned in the Introduction chapter, the Andean orogeny was mainly active in the Cordillera del Viento region between Late Cretaceous and Miocene. Andean orogeny reactivated Late Triassic WNW-ESE to NW and NE normal structures (Giacosa *et al*. 2014; Turienzo *et al*. 2018; Sánchez *et al*. 2018). Sánchez *et al*. (2018) reported zircon (U-Th)/He thermochronological data from 72.2 ± 2.8 to 66.0 ± 6.1 Ma and the apatite fission track ages are 51.7 ± 3.2 and 56.5 ± 10.7 Ma for exhumation in the Chos Malal fold-and-thrust belt. The WNW-ESE and NW structures acted as transfer zones, whereas the NE ones as frontal contractional structures (Sagripanti *et al*. 2014). The N-S structures have been interpreted as the result of Andean deformation, as these contractional structures are not related to the rifting architecture and cross-cut the depocentres (Sagripanti *et al*. 2014; Giacosa *et al*. 2014). They concluded that Andean crustal shortening caused the formation of the N-S faults and thrusts, and associated folds, as well as W-E to WNW-ESE strike slip structures. The latter are regarded as lateral structures that control the N and S propagation of the Andean thrusts.

During the Andean compressive stage in the Mid Cretaceous and slightly after, volcanic rocks of the Cayanta Formation (Rapela & Llambías, 1985) were extruded, and subvolcanic magmatic bodies were emplaced into a satellite position with respect to the present magmatic arc in Late Cretaceous-Paleogene times (Llambías & Rapela, 1989; Franchini *et al*. 2003; Cobbold & Rossello, 2003; Hervé *et al*. 2007; Zamora Valcarce 2007; Llambías & Aragón, 2011; Spagnuolo *et al.* 2012; Fig. 1, 2a).

3. Analytical methods

Field studies were carried out in the area of Varvarco, Radales and Butalón plutons, and their host rocks, resulting in 23 thin sections for petrographic studies. The Anisotropy of Magnetic Susceptibility (AMS) study was performed in 17 sites, where nine sites belong to the Varvarco Tonalite, three sites to the Butalón Tonalite, one site to the Radales Aplite, three sites to the Jurassic Host Granites, and one site to the Guaracó Norte Formation. A portable rock drill for paleomagnetic sampling was used. From each site we collected at least five orientated cylinders, summing up to a of 95 specimens (Table 1). The cylinders were orientated using solar and magnetic compasses. Sites are presented in Table 1; their distribution is placed along roads and creeks (Fig. 2a).

The high elevation of the Cordillera del Viento region makes it difficult to map the exact morphology of the Varvarco, Radales and Butalón igneous bodies. ASTER level 1B data were used to complement the mapping of the plutonic bodies (Fig. 3a, b). The studied geological units at 1:200000 scale are presented in Figures 2a and 3a, b. Their recognition in ASTER satellite images was possible through combining two false-color RGB compositions (RGB: 4 3 1 and RGB: 7 4 14), as shown in Figures 3a and b, respectively. False-color RGB composition 7 4 14 is useful to discriminate rocks with different silica content. In map shown in Figure 3b orange/yellow regions correspond to felsic litho-units that are richer in quartz, as shown by the diagnostic SiO-bond spectral absorption at 10.30-11.70 μm (Clark, 1999; bands 13-14 in ASTER).

3.a. Anisotropy of magnetic susceptibility (AMS)

An MFK1-B Kappabridge susceptibilimeter, located at the IGEBA, CONICET, Argentina, was used to perform the anisotropy of the magnetic susceptibility measurements. A minimum of five specimen per site were used (Jelínek, 1978, 1981) to obtain the anisotropy of the

magnetic susceptibility ellipsoids (with principal axes $K_1 > K_2 > K_3$) with the programs ANISOFT 4.2 (Chadima & Jelinek, 2009).

The rock magnetic fabric is defined by the three principal axes of the anisotropy of the magnetic susceptibility ellipsoid ($K_1 > K_2 > K_3$; Bouchez, 2000). A magnetic lineation is defined parallel to K_1. A magnetic foliation is the plane containing K_1 and K_2, with K_3 being the pole to foliation. The magnetic lineation is parallel to the structural lineation (stretching or flow), and the magnetic foliation is parallel to the structural foliation (flattening or flow; Borradaile & Henry, 1997). However, sometimes this relationship may be obliterated by fabric overprinting or by the presence of single domain magnetite (e.g., Rochette *et al*. 1992, 1999; Borradaile & Henry, 1997).

The domain state of magnetite was studied using the diagram of Day *et al*. (1977), which was constructed with the Hc, Ms and Mr (coercive force, saturation magnetisation and remanent magnetisation, respectively) hysteresis parameters, together with the remanent coercive force Hcr (obtained from the backfield curve, Bouchez, 2000). Anhysteretic remanence measurements (Somoza *et al*. 2015) were also performed in some representative samples to check the coaxial behavior of the ferromagnetic and the paramagnetic fabric of the rocks.

The minerals that control the magnetic fabric were investigated by hysteresis curves, isothermal remanent magnetisation-backfield analyses in 6 representative samples (four from Varvarco Tonalite and two from the Jurassic Host Granites). The anisotropy of anhysteretic remanent magnetisation (AARM; e.g., Somoza *et al*. 2015) was applied in three sites. Measurements were performed in the Ludwing-Maximilians University in München, Department of Earth and Environment Sciences, using an equipment called “sushi bar” (Wack & Gilder, 2012).

3.b. Apatite fission track dating (AFT)

Apatite fission tracks (AFT) from samples VAR5 from the Varvarco Tonalite and BU4 from the Butalón Tonalite were analysed in the LA.TE. ANDES laboratory (www.lateandes.com), Salta, Argentina. Both apatite fractions were obtained by mechanical separation, magnetic separation (Frantz isodynamic separator) and heavy liquid treatment (LTS and diiodomethane). Approximately 100 apatite crystals for each sample were then mounted in epoxy. In general, the apatite crystals are subhedral to euhedral, and fractured. The mounted samples were polished, and then leached under nitric acid (HNO_3) 5.5 N for 20 seconds at 20 °C, to reveal spontaneous tracks. The samples were then irradiated with the External Detector in the RA-3 Reactor (Centro Atómico Ezeiza, Buenos Aires, Argentina). The irradiation process took place over 76 hours, with a fluency of $7x10^{15}$ n/cm^2. After the decay period in the reactor, the batch was sent back to the LA.TE. ANDES S.A. laboratory for the fission track measurements. Overall, ~35 grains were used for measurements with a surface greater than 600 μm^2. Areas with obvious crystallographic dislocations were avoided.

All measurements were made with a Zeiss AXIO Imager Z2m binocular microscope. The system is equipped with the TrackWorks Autoscan software, which carried out the counting of the tracks and determination of other parameters, such as fission-track etch pit diameter (Dpar). The ages were determined with the method of ζ value from Hurford & Green (1982, 1983) and Wagner *et al*. (1992). Data processing was done using TrackKey software (Dunkl, 2002) that allowed age calculation. The uncertainty on obtained ages is reported at the 1-2 σ level (Fig. 15a, b).

3.c. Electron microprobe analysis

Electron microprobe analysis of major element concentrations was performed at the

Technical-Scientific Services of Oviedo University (Spain) using a Cameca SX-100 electron microprobe with a voltage of 15 KV, current of 15 nA, and acquisition time of 10 s per element, in WDS mode. Silicates and oxides were used for calibration. The standards of the Bureau de Recherches Geologiques et Minières (BRGM) were used to refine the results. The obtained mineral compositions are presented in Table 2.

4. Results

4.a. ASTER data, field observations and petrography

As stated earlier in text, Varvarco intrusives are made of Varvarco Tonalite, Radales Aplite and Butalón Tonalite. Varvarco Tonalite and Radales Aplite are a part of a composite intrusion of approximately 10 km diameter. Varvarco Tonalite is located in the outer region, Radales Aplite forms a small stock along the Chacay creek (Fig. 3a, b). These units intrude the rocks of the Guaracó Norte Formation and the Jurassic Host Granites. ASTER data suggest that the shape of the Varvarco pluton is broadly circular, with a typical normal zoning pattern, more felsic towards the centre of the intrusion, if we consider that the Radales Aplite is located towards the centre of the Varvarco Tonalite.

The shape of the Butalón Tonalite is more irregular; the body has a length of 8 km and is elongated in E-W direction (Fig. 3a, b). The similar response of pink colors in composition 431 (Fig. 3a) and yellow (Fig. 3b) in composition 7414 of Butalón Tonalite to Varvarco Tonalite, reflects the same composition. The results of the petrographic analysis are shown in the QAP diagram (Fig. 4) and a detailed description of the outcrops visited in the field is presented below.

4.a.1. Guaracó Norte Formation

The Guaracó Norte Formation, representing the host rock of the Varvarco Tonalite and Radales Aplite, was investigated along the Chacay, Matancilla, Manzano and Guaracó Norte creeks (Fig. 2a, 3a-b, 5a). This formation comprises quartzites affected by low-grade metamorphism. Generally, the metamorphic foliation has a NE-SW to N-S strike and steep dip (80º); steep inclinations were also measured close to the contact with the Varvarco Tonalite. In the Guaracó Norte creek, shales and phyllites strike N-S and have low dip (22º) towards the east. The pelitic rocks and sandstones of this formation are affected by hornblende-hornfels metamorphism that led to the development of andalusite, biotite, diopside and hornblende. This has been related to the intrusion of the Late Cretaceous Varvarco Tonalite (Giacosa *et al*. 2014).

4.a.2. Jurassic Host Granites

Along the Manzano and Guaracó Norte creeks we discovered a new unit at site V12 (Fig 2a, 3a-b, and 5b-e), which we tentatively name as the Jurassic Host Granites because it has an age of 185 ± 3 Ma U-Pb age that was obtained by LA-MC-ICP-MS on 12 magmatic zircon crystals (unpubl. data). This unit was previously described by Zanettini *et al*. (2001) as part of the Radales Aplite (formerly considered Radales Granite, see section 4.a.5). The U-Pb geochronology data of the Jurassic Host Granites are part of work in progress.

The Jurassic Host Granites enclose xenoliths derived from the Guaracó Norte Formation (Fig. 5d). Dykes of granitic composition that intrude the Guaracó Norte Formation in the Manzano creek (36º50´42.1"S; 70º40´14.0"W; site V10 in Table 1) can be assigned to the Jurassic Host Granites as well (Fig. 5c). The Jurassic Host Granites have the same syenogranitic composition (Fig. 4) and graphic texture (Fig. 5e) as the Radales Aplite, making it difficult to differentiate them in the field.

4.a.3. Varvarco Tonalite

Along the Matancilla and Chacay creeks, the Varvarco Tonalite can be observed in excellent exposures (Fig. 2a, 5a, 6a-d), which includes the contact relationships with the Guaracó Norte Formation host rock and with the intruding Radales Aplite (Fig. 5a). The Varvarco Tonalite is represented by medium- to fine-grained, equigranular to porphyritic tonalites, in which mafic minerals appear concentrated in blocks (Fig. 6a-b). The Varvarco Tonalite also hosts microgranular enclaves of dioritic composition (Fig. 6b-d). They have a fine-grained, equigranular texture and are composed of amphibole, biotite, plagioclase, quartz, and opaque minerals. The mafic magma was mixed and partially hybridised, as the enclaves show transitional contacts with the host rock (Fig. 6c). Enclave swarms that grade into disintegrated mafic dykes with different hybridisation degrees were also observed (Fig. 6d).

The average modal composition of the Varvarco Tonalite is plagioclase (50%), quartz (30%), orthoclase (4%), amphibole (10%), biotite (5%), and titanomagnetite, titanite, apatite and zircon (1%). Plagioclase crystals are subhedral with complex zoning patterns (Fig. 7a). Incipient sericitic alteration of plagioclase is observed in concentric areas. The observed orthoclase phenocrysts have oikocrystic texture with amphibole and plagioclase inclusions (Fig. 7b). Amphibole is present as subhedral poikilitic megacrysts of nearly 2 cm length that contain plagioclase inclusions. In some areas these large amphibole crystals give the rocks porphyritic appearance. Subhedral biotite is pleochroic from light to dark brown, and mostly fresh (Fig. 7c, d). Quartz is interstitial and contains inclusions of amphibole. Apatite is frequently acicular. All observed textures are magmatic; grain boundaries are straight, especially between plagioclase and orthoclase (Fig. 7b). Locally polygonal contacts between quartz grains are observed, suggesting that static recrystallisation has occurred.

Late aplitic veins of granitic composition (Fig. 6a) intrude the Varvarco Tonalite in the Chacay creek area (orientations: 285º/75º ENE, 320º/65º ENE). Disintegrated porphyritic quartz-dioritic dykes also cross cut the Varvarco Tonalite in the Chacay creek area (Fig. 8a). The dykes have poikilitic amphibole and plagioclase phenocrysts in a granular groundmass that is composed of plagioclase, amphibole, biotite, quartz, and opaque minerals (Fig. 8b). Amphibole has inclusions of plagioclase and rounded quartz (Fig. 8c). Quartz "ocelli" with reaction rims of amphibole and opaque minerals were occasionally observed (Fig. 8d).

4.a.4. Butalón Tonalite

This intrusive body crops out in the Butalón Norte area, approximately 15 km to the south of the Varvarco locality (Fig. 2a, 3a-b). In the RGB compositions of Fig. 3 the Butalón Tonalite is well distinguished from the hosting Permo-Triassic Choiyoi Group. Many granitic dykes and veins of steep to moderate dips and NW to NE strike cross cut the Butalón Tonalite. They have highly variable width between 5 and 50 cm (Fig. 9a). The Butalón Tonalite is classified as fine-grained tonalitic rock with an average composition of plagioclase (63%), quartz (23%), amphibole, biotite (12%), orthoclase (2%), and minor euhedral opaque minerals and acicular apatite (Fig. 4). Mafic microgranular enclaves of dioritic composition are present in this facies as well (Fig. 9b). Amphibole (hornblende determined optically) tends to form poikilitic phenocrysts with plagioclase and biotite inclusions (Fig. 9c). Plagioclase has complex zoning and many plagioclase cores are altered to sericite. Orthoclase is interstitial. Opaque minerals, amphibole and biotite are concentrated in blocks (Fig. 9d).

4.a.5. Radales Aplite

The Radales Aplite crops out only along the Chacay creek (Fig. 2a, 5a, and 8-la). In the satellite image of Fig. 3b, the Radales Aplite is shown in yellow due to its high silica content.

The quartz-rich composition of the Guaracó Norte Formation is shown with a very similar colour, making these two units, which were relatively easy to distinguish in the field (red line in Fig. 5a), not clearly separated in terms of compositions (fig. 3b). Therefore, the boundary was highlighted by dotted line with question marks (Fig. 3a-b).

The contact between the Radales Aplite and the Guaracó Norte Formation is distinctive (Fig. 8e). The Radales Aplite has fine-grained to aplitic texture and a syenogranitic composition (Fig. 4). Plagioclase phenocrysts (12%) are immersed in a granophyric matrix formed of quartz (43%) and orthoclase (40%) (Fig. 8f). The Radales Aplite is considered as late stage of the Varvarco Intrusives because late leucocratic veins intrude the Varvarco Tonalite (Fig. 6a) and the Butalón Tonalite (Fig. 9a), and these veins could correlate with the small stock cropping out along the Chacay creek (Fig. 5a).

4.b. Plagioclase, amphibole and biotite compositions for the Varvarco Tonalite

Electron microprobe analyses of plagioclase, amphibole and biotite from the Varvarco Tonalite are presented in Table 2.

Plagioclase compositions were calculated based on a 32 oxygen formula unit (Table 2a). Plagioclases are labradorite-andesine or andesine (Fig. 10a-c Table 2a). They show oscillatory zoning with decreasing anorthite component (An_{60-30}) from core to rim (Fig. 10a). In some profiles, plagioclase shows slight increase in An_{45-51} from core to more external zones and a labradoritic spike of An_{65} separating an external rim of An_{45-30} (Fig. 10b). These compositional spikes correspond to the inner rings observed in many crystals of Varvarco Tonalite (Fig. 7a). In plagioclases included in amphibole, cores with anorthite content of up to An_{78} were found.

Amphibole structural formulae were calculated based on a 23 oxygen formula unit and with all Ca in the M4 site (Dale *et al*. 2005; Table 2b). Calcic amphibole compositions were obtained, with $Fe_t/(Fe_t+Mg)$ in the 0.30-0.49 range, and low to moderate TiO_2 contents (0.09 to 1.69 wt%, and 0.01 to 0.19 a.p.f.u., respectively). Amphibole cores are mostly magnesiohornblende, whereas amphibole rims are magnesiohornblende to actinolite (Fig. 10c-e). All amphiboles balance the Al tetrahedral site occupancy by both tschermakitic and edenitic substitutions (Fig. 10f).

Compositions of fresh ***biotite*** are shown in Figure 10d). In order to calculate biotite formula, we used the method of Li *et al*. (2020). Most biotites are eastonites boundary to phlogopites with only one biotite (sample 53) falling into siderophyllite field (Fig. 11a). $Fe_t/(Fe_t + Mg)$ ratios vary between 0.44 and 0.58, and aluminium contents vary between 13.21 and 14.55 wt% Al_2O_3 (Table 2c). In the diagram of Foster (1960) and in the trioctahedral Tischendorf *et al*. (1997) diagram, the analysed grains are classified as Mg-biotites (Fig. 11b, c), with biotite from sample 53 falling into the Fe-biotite field (Fig. 11c). In the ternary diagram of Nachit *et al*. (2005), the compositions are compatible with primary and re-equilibrated primary biotites (Fig. 11d). Given that biotite is prone to secondary alteration, Ti was proposed to act as a discriminator, with Ti content <0.55 Ti per 22 oxygen formula unit indicative of fresh magmatic biotite (e.g. Li *et al*. 2017). Varvarco biotites contain 2.6-4.66 wt% TiO_2 which converts to 0.31-0.56 Ti pfu. Only one biotite grain (sample 53) is above 0.55 Ti pfu, supporting their magmatic origin.

4.c. Anisotropy of magnetic susceptibility (AMS)

As was stated in the introduction, AMS studies are used here to evaluate timing and possible emplacement mechanisms of the Varvarco Intrusives in relationship to regional deformation

affecting the Cordillera del Viento range. At all investigated sites, the petrofabric was magmatic, with most minerals of euhedral shapes, and no evidence of late solid-state deformation. The AMS ellipsoids for the individual sites obtained for each lithology are presented in Supplementary Figure S1a-e. As a usual practice in AMS studies, mineral and magnetic fabrics are assumed to be parallel. This could only be accomplished for in the site V8, the only site where we could measure the magmatic foliation in the field, whereas sampling in the other sites was carried out in isotropic rocks.

The corrected anisotropy degree Pj value and the shape parameter T (Jelinek 1981) can be used to describe the geometry of the magnetic ellipsoid. The general positive correlation between Km and Pj shows that titanomagnetite controls the anisotropy in the three analysed plutonic rocks, at both sample and site scale (Supplementary Figure S1a-f). Most values of the shape parameter T at the site scale lie between -0.5 and 0.5 (Supplementary Figure S1f, Table 1). Thus, the magnetic ellipsoids are predominantly triaxial, with good determinations of K1 and K3 axes corresponding, respectively, to magnetic lineations and poles of foliation planes.

The structural mapping of the Varvarco Intrusives was constructed with the AMS data for each sampling site (magnetic foliation and lineation maps; Fig. 12a, b). The orientation of the metamorphic foliation of the Guaracó Norte Formation taken from Giacosa *et al*. (2014) was also added to complete the structural map of the host rock in the Varvarco area (Fig. 12a). In this area, the strike of the magnetic foliation planes of the Varvarco Tonalite oscillate between NNW-SSE and NNE-SSW, and they systematically dip steeply to moderately towards the E (Supplementary Figure S1a; Fig. 12a). In turn, the magnetic foliation of the Radales Aplite and Jurassic Host Granites is steeply dipping as in the Varvarco Tonalite, but the strike of the magnetic foliation of the Jurassic Host Granites is more variable especially in the Manzano creek area (Supplementary Figure S1c, d; Fig. 12a). The Guaracó Norte Formation in the area between the Chacay and Matancilla creeks shows steeply dipping metamorphic foliations in

N-S strike direction, changing to NW-SE strike (Giacosa *et al*. 2014; Fig. 12a). The foliation obtained for V13 site in the Manzano creek has a steeply dipping NNW-SSE strike (Supplementary Figure S1d; Fig. 12a).

The average lineations of the Varvarco Tonalite plunge moderately to steeply towards the SE (Supplementary Figure S1a; Fig. 12b); with one site (V3) with a shallowly plunging lineation trending towards the NW (Supplementary Figure S1a; Fig. 12b). The lineations of the Radales Aplite and Jurassic Host Granites are more diverse: they plunge moderately towards the SE, but lineations plunging to the NE were also found (Supplementary Figure S1c, d; 12b). The lineation found in the Guaracó Norte Formation at V13 site is shallow dipping (Supplementary Figure S1d; 12b).

The quartz-dioritic dyke at V4 site, belonging to the Varvarco Tonalite, has a steeply dipping NW-SE magnetic foliation plane, parallel to dyke strike (Supplementary Figure S1a). Magnetic lineation plunges moderately to the SE (Supplementary Figure S1a).

In the area of Butalón Norte, the Butalón Tonalite has steeply dipping magmatic foliation planes with different attitudes; two sites have an E-W strike (V14 and V16), whereas the remaining site (V15) has N-S strike (Supplementary Figure S1b). The magnetic lineation is subhorizontal in the case of V15 site, and sub-vertical in the case of V14 and V16 sites (Supplementary Figure S1b).

4.d. Mean susceptibility and minerals responsible for the AMS ellipsoids

The simple exploration of the nominal value of bulk magnetic susceptibility indicates which are the main minerals controlling the magnetic fabric of rocks (Bouchez 2000). The mean magnetic susceptibilities (Km) of the Varvarco Tonalite and the Butalón Tonalite are 38.56 $x10^{-3}$ SI and 43.57 $x10^{-3}$ SI, respectively. These values are significantly higher than that for

the Radales Aplite of 2.37 x10^{-3} SI and the Jurassic Host Granites of 20.18 x10^{-3} SI (averages were taken using the data of Table 1). The Guaracó Norte Formation has an even lower Km of 0.44 x10^{-3} SI (Table 1). These high bulk susceptibility values, higher than 4 x10^{-4} SI in most of the samples of the Varvarco and Butalón plutons, suggest that the AMS signal is dominated by magnetite (following the method of Bouchez 2000; Supplementary Figure S2a-b). This is consistent with the mineralogy of the studied granitoids.

Rock magnetic studies can be used to further constrain which minerals dominate the magnetic anisotropy of the rocks. In particular, it is important to determine the domain state of the magnetite, which is essential for the correct interpretation of the magnetic ellipsoids (Grégoire *et al*. 1995; Borradaile & Jackson 2010). Therefore, hysteresis loops, the anisotropy of isothermal remanence (AIRM) and backfield curves were performed in the Varvarco Tonalite (Supplementary Figure S2a) and the Jurassic Host Granites (Supplementary Figure S2b), all in agreement with the presence of magnetite. Magnetite is mostly of pseudo-single domain (PSD) type, as is suggested by the diagram of Day *et al*. (1977) (Fig. 13). However, two samples from the Varvarco Tonalite have a fine-grained, single-domain (SD) magnetite signature (samples from V7 and V8 sites, Fig. 13). Consequently, for these AMS sites, anisotropy of the anhysteretic remanence ellipsoids (AARM) was determined. The coincidence of AARM and AMS ellipsoids (Fig. 14) further supports that magnetite controls the AMS signal and no axis inversion is necessary due to the presence of SD magnetite. It can be concluded that the interpretation of the AMS fabric in all sites is direct, as the magnetic lineation coincides with the K_1 axis and the pole of the magnetic foliation corresponds to the K_3 axis; with the K_1 and K_3 directions taken from the AMS ellipsoids.

4.e. Apatite fission tracks (AFT) results

Samples VAR5 (36º48´58.7"S; 70º40´20.2"W) from the Varvarco Tonalite and BU4 (36º59´03.2"S; 70º41´24.9"W) from the Butalón Tonalite were analysed by AFT. For sample VAR5, AFT results were obtained for 21 apatite crystals. In the radial plot, the mean age obtained is 67.5 ± 8.0 Ma (Late Cretaceous, Fig. 15a; Table 3), with low dispersion of ages from individual crystals. This sample passed the chi-square test suggesting that there is a sole age distribution ($P(\chi^2)$ = 90.72 % > 5%; (Galbraith, 1981; Green, 1981). From sample BU4, 13 apatite crystals were measured. The mean age in the radial plot is 50.3 ± 5.9 Ma (Early Eocene), with low age dispersion for individual grains (Fig. 15b; Table 3). The sample also passed the chi-square test (44.37 %), suggesting that the single grain ages have a sole age distribution ($P(\chi^2)$ = 44.37% > 5%).

5. Discussion

5.a. Magma hybridisation processes in the I-type Varvarco and Butalón intrusive bodies

According to the field and petrographic observations presented above, we interpreted that Varvarco and Butalón tonalites are hybridised igneous bodies which have experienced magma mingling-mixing at their sources. In the area, the more mafic part is represented by the quartz-dioritic dykes, that are intermediate in composition, whereas the more felsic products are represented by the Radales Aplite. The intermediate composition of the quartz-dioritic dykes indicates that the hybridisation process was strong in the area.

The presence of enclaves with different degrees of hybridisation such as enclaves with distinct contacts with the host tonalite (Fig. 5c) or enclaves partially absorbed (corroded) and rimmed by a new hybrid magma (Fig. 5d), and the varied degree of hybridisation observed in enclave swarms (Fig. 5e), suggest that the mingling process would have started before the

emplacement (i.e., at the source). Magmatic flow had possibly favoured the incorporation of heterogeneous enclaves such as those shown in Figure 5c-e (e.g., Bateman, 1995). At higher temperatures, mixing processes are likely to have taken place in the magma chamber. A schematic hybridisation trend is shown in Figure 16, based on Barbarin (2005)'s model.

Increasing crystallisation stages of the intermediate host magma (given mainly by the more voluminous tonalite), would produce the magma hybridisation textures that are observed, which range from early to late mingling features. Scattered mafic magmatic enclaves from the Varvarco and Butalón plutons represent early mingling textures (Fig. 16a, b), whereas the presence of needle-like apatite in these enclaves points to early mafic magma quenching (Wyllie *et al*. 1962). The lack of chilled margins shown by most of the enclaves suggests that local mixing was caused by partial dissolution of the originally chilled borders (Barbarin, 2005). The presence of outer zones of calcic plagioclase (labradoritic spikes) in more sodic plagioclase of the Varvarco Tonalite (Fig. 10b) has also been interpreted as a result of mixing processes involving coeval acid and mafic magmas (Fig. 7b in Hibbard, 1981), and can be due to quenching related to magma hybridisation (Mollo *et al*. 2011; Molina *et al*. 2012).

The enclave swarms present in the Varvarco Tonalite represent magma channels that were used by new pulses of magma arriving to the chamber (e.g., Bateman, 1995; Tobisch *et al*. 1997). The disrupted quartz-dioritic dykes (Fig. 16c) suggest that mafic magma intruded through early fractures in the increasingly more crystallised Varvarco Tonalite (Barbarin, 2005).

The presence of K-feldspar and amphibole oikocrysts with inclusions of early-formed minerals are an evidence of mafic magma undercooling and thermal adjustment (Castro *et al*. 1991). Separate plagioclase crystals constitute chadocrysts included in relatively larger, late amphibole oikocrysts. Chadocrysts remain representatives of an earlier textural development stage (Higgins & Roberge, 2003).

Rounded quartz phenocrysts rimmed by amphibole ("quartz ocelli", Fig. 8d, Vernon, 1990; Hibbard, 1991) are observed in the dioritic to quartz-dioritic dykes and are assigned to the liquid-dominated hybridisation stage (compare Fig. 16a). For quartz ocelli, the parental magma of the quartz-dioritic dykes would have already mixed-mingled by the time when it intruded the solidified host rock, suggesting that the hybridisation process had been achieved in several stages.

No solid-state recrystallisation textures were observed in the Varvarco Intrusives. The only modification of grain boundaries was locally observed is some polygonisation of quartz grains. This suggests that the rocks underwent some degree of static recrystallisation (textural coarsening – Higgins, 2011). The Radales Aplite sample from the V5 site sampled for this study has a granophyric texture suggesting that it cooled under shallow subvolcanic conditions (Vernon, 2010).

The affinity of the Varvarco Intrusives with calc-alkaline I-type magmas (Franchini *et al*. 2003; Casé *et al*. 2008) and the predominance of intermediate compositions in the suite, with hornblende as the main mafic mineral, is typical of Cordilleran magmas. These water-rich compositions are characteristic of subduction environments (Bachmann & Bergantz, 2008). Amphibole and biotite crystals from the Varvarco Tonalite crystallised from magmas of calc-alkaline composition (Fig. 17a-f). According to the classification of Molina *et al*. (2009), the amphibole cores and rims crystallised in equilibrium with subalkaline magmas (Fig. 17a-d), although some amphibole cores fall into the field of subalkaline trachytoid magmas (Fig. 17b). Given that the Varvarco area is poorly studied, there are no granitoid rocks in vicinity to directly compare the mineralogy of Varvarco intrusive. In figures 10, 11, 17 and 18 we compare compositions of amphiboles and biotites with amphiboles and biotites of Zaffarana *et al*. (2014) and of Castro *et al*. (2011). Zaffarana *et al*. reports granitoids of Late Triassic age from the Central Patagonian Batholith at Gastre (North Patagonian Massif) which were

emplaced during the early stages of Gondwana break-up. In turn, Castro *et al*. (2011) reports Jurassic granites of the North Patagonian Batholith in the area of Bariloche (North Patagonian Andes) which were, like the Varvarco rocks, formed by the Andean subduction system. Varvarco amphiboles largely overlap in compositions with the amphiboles reported for the Late Triassic granites of the Gastre Superunit of the Central Patagonian Batholith studied by Zaffarana *et al*. (2014) and have less variable TiO_2 concentrations than amphiboles reported for the Jurassic granites of the Patagonian Batholith studied by Castro *et al*. (2011).

The composition of the biotite crystals is comparable with those from calc-alkaline orogenic suites (Fig. 17e-f) in the tectonic discrimination diagram of Abdel-Rahman (1994). The presence of titanomagnetite as the main oxide in these rocks (Varvarco Tonalite, Fig. S2a) is also compatible with granites being of the magnetite series of Ishihara (1977), in agreement with the results of Casé *et al*. (2008). Similarly, to amphiboles, Varvarco biotites are largely overlapping in Al_2O_3, MgO and FeO_T concentrations with biotites reported by Zaffarana *et al*. (2014) and Castro *et al*. (2011) (Fig. 17e-f), with the biotites by Castro *et al*. (2011) showing slightly larger variations.

5.b. Parental melt conditions of the Varvarco Tonalite

5.b.1. Thermobarometry

To estimate the magma storage temperatures we used geothermometers based on amphibole-plagioclase compositions (Holland & Blundy, 1994, expression B; Molina *et al*. 2021, expressions A1, A2 and B2), amphibole compositions (Ridolfi *et al*. 2010; Ridolfi & Renzulli, 2012; Putirka, 2016), biotite (Henry *et al*. 2005) and melt compositions (Molina *et al*. 2015; Putirka, 2016). Individual results are presented in Table 2, and a summary is presented in Table 4.

Temperatures obtained with the expressions A1, A2, and B2 from Molina *et al*. (2021) agree reasonably and are between 623 and 703 °C (Table 4). In general, temperatures obtained with expression A1 are lower than those obtained with expressions A2 and B2 (Table 4). In the case of the pressure-dependent expressions A1 and A2, results obtained at 1 and at 5 kbar are almost identical (Table 4). For these calculations, we used amphibole compositions 61, 62, 63 and 65, which are from cores of amphibole crystals that satisfy the validation criteria of these geothermometers (Molina *et al*. 2021). These amphibole cores were combined with plagioclases 9, 21, 28 and 39, of andesine composition An_{30-36}, which also pass the validation criteria proposed by the authors (Table 2a and 2b).

The expression B from the Holland & Blundy (1994) amphibole and plagioclase thermometer was used for the same plagioclase cores as in the Molina *et al*. (2021) geothermometer, and amphibole cores with 0.2 Ti (a.p.f.u.) and 1.5 (a.p.f.u.) Al^{IV} contents. This filter yielded a temperature of 784-716 °C for the amphibole cores, and these temperatures agree with the amphibole core-only temperatures (Ridolfi *et al*. 2010; Ridolfi & Renzulli, 2012; Putirka, 2016; Table 2b). However, the higher temperatures could be due to either their high Al^{VI} or to low Mg occupancies, and therefore we consider that the crystallisation temperatures around 623-703 °C obtained with the expressions from Molina *et al*. (2021) are more likely.

Liquid-only temperatures of Molina *et al*. (2015) and Putirka (2016) for amphibole-saturated magmas are, as expected, higher than the temperatures calculated by using amphibole crystals and by the combination of amphibole and plagioclase crystal cores. They range from 922 to 958 ºC (Table 4), and for these calculations the liquid composition was estimated using the whole-rock composition of sample BPN11 from of the Varvarco Tonalite (sample reported in Kay *et al*. 2006). The obtained liquid-only temperatures are compatible with the amphibole stability field in subalkaline liquids (see Fig. 15 in Molina *et al*. 2009 and Fig. 9 in Kiss *et al*. 2014), consistent with a system that involved amphibole-saturated parental melts.

The combination of Ti and Mg/(Mg+Fe) ratios of biotites were used to determine temperature following the method by Henry *et al*. (2005). Biotite compositions are well within the calibration range of the method (X_{Mg} = 0.275-1,000, Ti = 0.04-0.6 a.p.f.u.) and yielded temperatures between 689 and 753ºC, in an excellent agreement with amphibole temperatures determined by Molina *et al*. (2021) (Table 4).

Crystallisation pressures were estimated using the Ridolfi & Renzulli (2012) amphibole-only geobarometers (average between the results of equations 1a and 1b) and the Molina *et al*. (2015) and Anderson & Smith (1995) amphibole-plagioclase barometers. For these calculations, as in the case of geothermometers, only amphiboles 63 and 68 and plagioclases 9, 21, 28 and 29 (Tables 2a and b) that passed all the validation parameters from Molina *et al*. (2015, 2021) were used. We also estimated pressures using the Al in hornblende geobarometers of Hammarstrom & Zen (1986), Hollister *et al*. (1987), Johnson & Rutherford (1989), and Schmidt (1992) (Table 4).

The highest pressures were calculated using Schmidt (1992) calibration, yielding ~4 kbars for amphibole cores (amphibole rim compositions were not suitable for the Al in hornblende calibrations, because of their high silica content, higher than 50% wt; Table 2b). However, Al in hornblende geobarometers tend to overestimate pressures, as both the pressure-dependent tschermakitic and the temperature-dependent edenitic substitutions govern the total Al content in amphiboles (Erdmann *et al*. 2014).

Pressures range from 3.36 to 2.15 kbar when calculated with the geobarometer of Molina *et al*. (2015) and the temperatures obtained with the pressure-independent thermometer B2 from Molina *et al*. (2021).

Similar pressures were obtained using the Molina *et al*. (2015) geobarometer combined with the temperatures obtained with the Ridolfi & Renzulli (2012) and Putirka (2016)

thermometers (Table 4). These pressures broadly agree with the ones obtained with the Anderson & Smith (1995) amphibole barometer (3.13-2.26; Table 4).

5.b.2 Oxygen fugacity.

The oxygen fugacity of the parental melt to the Varvarco Tonalite was calculated using the method by Ridolfi *et al*. (2010) and Wones & Eugster (1965) (Fig. 18a,e). Ridolfi *et al*. (2010) uses amphibole chemistry to derive P-T conditions, H_2O and fO_2. It should be noted that Ridolfi *et al*. (2010) barometer estimates pressures of about 1.1 kbars for amphibole cores and 0.7 kbars for rims, which is significantly lower than pressures derived by other barometers. However, pressure differences within 1-3 kbars have very little effect (~0.2 log unit) on the fO_2 estimates by Ridolfi *et al*. (2010) oxybarometer, which is within the uncertainty of the method (0.4 log unit). According to Ridolfi *et al*. (2010) oxybarometer, amphibole cores and rims from the Varvarco Tonalite have similar fO_2s in the range of -12.2-14.9 logfO_2, which indicates that they crystallised under relatively high fO_2 conditions between the nickel-nickel oxide (NNO) and NNO + 2, typical of calc-alkaline magmas (ΔNNO from -1 to +3; e.g., Gill, 1981; Behrens & Gaillard, 2006).

Wones & Eugster (1965) use (Mg/(Mg+Fe) ratios in biotite and temperatures in order to estimate oxygen fugacity. We used temperatures derived by Henry *et al*. (2005) and biotite cations by Li *et al*. (2020). All biotites plot in the area outlined by a yellow circle (Figure 18d). For comparison, biotites by Castro *et al*. (2011) plot over the wider ranges of fO_2, but still between the NNO and hematite-magnetite (HM) buffers.

fO_2 between NNO and HM buffers are also suggested by Fe^{2+}-Fe^{3+}-Mg ternary for biotite compositions by Wones & Eugster (1965) (Figure 18c). Additionally, high fO_2s of the studied rocks are also in inferred by $Fe_t/(Fe_t+Mg)$ ratios in amphibole (Czamanske & Wones,

1973; Anderson & Smith, 1995), and by titanomagnetite as the main oxide phase of these rocks (see below, Fig. 18b; Supplementary Figure S2a).

5.c. Cooling history and exhumation of the Late Cretaceous and Paleogene plutons

To date, three ages have been obtained for the Varvarco Tonalite: a recalculated K-Ar biotite age of 64.7 ± 3.2 Ma (J.I.C.A./M.M.A.J 2000 in Franchini *et al*. 2003), an $^{40}Ar/^{39}Ar$ biotite age of 69.09 ± 0.13 Ma (Kay *et al*. 2006), and recently a U-Pb SHRIMP zircon age of 67.8 ± 0.8 Ma (Assis, 2019). Zappettini *et al*. (2014) and Zappettini *et al*. (2021) reported an ^{40}Ar-^{39}Ar age of 65.68 ± 0.22 Ma for adularia from veins associated with the hydrothermal alteration of basic volcanic rocks from the Jurassic Colomichicó Formation (Zappettini *et al*. 2018).

If the closure temperatures of the specific minerals for the various geochronological methods are taken into account, it is possible to construct a thermal profile and to calculate the exhumation rate (England and Moldnar 1990). Thus, the thermal profile/cooling curve for the Varvarco Tonalite was constructed (Fig. 19) considering the more accurate geochronological data, namely those obtained by Assis (2019) and by Zappettini *et al*. (2014). The typical closure temperature for U-Pb on zircon is greater than 800 °C (Lee *et al*. 1997). Siégel *et al*. (2018) showed that the zircon saturation temperature in igneous rocks is variable, but normally between 780 and 860 °C for intrusive rocks. Since we do not have Ti in zircon data that would allow to calculate temperatures more precisely, we assume a closure temperature for zircon of ca. 850 °C. Considering that the closure temperature of radiogenic argon in K-feldspar can be as low as 120–150°C (Foland 1974, Harrisson and McDougall 1982), we opted for using a closure temperature of 150 °C for adularia.

A ***one-step*** theoretical curve between 67.8 ± 0.8 Ma (U-Pb in zircon) and 65.68 ± 0.22 Ma (^{40}Ar-^{39}Ar in adularia from hydrothermal veins) was constructed for the exhumation of the Varvarco Tonalite (Fig. 19). This curve gives a continuous cooling rate of approximately 330 °C per Ma. Sánchez *et al*. (2018) proposed tectonically driven continuous exhumation for the Cordillera del Viento during the latest Cretaceous-early Paleogene deformation event. Considering continuous and fast exhumation, the theoretical curve can be extended below 100 °C towards the graphically obtained age of 65.3 Ma (Fig. 19). Fast cooling and exhumation of the Varvarco Tonalite also agrees with the low pressures obtained by geothermobarometry (Tables 2 and 4). The highest pressures calculated for amphibole and plagioclase cores are of the order of 3.37 kbars, that correspond to a source at ~12 km depth. Amphibole rims crystallised at lower pressures of about 1-2 kbars, which is compatible with shallower emplacement at ~4-7 km depth. It means that if the exhumation was a continuous process, as suggested by the thermal profile, the magmatic system could have been exhumed by ~12 km in ca. 2.1 Ma.

Considering that the Paleogene Cayanta Volcanics intruded over the already eroded Varvarco Tonalite and Radales Aplite between 50-56.9 Ma (^{40}Ar-^{39}Ar hornblende ages, Jordan *et al*. 2001) and 67.5 ± 8 Ma (apatite FT age), and Varvarco Tonalite has a final stage of exhumation (below 4-5 km) at least at 59.5 Ma, one important question that we are trying to answer is "When was the final exhumation of the Varvarco Tonalite plus Radales Aplite?" The final tectonic exhumation must have occurred after the crystallisation of the adularia veins in the Radales Aplite at 65.68 ± 0.22 Ma and prior to the extrusion of the Cayanta volcanic rocks at 50-56.9 Ma. The Varvarco Tonalite magmatic fabric was not affected by any solid-state deformation that could have been superimposed onto these rocks, and shallow emplacement conditions helped in the fast exhumation process. The Radales Aplite has granophyric texture, which suggests that it would have experienced a greater degree of

undercooling than the Varvarco Tonalite (Vernon, 2010) - consistent with emplacement at a shallower crustal level. At this point, we do not have any crystallisation age for the Radales Aplite that may corroborate the relationship between cooling and exhumation. The final exhumation possibly occurred coevally with the generation of the adularia veins in the Radales Aplite at 65.68 Ma or later as part of the continuous process of exhumation at 65.3 Ma (Fig. 19), or between 65.3 and 59.5 Ma, considering the apatite FT age. We do not exclude that the final exhumation could have happened after 59.5 Ma, but certainly before 56.9 Ma.

Note that the K-Ar biotite cooling age of 64.7 ± 3.2 Ma (Franchini *et al*. 2003) falls onto this cooling curve given the uncertainty of the fission track ages. The biotite age of 69.09 ± 0.13 Ma - also from the Varvarco Tonalite (Kay *et al*. 2006) - is much older than the U-Pb zircon age of Assis (2019). These two ages are not within the uncertainty. It is difficult to explain this age difference in the context of the thermal profile, but it could be related with an early (c. 69 Ma) input of mafic hydrated magma into the magmatic system of the Varvarco Tonalite.

Given the age of 50.3 ± 5.9 Ma (AFT, sample BU4), the Butalón Tonalite was exhumed a little later than the Varvarco Tonalite, in Paleogene. However, the exact age of its exhumation is not yet fully constrained. The AFT age of Butalón Tonalite is not as well defined as that for the Varvarco Tonalite, because less fission track data could be obtained from the dated sample BU4 (Table 3). It seems that the Butalón Tonalite was emplaced in an already exhumed orogenic system. This is also in agreement with the different cooling rates of the Varvarco Tonalite and the Radales Aplite, as inferred from their magmatic textures discussed before.

Temperature and pressure estimates derived from mineral chemistry are here integrated with the Tt (temperature-time) path reconstruction in order to derive a geothermal gradient for the Cordillera del Viento area. In the first place, amphibole core compositions provide

temperatures around ~620-700°C and pressures around 3.36-2 kbars, which correspond to nearly ~12 km depth (Fig. 19). At these P-T (pressure-temperature) conditions the Varvarco Tonalite was almost completely crystallised and already cooling. Then, amphibole rim compositions record pressures of 2-1 kbars which correspond to ~4-7 km depth (Fig. 19), and, at this stage, the temperatures were no higher than 120°C, as apatite fission tracks anneal at temperatures higher than this threshold (Ehlers and Farley, 2003; Reiners and Ehlers, 2005). From these two T and P regimes, a geothermal gradient of ~62.5°C/km can be obtained, revealing the cooling and exhumation history of the Varvarco Tonalite. Such high geothermal gradient suggests that the intrusive rocks were cooling down and exhumed at the same time. The lower geothermal gradients of ~51°C/km (Sigismondi 2013; Sigismondi and Ramos 2009a, 2009b, see Galetto *et al*. 2021) can be reflecting the pre-Andean tectonic scenario in the modern easternmost region of the Neuquén Basin which was not affected by Andean deformation (Galetto *et al*. 2021).

5.d. Magnetic fabrics of magmatic origin in the Late Cretaceous and Paleogene plutons

As previously shown in section 4.d, the magnetic fabrics determined by the ASM method in the Varvarco Tonalite, Butalón Tonalite and the Radales Aplite can be interpreted as of pure magmatic origin representative of magma flow during the Late Cretaceous-Paleogene. In particular, the fast-cooling rate estimated from the U-Pb, ^{40}Ar-^{39}Ar, and AFT ages suggest that the magmatic fabrics of the Varvarco Tonalite were acquired during pluton cooling and exhumation.

The magmatic fabrics from the Varvarco Tonalite and Radales Aplite are steeply dipping, with a predominant N-S strike (Supplementary Figure S1a), which is mostly consistent with the orientation of the regional structures from the Andean orogenic cycles (Giacosa *et al*.

2014; Turienzo *et al*. 2018; Sánchez *et al*. 2018). The oscillating character of the magmatic fabrics strongly suggests that they could have been influenced by intrinsic dynamics inside the magma chamber. However, there is some evidence of regional stress influence, such as N-S elongation of the pluton along the Matancillas creek (Fig. 2a, 3a-b) and NNE-SSW to NNW-SSE fabrics. Even though coupling with the wall rock may not occur, the Andean stress field might have influenced magma flow to some extent. The N-S Matancillas creek goes along the trace of the N-S directed Cordillera del Viento Fault (Fig. 2a, b). This fault was active during the Andean deformation and could have favoured magma ascent through the crust. The lack of tectonic deformation suggests that pluton emplacement took place either during or soon after the Late Cretaceous deformation event in the Neuquén Andes. Alternatively, similar fabrics may be possible even during a regional deformation event if strain partitioning in low- vs high-strain domains is present. However, post-tectonic emplacement is also in agreement with observations made in the other parts of the Naunauco Belt, where other subvolcanic bodies were post-tectonically emplaced (Llambías & Malvicini, 1978; Zamora Valcarce *et al*. 2011).

Other plutons which were emplaced late with respect to main tectonic deformation events have been described as having flat roofs and steeply dipping foliation planes along the pluton walls (de Saint-Blanquat *et al*. 2006; Payacán *et al*. 2014). Their internal fabric is strongly decoupled from the host rock fabrics, likely reflecting magma chamber processes (Paterson *et al*. 1998).

Unfortunately, the areas of the Varvarco Tonalite (marked as "VT" in Fig. 2 and in Fig. 3a-b) where we expected to see flattened magmatic foliations in the roof of the intrusion, were only inferred by satellite images and inaccessible for sampling. Some sites, such as site V3, within the Varvarco Tonalite show flat foliation planes, suggesting a location near the pluton roof. But in general, steeply dipping magmatic foliations are dominant and probably reflect

closeness to the contact with the host rocks. The contact area is the place where the highest degree of coupling between the magmatic and the host rock fabrics usually occurs (Paterson *et al*. 1998). In this sense, the parallel foliations presented by the metamorphic rocks of the Guaracó Norte Formation and the magmatic rocks of the Varvarco and Radales plutons in the area between the Matancilla and Chacay creeks suggest that some degree of mechanical coupling existed between them (Fig. 12a). However, the contact aureole in the margin-parallel fabrics rules out regional deformation as a significant cause of fabric formation, and instead suggests late fabric formation due to internal processes during emplacement (Paterson *et al*. 1998). In addition, the thermal contrast between the Guaracó Norte Formation and the Varvarco Tonalite is consistent with the results obtained from geothermobarometry, which suggests that the Varvarco pluton was emplaced at a high crustal level at ~2-3 kbars (between 7-11 km depth).

Lastly, magma feeder zones, where magma upwelled, can be traced by the existence of vertical magmatic lineations at sites for which AMS ellipsoids of prolate shape (T<0) were measured, such as V1, V2, V6 and V7 from the Varvarco Tonalite (Supplementary Figure S1e).

6. Conclusions

Field observations and petrographic analysis indicates that magma hybridisation was the main process in the Varvarco and Butalón plutons. The magnetic fabrics of these plutons are dominated by titanomagnetite. This, together with mineral chemistry data (amphibole and biotite) confirms that these magmatic phases belong to the I-type series of calc-alkaline igneous bodies.

The fabrics are, without exception, magmatic, and the AMS data can be interpreted as the result of emplacement and rapid exhumation of fast-cooled plutons. The AFT ages of the Varvarco Tonalite are close to its crystallisation age, as well as the fast-cooling age calculated for this pluton (330°C/My; Fig. 19). Shallow emplacement conditions were estimated based on geothermobarometry (2-3 kbars, equivalent to 12 km depth). These combined data allow us to infer uplift in the region between 64.9 and 66 Ma. Geothermobarometry and AFT data suggest the geothermal gradient of the area of ~62.5 °C/km. The magmatic system in the Varvarco area could have been exhumed by ~12 km in ca. 2.1 Ma.

The orientation of the magmatic fabrics implies that they formed mostly due to magma chamber processes. However, they could have been controlled, in part, by the regional Late Cretaceous compressive deformation. As the plutons are located along the trace of the Cordillera del Viento Fault, and the fact that they are devoid of post emplacement tectonic deformation, reactivations of this fault are not supported.

Acknowledgements

We want to thank Dr. Sebastián Oriolo and an anonymous reviewer for their valuable suggestions that greatly improved the manuscript. We cordially thank Fuat Yavuz for help with biotite diagrams in the earlier version of this article. The research projects from the Universidad Nacional de Río Negro (UNRN) PI-40-A-466, PI-40-A-547, PI-40-A-631, PI-40-A-798 and PI-40-A-916; project PIP CONICET 2015-2017 11220150100736CO; PICT 2019-01809; project CGL 2012-38396-C01 of the Spanish Program for Science Technology (I+D+i) and FEDER Funds of the EU, contributed to finance this work. The research of José F. Molina has been supported for the Ministerio de Economía y Competitividad (Gobierno de España), grant numbers:

CGL2013-40785-P and CGL2017-84469-P, and Consejería de Economía y Conocimiento (Junta de Andalucía), grant number: RNM2163. The research of Natalia Hauser has been supported in part by CNPq fellowships (grants 309878/2019-5). This study was financed in part by the Coordenação de Aperfeiçoamento de Pessoal de Nivel Superior – Brasil (CAPES) – Finance Code 001.

Competing Interest

The authors declare that they have no known competing financial interests or personal relationships that could have appeared to influence the work reported in this paper.

Supplementary Material

Supplementary Figure S.1: (a-e) ASM data for the 17 studied sites, showing the individual magnetic ellipsoids for each site, and the P vs. Km and T vs. P diagrams, as obtained with the software Anisoft 4.2. (f) AMS scalar data at the site scale, showing the Pj vs. Km and T vs. Pj graphs (Jelinek, 1981). Equal area projection in geographic coordinate system.

Supplementary Figure S.2: Hysteresis loops and backfield curves obtained for samples from the Varvarco Tonalite and Jurassic Host Granites.

Supplementary Table S.1: Summary of the compiled ages of intrusive and volcanic rocks shown in Figure 1.

Supplementary material is online at http://journals.cambridge.org/geo'

References

Abdel-Rahman Abdel-Fattah, M. 1994. Nature of Biotites from Alkaline, Calc-alkaline, and Peraluminous Magmas. *Journal of Petrology* 35, 525–541. https://doi.org/10.1093/petrology/35.2.525

Allmendinger, R. W., Cardozo, N. & Fisher, D. M. 2012. *Structural Geology Algorithms: Vectors and Tensors*. Cambridge University Press, Cambridge, 289 pp. https://doi.org/10.1017/CBO9780511920202

Anderson, J. L. & Smith, D. R. 1995. The effects of temperature and fO2 on the Al-in-hornblende barometer. *American Mineralogist* 80, 549–559. https://doi.org/10.2138/am-1995-5-614

Archanjo, C. J., Launeau, P. & Bouchez, J. L. 1995. Magnetic fabric vs. magnetite and biotite shape fabrics of the magnetite-bearing granite pluton of Gameleiras (Northeast Brazil). *Physics of the Earth and Planetary Interiors* 89, 63-75. https://doi.org/10.1016/0031-9201(94)02997-P

Archanjo, C. J., Trindade, R. I. F., Bouchez, J. L. & Ernesto, M. 2002. Granite fabrics and regional-scale strain partitioning in the Seridó belt (Borborema Province, NE Brazil). *Tectonics* 21, 3-1-3–14. https://doi.org/10.1029/2000TC001269

Arregui, C., Carbone, O. & Leanza, H. A. 2011. Contexto tectosedimentario, in: *Relatorio Del 18° Congreso Geológico Argentino, Neuquén*. Neuquén, pp. 29-36.

Assis, O. S. 2019. Petrografía y fábrica magnética de la Granodiorita Varvarco y plutones asociados, Cretácico Tardío-Paleoceno de los Andes Neuquinos. Universidad Nacional de Río Negro. http://rid.unrn.edu.ar/jspui/handle/20.500.12049/2256

Bachmann, O. & Bergantz, G. W. 2008. Deciphering Magma Chamber Dynamics from Styles of

Compositional Zoning in Large Silicic Ash Flow Sheets. *Reviews in Mineralogy and Geochemistry* 69, 651–674. https://doi.org/10.2138/rmg.2008.69.17

Barbarin, B. 2005. Mafic magmatic enclaves and mafic rocks associated with some granitoids of the central Sierra Nevada batholith, California: nature, origin, and relations with the hosts. *Lithos* 80, 155–177. https://doi.org/10.1016/j.lithos.2004.05.010

Bateman, P. C. & Eaton, J. P. 1967. Sierra Nevada Batholith. *Science* 158, 1407-1417.

Bateman, R. 1995. The interplay between crystallization, replenishment and hybridization in large felsic magma chambers. *Earth-Science Reviews* 39, 91-106. https://doi.org/10.1016/0012-8252(95)00003-S

Baxter, S. & Feely, M. 2002. Magma mixing and mingling textures in granitoids: Examples from the Galway Granite, Connemara, Ireland. *Mineralogy and Petrology* 76, 63-74. https://doi.org/10.1007/s007100200032

Behrens, H. & Gaillard, F. 2006. Geochemical Aspects of Melts: Volatiles and Redox Behavior. *Elements* 2, 275-280. https://doi.org/10.2113/gselements.2.5.275

Borradaile, G. J. & Henry, B. 1997. Tectonic applications of magnetic susceptibility and its anisotropy. *Earth-Science Reviews* 42, 49-93. https://doi.org/10.1016/S0012-8252(96)00044-X

Borradaile, G. J. & Jackson, M. 2010. Structural geology, petrofabrics and magnetic fabrics (AMS, AARM, AIRM). *Journal of Structural Geology* 32(10), 1519-1551. https://doi.org/10.1016/j.jsg.2009.09.006

Bouchez, J.-L., 2000. Anisotropie de susceptibilité magnétique et fabrique des granites. *Comptes Rendus de l'Académie des Sciences - Series IIA - Earth and Planetary Science* 330, 1–14. https://doi.org/10.1016/S1251-8050(00)00120-8

Cardozo, N. & Allmendinger, R. W. 2013. Spherical projections with OSXStereonet. *Computers & Geosciences* 51, 193-205. https://doi.org/10.1016/j.cageo.2012.07.021

Casé, A. M., López-Escobar, L., Danieli, J. C. & Schalamuk, A. 2008. Butalón igneous rocks, Neuquén, Argentina: Age, stratigraphic relationships and geochemical features. *Journal of South American Earth Sciences* 26, 188-203. https://doi.org/10.1016/j.jsames.2007.11.001

Castro, A., Moreno-Ventas, I., Fernández, C., Vujovich, G., Gallastegui, G., Heredia, N., Martino, R. D. D., Becchio, R., Corretgé, L. G. G., Díaz-Alvarado, J., Such, P., García-Arias, M., & Liu, D.-Y. 2011. Petrology and SHRIMP U–Pb zircon geochronology of Cordilleran granitoids of the Bariloche area, Argentina. *Journal of South American Earth Sciences* 32(4), 508-530. https://doi.org/10.1016/j.jsames.2011.03.011

Castro, A., Moreno-Ventas, I. & de la Rosa, J. D. 1991. Multistage crystallization of tonalitic enclaves in granitoid rocks (Hercynian belt, Spain): implications for magma mixing. *Geologische Rundschau* 80, 109-120. https://doi.org/10.1007/BF01828770

Chadima, M. & Jelinek, V. 2009. Anisoft 4.2: Anisotropy data browser for windows.

Clark, R. N. 1999. Spectroscopy of Rocks and Minerals and Principles of Spectroscopy. Manual of Remote Sensing. *Remote Sensing for the Earth Sciences: Manual of Remote Sensing*.

Cobbold, P. R. & Rossello, E. A. 2003. Aptian to recent compressional deformation, foothills of the Neuquén Basin, Argentina. *Marine and Petroleum Geology* 20, 429–443. https://doi.org/10.1016/S0264-8172(03)00077-1

Czamanske, G. K. & Wones, D. R. 1973. Oxidation During Magmatic Differentiation, Finnmarka Complex, Oslo Area, Norway: Part 2, The Mafic Silicates. *Journal of Petrology* 14, 349-380. https://doi.org/10.1093/petrology/14.3.349

D'Eramo, F., Pinotti, L., Tubía, J. M., Vegas, N., Aranguren, A., Tejero, R. & Gómez, D. 2006. Coalescence of lateral spreading magma ascending through dykes: a mechanism to form a granite canopy (El Hongo pluton, Sierras Pampeanas, Argentina). *Journal of the Geological Society* 163, 881–892. https://doi.org/10.1144/0016-764905-060

Dale, J., Powell, R., White, R. W., Elmer, F. L. & Holland, T. J. B. 2005. A thermodynamic model for Ca-Na clinoamphiboles in Na_2O-CaO-FeO-MgO-Al_2O_3-SiO_2-H_2O-O for petrological calculations. *Journal of Metamorphic Geology* 23, 771-791. https://doi.org/10.1111/j.1525-1314.2005.00609.x

Day, R., Fuller, M. & Schmidt, V. A. 1977. Hysteresis properties of titanomagnetites: grain-size and compositional dependence. *Physics of the Earth and Planetary Interiors* 13, 260-267.

de Saint-Blanquat, M., Habert, G., Horsman, E., Morgan, S. S., Tikoff, B., Launeau, P. & Gleizes, G. 2006. Mechanisms and duration of non-tectonically assisted magma emplacement in the upper crust: The Black Mesa pluton, Henry Mountains, Utah. *Tectonophysics* 428, 1–31. https://doi.org/10.1016/j.tecto.2006.07.014

de Saint Blanquat, M. & Tikoff, B. 1997. Development of Magmatic to Solid-State Fabrics during Syntectonic Emplacement of the Mono Creek Granite, Sierra Nevada Batholith, in: *Granite: From Segregation of Melt to Emplacement Fabrics* (ed J. L., Bouchez), pp. 231-252. Springer, Dordrecht. https://doi.org/10.1007/978-94-017-1717-5_15

Deer, W. A., Howie, R. A. & Zussman, J. 2013. *An Introduction to the Rock-Forming Minerals*. Mineralogical Society of Great Britain and Ireland, London.

Digregorio, J. H. 1972. Neuquén. In *Geología Regional Argentina* (ed A. F. Leanza), pp. 439-505. Academia Nacional de Ciencias, Córdoba.

Digregorio, J. H. & Uliana, M. A. 1980. Cuenca Neuquina. In *Geología Regional Argentina* (ed J. C. M., Turner), pp. 985-1032. Academia Nacional de Ciencias, Córdoba.

Dunkl, I. 2002. Trackkey: a Windows program for calculation and graphical presentation of fission track data. *Computers & Geosciences* 28, 3-12. https://doi.org/10.1016/S0098-3004(01)00024-3

Ehlers, T. A., Farley, K. A., 2003. Apatite (U–Th)/He thermochronometry: methods and

applications to problems in tectonics and surface processes. *Earth and Planetary Science Letters* 206, 1-14.

England P. & Molnar, P. 1990. Surface uplift, uplift of rocks, and exhumation of rocks. *Geology* 18, 1173-1177. https://doi.org/10.1130/0091-7613(1990)018<1173:SUUORA>2.3.CO;2

Erdmann, S., Martel, C., Pichavant, M. & Kushnir, A. 2014. Amphibole as an archivist of magmatic crystallization conditions: problems, potential, and implications for inferring magma storage prior to the paroxysmal 2010 eruption of Mount Merapi, Indonesia. *Contributions to Mineralogy and Petrology* 167, 1016. https://doi.org/10.1007/s00410-014-1016-4

Ferré, E. C. & Améglio, L. 2000. Preserved magnetic fabrics vs. annealed microstructures in the syntectonic recrystallised George granite, South Africa. *Journal of Structural Geology* 22, 1199-1219. https://doi.org/10.1016/S0191-8141(00)00026-2

Foland K A, 1974. Ar^{40} diffusion in homogeneous orthoclase and an interpretation of Ar diffusion in K-feldspars. *Geochimica et cosmochimica Acta* 38, 151-166.

Foster, M. D. 1960. Interpretation of the Composition of Trioctahedral Micas. *USGS Professional Paper* 354, 11-48.

Franchini, M., López-Escobar, L., Schalamuk, I. B. A. & Meinert, L. 2003. Magmatic characteristics of the Paleocene Cerro Nevazón region and other Late Cretaceous to Early Tertiary calc-alkaline subvolcanic to plutonic units in the Neuquén Andes, Argentina. *Journal of South American Earth Sciences* 16, 399-421. https://doi.org/10.1016/S0895-9811(03)00103-2

Galbraith, R. F. 1981. On statistical models for fission track counts. *Journal of the International Association for Mathematical Geology* 13, 471-478. https://doi.org/10.1007/BF01034498

Galetto, A., Georgieva, V., García, V. H., Zattin, M., Sobel, E. R., Glodny, J., Bordese, S., Arzadún, G., Bechis, F., Caselli, A. T. & Becchio, R. 2021. Cretaceous and Eocene rapid

cooling phases in the Southern Andes (36°-37°S): insights from low-temperature thermochronology, U-Pb geochronology and inverse thermal modeling from Domuyo area, Argentina. *Tectonics* 40, 1-30. https://doi.org/10.1029/2020TC006415

Giacosa, R., Allard, J., Foix, N. & Heredia, N. 2014. Stratigraphy, structure and geodynamic evolution of the Paleozoic rocks in the Cordillera del Viento (37º S latitude, Andes of Neuquén, Argentina). *Journal of Iberian Geology* 40, 331-348. https://doi.org/10.5209/rev_JIGE.2014.v40.n2.45301

Gill, J. B. 1981. *Orogenic Andesites and Plate Tectonics, Minerals and Rocks*. Springer Berlin Heidelberg, Berlin. https://doi.org/10.1007/978-3-642-68012-0

Green, P. F. 1981. A new look at statistics in fission-track dating. *Nuclear Tracks* 5, 77-86. https://doi.org/10.1016/0191-278X(81)90029-9

Grégoire, V., de Saint Blanquat, M., Nédélec, A. & Bouchez, J.-L. 1995. Shape anisotropy versus magnetic interactions of magnetite grains: Experiments and application to AMS in granitic rocks. *Geophysical Research Letters* 22(20), 2765-2768. https://doi.org/10.1029/95GL02797

Gulisano, C. A., Gutiérrez Pleimling, A. R. & Digregorio, R. E. 1984. Esquema estratigráfico de la secuencia jurásica del oeste de la provincia del Neuquén. In *9º Congreso Geológico Argentino*, pp. 236-259.

Hammarstrom, J. M. & Zen, E. 1986. Aluminum in hornblende: an empirical igneous geobarometer. *American Mineralogist* 71, 1297–1313.

Harrison T M, McDougall I, 1982. The thermal significance of potassium feldspar K-Ar ages inferred from $^{40}Ar/^{39}Ar$ age spectrum results. *Geochimica et cosmochimica Acta* 46, 1811-1820.

Henry, D. J., Guidotti, C. V. & Thomson, J. A. 2005. The Ti-saturation surface for low-to-medium pressure metapelitic biotites: Implications for geothermometry and Ti-

substitution mechanisms. *American Mineralogist* 90(2-3), 316-28.

Hervé, F., Pankhurst, R. J., Fanning, C. M., Calderón, M. & Yaxley, G. M. 2007. The South Patagonian batholith: 150 my of granite magmatism on a plate margin. *Lithos* 97, 373-394. https://doi.org/10.1016/j.lithos.2007.01.007

Hibbard, M. J. 1981. The magma mixing origin of mantled feldspars. *Contributions to Mineralogy and Petrology* 76, 158–170. https://doi.org/10.1007/BF00371956

Hibbard, M. J. 1991. Textural anatomy of twelve magma-mixed granitoid systems. In *Enclaves and Granite Petrology*, pp. 431-444.

Higgins, M. D. 2011. Textural coarsening in igneous rocks. *International Geology Review* 53(3-4), 354-376. https://doi.org/10.1080/00206814.2010.496177

Higgins, M. D. & Roberge, J. 2003. Crystal Size Distribution of Plagioclase and Amphibole from Soufriere Hills Volcano, Montserrat: Evidence for Dynamic Crystallization-Textural Coarsening Cycles. *Journal of Petrology* 44, 1401-1411. https://doi.org/10.1093/petrology/44.8.1401

Holland, T. & Blundy, J. 1994. Non-ideal interactions in calcic amphiboles and their bearing on amphibole-plagioclase thermometry. *Contributions to Mineralogy and Petrology* 116, 433-447. https://doi.org/10.1007/BF00310910

Hollister, L. S., Grissom, G. C., Peters, E. K., Stowell, H. H. & Sisson, V. B. 1987. Confirmation of the empirical correlation of Al in hornblende with pressure of solidification of calc-alkaline plutons. *American Mineralogist* 72, 231-239.

Howell, J. A., Schwarz, E., Spalletti, L. A., Veiga, G. D. 2005. The Neuquén Basin: an overview. In *The Neuquén Basin, Argentina: A Case Study in Sequence Stratigraphy and Basin Dynamics* (eds G. D. Veiga, L. A. Spalletti, J. A. Howell & E. Schwarz), pp. 1-14. Geological Society, Special Publication, 252, London.

Hrouda, F. 1982. Magnetic anisotropy of rocks and its application in geology and geophysics.

Geophysical Surveys 5, 37-82. https://doi.org/10.1007/BF01450244

Hurford, A. J. & Green, P. F. 1983. The zeta age calibration of fission-track dating. *Chemical Geology* 41, 285-317. https://doi.org/10.1016/S0009-2541(83)80026-6

Hurford, A. J. & Green, P. F. 1982. A users' guide to fission track dating calibration. *Earth and Planetary Science Letters* 59, 343-354. https://doi.org/10.1016/0012-821X(82)90136-4

Ishihara, S. 1977. The Magnetite-series and Ilmenite-series Granitic Rocks. *Mining Geology* 27, 293-305.

Jelinek, V. 1981. Characterization of the magnetic fabric of rocks. *Tectonophysics* 79, T63-T67. https://doi.org/10.1016/0040-1951(81)90110-4

Jelínek, V. 1978. Statistical processing of anisotropy of magnetic susceptibility measured on groups of specimens. *Studia Geophysica et Geodaetica* 22, 50-62. https://doi.org/10.1007/BF01613632

Johnson, M. C. & Rutherford, M. J. 1989. Experimental calibration of the aluminum-in-hornblende geobarometer with application to Long Valley caldera (California) volcanic rocks. *Geology* 17, 837-841. https://doi.org/10.1130/0091-7613(1989)017<0837:ECOTAI>2.3.CO;2

Jordan, T. E., Burns, W. M., Veiga, R., Pángaro, F., Copeland, P., Kelley, S. & Mpodozis, C. 2001. Extension and basin formation in the southern Andes caused by increased convergence rate: A mid-Cenozoic trigger for the Andes. *Tectonics* 20, 308-324. https://doi.org/10.1029/1999TC001181

Kawakatsu, K. & Yamaguchi, Y. 1987. Successive zoning of amphiboles during progressive oxidation in the Daito-Yokota granitic complex, San-in belt, southwest Japan. *Geochimica et Cosmochimica Acta* 51, 535-540. https://doi.org/10.1016/0016-7037(87)90067-6

Kay, S. M., Burns, W. M., Copeland, P. & Mancilla, O. 2006. Upper Cretaceous to Holocene

magmatism and evidence for transient Miocene shallowing of the Andean subduction zone under the northern Neuquén Basin In *Evolution of an Andean Margin: A Tectonic and Magmatic View from the Andes to the Neuquén Basin (35°-39°S Lat)*, pp. 16-90. Geological Society of America. https://doi.org/10.1130/2006.2407(02)

Kiss, B., Harangi, S., Ntaflos, T., Mason, P. R. D. & Pál-Molnár, E. 2014. Amphibole perspective to unravel pre-eruptive processes and conditions in volcanic plumbing systems beneath intermediate arc volcanoes: a case study from Ciomadul volcano (SE Carpathians). *Contributions to Mineralogy and Petrology* 167, 986. https://doi.org/10.1007/s00410-014-0986-6

Leake, B. E., Woolley, A. R., Arps, C. E. S., Birch, W. D., Gilbert, M. C., Grice, J. D., Hawthorne, F. C., Kato, A., Kisch, H. J., Krivovichev, V. G., Linthout, K., Laird, J., Mandarino, J., Maresch, W. V., Nickel, E. H., Rock, N. M. S., Schumacher, J. C., Smith, D. C., Stephenson, N. C. N., Ungaretti, L., Whittaker, E. J. W. & Youzhi, G. 1997. Nomenclature of Amphiboles; Report of the Subcommittee on Amphiboles of the International Mineralogical Association Commission on New Minerals and Mineral Names. *Mineralogical Magazine* 61, 295-321. https://doi.org/10.1180/minmag.1997.061.405.13

Leanza, H. A., Llambías, E. J. & Carbone, O. 2005. Unidades estratigráficas limitadas por discordancias en los depocentros de la Cordillera del Viento y la Sierra de Chacaico durante los inicios de la Cuenca Neuquina. In *6º Congreso de Exploración de Hidrocarburos*, p. 13.

Lee, J. K. W., Williams, I. S. & Ellis, D. J. 1997. Pb, U and Th diffusion in natural zircon. *Nature* 390, 159-162. https://doi.org/10.1038/36554

Legarreta, L. & Uliana, M. A. 1991. Jurassic-Cretaceous marine oscillations and geometry of back-arc basin fill, central Argentine Andes. In *Sedimentation, Tectonics and Eustasy*,

pp. 429-450. Blackwell Publishing Ltd., Oxford, UK. https://doi.org/10.1002/9781444303896.ch23

Li, X., Chi, G., Zhou, Y., Deng, T. & Zhang, J. 2017. Oxygen fugacity of Yanshanian granites in South China and implications for metallogeny. *Ore Geology Reviews* 88, 690-701.

Li, X., Zhang, C., Behrens, H. & Holtz, F. 2020. Calculating biotite formula from electron microprobe analysis data using a machine learning method based on principal components regression. *Lithos* 356-357, 105371.

Llambías, E. J. & Aragón, E. 2011. Volcanismo Paleógeno. In *Relatorio Del 18° Congreso Geológico Argentino, Neuquén*, pp. 265-274.

Llambías, E. J., Leanza, H. A. & Carbone, O. 2007. Evolución tectono-magmática durante el Pérmico al Jurásico temprano en la Cordillera del Viento (37°05′S - 37°15′S): Nuevas evidencias geológicas y geoquímicas del inicio de la Cuenca Neuquina. *Revista de la Asociación Geologica Argentina* 62, 217-235.

Llambías, E. J. & Malvicini, L. 1978. Geología, Petrología y Metalogénesis del área de Colipilli, provincia del Neuquén, República Argentina. *Revista de la Asociación Geológica Argentina* 33, 257-276.

Llambías, E. J. & Rapela, C. W. 1989. Las volcanitas de Collipilli, Neuquén (37ºS) y su relación con otras unidades paleógenas de la cordillera. *Revista de la Asociación Geológica Argentina* 44, 224-236.

McNulty, B. A., Tobisch, O. T., Cruden, A. R. & Gilder, S. 2000. Multistage emplacement of the Mount Givens pluton, central Sierra Nevada batholith, California. *Geological Society of America Bulletin* 112, 119-135. https://doi.org/10.1130/0016-7606(2000)112<119:MEOTMG>2.0.CO;2

Molina, J. F., Cambeses, A., Moreno, J. A., Morales, I., Montero, P. & Bea, F. 2021. A reassessment of the amphibole-plagioclase NaSi–CaAl exchange thermometer with

applications to igneous and high-grade metamorphic rocks. *American Mineralogist* 106, 782-800.

Molina, J. F., Montero, P., Bea, F., Scarrow & J. H. 2012. Anomalous xenocryst dispersion during tonalite-granodiorite crystal mush hybridization in the mid crust: Mineralogical and geochemical evidence from Variscan appinites (Avila Batholith, Central Iberia). *Lithos* 153, 224-242. https://doi.org/10.1016/j.lithos.2012.03.021

Molina, J. F., Moreno, J. A., Castro, A., Rodríguez, C. & Fershtater, G. B. 2015. Calcic amphibole thermobarometry in metamorphic and igneous rocks: New calibrations based on plagioclase/amphibole Al-Si partitioning and amphibole/liquid Mg partitioning. *Lithos* 232, 286-305. https://doi.org/10.1016/j.lithos.2015.06.027

Molina, J. F., Scarrow, J. H., Montero, P. G. & Bea, F. 2009. High-Ti amphibole as a petrogenetic indicator of magma chemistry: evidence for mildly alkalic-hybrid melts during evolution of Variscan basic–ultrabasic magmatism of Central Iberia. *Contributions to Mineralogy and Petrology* 158, 69-98. https://doi.org/10.1007/s00410-008-0371-4

Mollo, S., Putirka, K., Iezzi, G., Del Gaudio, P. & Scarlato, P. 2011. Plagioclase-melt (dis)equilibrium due to cooling dynamics: Implications for thermometry, barometry and hygrometry. *Lithos* 125, 221-235. https://doi.org/10.1016/j.lithos.2011.02.008

Nachit, H., Ibhi, A., Abia, E. H., Ben Ohoud & M. 2005. Discrimination between primary magmatic biotites, reequilibrated biotites and neoformed biotites. *Comptes Rendus Geoscience* 337, 1415–1420. https://doi.org/10.1016/j.crte.2005.09.002

Nédélec, A. & Bouchez, J.-L. 2015. *Granites: Petrology, Structure, Geological Setting, and Metallogeny*. Oxford University Press, Oxford.

Neves, S. P., Araújo, A. M. B., Correia, P. B. & Mariano, G. 2003. Magnetic fabrics in the Cabanas Granite (NE Brazil): interplay between emplacement and regional fabrics in a

dextral transpressive regime. *Journal of Structural Geology* 25, 441-453. https://doi.org/10.1016/S0191-8141(02)00003-2

Olivier, P., Druguet, E., Castaño, L. M. & Gleizes, G. 2016. Granitoid emplacement by multiple sheeting during Variscan dextral transpression: The Saint-Laurent – La Jonquera pluton (Eastern Pyrenees). *Journal of Structural Geology* 82, 80-92. https://doi.org/10.1016/j.jsg.2015.1b.d.l.6

Pankhurst, R. J., Weaver, S. D., Hervé, F. & Larrondo, P. 1999. Mesozoic-Cenozoic evolution of the North Patagonian Batholith in Aysen, southern Chile. *Journal of the Geological Society* 156, 673-694. https://doi.org/10.1144/gsjgs.156.4.0673

Paterson, S. R., Fowler, T. K., Schmidt, K. L., Yoshinobu, A. S., Yuan, E. S. & Miller, R. B. 1998. Interpreting magmatic fabric patterns in plutons. *Lithos* 44(1–2), 53-82.

Payacán, I., Gutiérrez, F., Gelman, S. E., Bachmann, O. & Parada, M. A. 2014. Comparing magnetic and magmatic fabrics to constrain the magma flow record in La Gloria pluton, central Chile. *Journal of Structural Geology* 69, 32-46. https://doi.org/10.1016/j.jsg.2014.09.015

Pesce, A. H. 1981. Estratigrafía de las nacientes del río Neuquén y Nahuever, Provincia del Neuquén. In *Actas 8º Congreso Geológico Argentino*, pp. 439-455.

Putirka, K. 2016. Amphibole thermometers and barometers for igneous systems and some implications for eruption mechanisms of felsic magmas at arc volcanoes. *American Mineralogist* 101, 841-858. https://doi.org/10.2138/am-2016-5506

Ramos, V. 1999. Rasgos estructurales del territorio argentino. In *Geología Argentina*. Buenos Aires, pp. 715-784.

Ramos, V. Mosquera, A., Folguera, A. & García Morabito, E. 2011. Evolución tectónica de los Andes y del Engolfamiento Neuquino adyacente. In *Relatorio Del 18° Congreso Geologico Argentino, Neuquén*, pp. 335-348.

Ramos, V. A., Niemeyer, H., Skarmeta, J. & Muñoz, J. 1982. Magmatic evolution of the Austral Patagonian Andes. *Earth Science Reviews* 18, 411-431. https://doi.org/10.1016/0012-8252(82)90047-2

Rapela, C. W. & Llambías, E. J. 1985. La secuencia andesítica terciaria de Andacollo, Neuquén, Argentina. In *4º Congreso Geológico Chileno*, pp. 458-488.

Reiners, P. W., Ehlers, T. A. (Eds.), 2005. Low-temperature thermochronolog: Techniques, Interpretations, and Applications. Reviews in Mineralogy & Geochemistry, vol. 58

Riccardi, A. C. & Stipanicic, P. N. 2002. Fase diastrófica Río Atuel. In *Léxico Estratigráfico de La Argentina. Triásico* (eds P. N. Stipanicic & C. A. Marsicano), p. 245. Asociación Geológica Argentina, Buenos Aires.

Ridolfi, F., Puerini, M., Renzulli, A., Menna, M. & Toulkeridis, T. 2008. The magmatic feeding system of El Reventador volcano (Sub-Andean zone, Ecuador) constrained by texture, mineralogy and thermobarometry of the 2002 erupted products. *Journal of Volcanology and Geothermal Research* 176, 94-106. https://doi.org/10.1016/j.jvolgeores.2008.03.003

Ridolfi, F. & Renzulli, A. 2012. Calcic amphiboles in calc-alkaline and alkaline magmas: thermobarometric and chemometric empirical equations valid up to 1,130°C and 2.2 GPa. *Contributions to Mineralogy and Petrology* 163, 877-895. https://doi.org/10.1007/s00410-011-0704-6

Ridolfi, F., Renzulli, A. & Puerini, M. 2010. Stability and chemical equilibrium of amphibole in calc-alkaline magmas: an overview, new thermobarometric formulations and application to subduction-related volcanoes. *Contributions to Mineralogy and Petrology* 160, 45-66. https://doi.org/10.1007/s00410-009-0465-7

Rochette, P., Aubourg, C. & Perrin, M. 1999. Is this magnetic fabric normal? A review and case studies in volcanic formations. *Tectonophysics* 307, 219-234. https://doi.org/10.1016/S0040-1951(99)00127-4

Rochette, P., Jackson, M. & Aubourg, C. 1992. Rock magnetism and the interpretation of anisotropy of magnetic susceptibility. *Reviews of Geophysics* 30, 209. https://doi.org/10.1029/92RG00733

Rovere, E. I., Caselli, A., Tourn, S., Leanza, H. A., Hugo, C. A., Folguera, A., Escosteguy, L., Geuna, S., González, R., Colombino, J. & Danieli, J. C. 2004. *Hoja Geológica 3772- IV, Andacollo, provincia del Neuquén*, Boletín 26. ed. Instituto de Geología y Recursos Minerales. Servicio Geológico Minero Argentino, Buenos Aires.

Sagripanti, L., Folguera, A., Giménez, M., Rojas Vera, E. A., Fabiano, J. J., Molnar, N., Fennell, L. & Ramos, V. A. 2014. Geometry of Middle to Late Triassic extensional deformation pattern in the Cordillera del Viento (Southern Central Andes): A combined field and geophysical study. *Journal of Iberian Geology* 40, 349-366. https://doi.org/10.5209/rev_JIGE.2014.v40.n2.45305

Sánchez, N. P., Coutand, I., Turienzo, M., Lebinson, F., Araujo, V. & Dimieri, L. 2018. Tectonic Evolution of the Chos Malal Fold-and-Thrust Belt (Neuquén Basin, Argentina) From (U-Th)/He and Fission Track Thermochronometry. *Tectonics* 37, 1907-1929. https://doi.org/10.1029/2018TC004981

Schmidt, M. W. 1992. Amphibole composition in tonalite as a function of pressure: an experimental calibration of the Al-in-hornblende barometer. *Contributions to Mineralogy and Petrology* 110, 304-310. https://doi.org/10.1007/BF00310745

Siégel, C., Bryan, S. E., Allen, C. M. & Gust, D. A. 2018. Use and abuse of zircon-based thermometers: A critical review and a recommended approach to identify antecrystic zircons. *Earth-Science Reviews* 176, 87-116. https://doi.org/10.1016/j.earscirev.2017.08.011

Sigismondi, M. E. 2013. Estudio de la deformacion litosférica de la cuenca Neuquina: Estructura termal, datos de gravedad y sísmica de reflexion. Facultad de Ciencias

Exactas y Naturales. Universidad de Buenos Aires. http://digital.bl.fcen.uba.ar/Download/Tesis/Tesis_5361_Sigismondi.pdf

Sigismondi, M., & Ramos, V. A. 2009a. El flujo de calor de la cuenca neuquina, Argentina, segunda parte. Instituto Argentino del Petróleo y Gas, Petrotecnia, 2(9), 58–76.

Sigismondi, M., & Ramos, V. A. 2009b. El flujo de calor de la cuenca Neuquina, Argentina, primera parte (Vol. 1, pp. 64–81). Instituto Argentino del Petroleo y Gas., p. 662.

Somoza, R., Tomlinson, A. J., Zaffarana, C. B., Singer, S. E., Puigdomenech Negre, C. G., Raposo, M. I. B. & Dilles, J. H. 2015. Tectonic rotations and internal structure of Eocene plutons in Chuquicamata, northern Chile. *Tectonophysics* 654, 113-130. https://doi.org/10.1016/j.tecto.2015.05.005

Spagnuolo, M. G., Folguera, A., Litvak, V., Rojas Vera, E. A. & Ramos, V. A. 2012. Late Cretaceous arc rocks in the Andean retroarc region at 36.5°S: Evidence supporting a Late Cretaceous slab shallowing. *Journal of South American Earth Sciences* 38, 44-56. https://doi.org/10.1016/j.jsames.2012.05.002

Stevenson, C. 2009. The relationship between forceful and passive emplacement: The interplay between tectonic strain and magma supply in the Rosses Granitic Complex, NW Ireland. *Journal of Structural Geology* 31, 270-287. https://doi.org/10.1016/j.jsg.2008.11.009

Stipanicic, P. N. 1966. El Jurásico en Vega de la Veranada (Neuquén), el Oxfordense y el diastrofismo Divesiano (Agassiz-Yaila) en Argentina. *Revista de la Asociación Geológica Argentina* 20, 403-478.

Suárez, M. & de la Cruz, R. 1997. Volcanismo pliniano del Lías durante los inicios de la cuenca de Neuquén, Cordillera del Viento, Neuquén, Argentina. In *Actas 7º Congreso Geológico Chileno. Concepción*, Vol. 1, pp. 266-270.

Tischendorf, G., Gottesmann, B., Förster, H.-J. & Trumbull, R. B. 1997. On Li-bearing micas: estimating Li from electron microprobe analyses and an improved diagram for graphical

representation. *Mineralogical Magazine* 61, 809-834. https://doi.org/10.1180/minmag.1997.061.409.05

Tobisch, O. T., McNulty, B. A. & Vernon, R. H. 1997. Microgranitoid enclave swarms in granitic plutons, central Sierra Nevada, California. *Lithos* 40, 321-339. https://doi.org/10.1016/S0024-4937(97)00004-2

Turienzo, M., Sánchez, N., Lebinson, F. & Dimieri, L. 2018. The Structure of the Southern Central Andes (Chos Malal Fold and Thrust Belt). In *The Evolution of the Chilean-Argentinean Andes*, pp. 411-441. Springer. https://doi.org/10.1007/978-3-319-67774-3_17

Vergani, G. D., Tankard, A. J., Belotti, H. J. & Welsink, H. J. 1995. Tectonic Evolution and Paleogeography of the Neuquén Basin, Argentina. In *Petroleum Basins of South America: AAPG Memoir 62*, pp. 383-402. https://doi.org/https://doi.org/10.1306/M62593C19

Vernon, R. H. 2010. Granites Really Are Magmatic: Using Microstructural Evidence to Refute Some Obstinate Hypotheses. *Journal of the Virtual Explorer* 35, 1-36. https://doi.org/10.3809/jvirtex.2011.00264

Vernon, R. H. 1990. Crystallization and hybridism in microgranitoid enclave magmas: Microstructural evidence. *Journal of Geophysical Research* 95, 17849. https://doi.org/10.1029/JB095iB11p17849

Wack, M. R., Gilder, S. A. 2012. The SushiBar: An automated system for paleomagnetic investigations. *Geochemistry, Geophysics, Geosystems* 13, 1-24. https://doi.org/10.1029/2011GC003985

Wagner, M., Altherr, R., Van den haute, P. 1992. Apatite fission-track analysis of Kenyan basement rocks: constraints on the thermotectonic evolution of the Kenya dome. A reconnaissance study. *Tectonophysics* 204, 93-110. https://doi.org/10.1016/0040-

1951(92)90272-8

Wones, D. R. & Eugster, H. P. 1965. Stability of Biotite: Experiment, Theory, and Application. *The American Mineralogist* 50, 1228-1272.

Wyllie, P. J., Cox, K. G. & Biggar, G. M. 1962. The Habit of Apatite in Synthetic Systems and Igneous Rocks. *Journal of Petrology* 3, 238-243. https://doi.org/10.1093/petrology/3.2.238

Yavuz, F. 2003. Evaluating micas in petrologic and metallogenic aspect: I–definitions and structure of the computer program MICA+. *Computers & Geosciences* 29, 1203-1213. https://doi.org/10.1016/S0098-3004(03)00142-0

Zaffarana, C. B., Somoza, R., Orts, D. L., Mercader, R., Boltshauser, B., González, V. R. & Puigdomenech, C. 2017. Internal structure of the Late Triassic Central Patagonian batholith at Gastre, southern Argentina: Implications for pluton emplacement and the "Gastre fault system." *Geosphere* 13, 1973-1992. https://doi.org/10.1130/GES01493.1

Zaffarana, C. B., Somoza, R. & López de Luchi, M. 2014. The Late Triassic Central Patagonian Batholith: Magma hybridization, $^{40}Ar/^{39}Ar$ ages and thermobarometry. *Journal of South American Earth Sciences* 55, 94-122. https://doi.org/10.1016/j.jsames.2014.06.006

Žák, J., Schulmann, K. & Hrouda, F. 2005. Multiple magmatic fabrics in the Sázava pluton (Bohemian Massif, Czech Republic): a result of superposition of wrench-dominated regional transpression on final emplacement. *Journal of Structural Geology* 27, 805-822. https://doi.org/10.1016/j.jsg.2005.01.012

Zamora Valcarce, G. 2007. Estructura y Cinemática de la Faja Plegada y Corrida del Agrio, Cuenca Neuquina. PhD Thesis. Universidad de Buenos Aires. Published thesis.

Zamora Valcarce, G., Zapata, T. & Ramos, V. A. 2011. La Faja Plegada y Corrida del Agrio. In *Relatorio Del XVIII Congreso Geológico Argentino, Neuquén*, pp. 367-374.

Zanettini, J. C. M., Santamaría, G. R. & Leanza, H. 2001. *Hoja Geológica 3772-II, Las Ovejas.*

Provincia del Neuquén. Instituto de Geología y Recursos Minerales. Servicio Geológico Minero Argentino, Buenos Aires.

Zappettini, E., Korzeniewski, L. I. & Segal, S. 2014. Nuevos datos de las mineralizaciones polimetálicas del distrito Varvarco, Neuquén. In *19º Congreso Geológico Argentino, Córdoba*. pp. S6-4.

Zappettini, E., Méndez, V. & Zanettini, J. C. 1987. Metasedimentitas mesopaleozoicas en el noroeste de la Provincia del Neuquén. *Revista de la Asociación Geológica Argentina* 42, 206-207.

Zappettini, E. O., Chernicoff, C. J., Santos, J. O. S., Dalponte, M., Belousova, E. & McNaughton, N. 2012. Retrowedge-related Carboniferous units and coeval magmatism in the northwestern Neuquén province, Argentina. *International Journal of Earth Sciences* 101, 2083-2104. https://doi.org/10.1007/s00531-012-0774-3

Zappettini, E. O., Cozzi, G., Dalponte, M., Godeas, M., Korzeniewski, L. I., Peroni, J., Segal, S. & Castro Godoy, S. 2021. *Análisis Geológico y Metalogenético del Sector Norte de la Cordillera del Viento, provincia del Neuquén*. Instituto de Geología y Recursos Minerales, Servicio Geológico Minero Argentino. Serie Contribuciones Técnicas Recursos Minerales Nº44, 51 pp. Buenos Aires.

Zappettini, E. O., Lagorio, S. L., Dalponte, M., Orestes, J. & Belousova, E. 2018. Evidencias de magmatismo precuyano (Pliensbachiano - Toarciano) en el norte de la Cordillera del Viento, provincia del Neuquén: caracterización geoquímica, isotópica e implicancias tectónicas. *Revista de La Asociación Geológica Argentina* 75(4), 533-558.

Figures

Figure 1: Regional geological map of the Southern Central Andes. Ages for intrusive and volcanic rocks are listed in Supplementary Table S1. Black rectangle indicates study area (Figures 2A and 2B). The Naunauco Belt is marked with a grey dotted line, it comprises both plutonic rocks of Late Cretaceous-Paleogene age and volcanic rocks of Paleocene-Eocene age. Numbers indicate ages obtained by different methods, as shown in legend.

Figure 2: Local (a) and regional (b) maps of the study area. The maps are based on Zanettini *et al*. (2001), Ramos *et al*. (2011), Giacosa *et al*. (2014), and Sagripanti *et al*. (2014). Black rectangle indicates the area in Figure 3, and red rectangle indicates the area of Figure 12.

Figure 3: ASTER images of the study area: (a) RGB: 4 6 1 and (b) RGB: 7 4 14. VT: Varvarco Tonalite, GN: Guaracó Norte Formation.

Figure 4: QAP ternary diagram for Varvarco Intrusives and Jurassic Host Granite.

Figure 5: Outcrops of the Guaracó Norte Formation, Jurassic Host Granites and Varvarco Intrusives. (a) View towards the SE from Puesto Hernández, Chacay creek area, with the outcrops of the Varvarco Tonalite, Radales Aplite and the Guaracó Norte Formation. b) Outcrops of the Jurassic Host Granites in the Manzano creek area c) Leucocratic dyke assigned to the Radales Aplite in the Manzano creek area d) Xenolith of Guaracó Norte Formation in the Jurassic Host Granites and e) Plagioclase phenocrysts in granophyric matrix for the Jurassic Host Granites (cross-polarised light).

Figure 6: Outcrop images of the Varvarco Tonalite. (a) Thin leucocratic vein intruding the Varvarco Tonalite in the Chacay creek area. (b) Mafic microgranular enclave. (c) Partially

dissolved (corroded) enclave in a hybrid magma of the Varvarco Tonalite. (d) Disintegrated quartz-dioritic dykes in the Varvarco Tonalite, where different degrees of hybridisation are observed.

Figure 7: Petrographic image of the Varvarco Tonalite in cross-polarised light. (a) Plagioclase (Pl) with cores of more calcic composition and lighter rims of more sodic composition. (b) Euhedral plagioclase crystals included in anhedral K-feldspar (Kfs; orthoclase) crystals. (c) Euhedral plagioclase and subhedral amphibole (Amp) and biotite (Bt). (d) Biotite, amphibole and titanomagnetite (Ti-mag) concentrated in blocks in the Varvarco Tonalite. Other mineral abbreviations: Qtz: quartz.

Figure 8: Quartz-dioritic dykes intruding the Varvarco Tonalite and Radales Aplite. (a) Fine-grained texture of a quartz-dioritic dykes. (b) Plagioclase phenocrysts in a fine-grained matrix mainly composed of plagioclase. (c) Amphibole phenocryst with inclusions of plagioclase and opaque minerals. (d) Rounded quartz xenocryst rimmed by amphibole and opaque minerals (quartz ocelli). (e) Contact between the Radales Aplite and the hosting Guaracó Norte Formation. (f) Xenolith of Guaracó Norte Formation in the Radales Aplite. Mineral abbreviations as in Fig. 7.

Figure 9: Outcrops and petrographic images of the Butalón Tonalite in cross-polarised light. (a) Felsic aplitic vein intruding the Butalón Tonalite. (b) Mafic microgranular enclaves. (c) Amphibole megacryst with inclusions of plagioclase and biotite. (d) Mafic minerals. Mineral abbreviations as in Fig. 7 and Op: opaque minerals.

Figure 10: Plagioclase and amphibole compositional classification. (a) and (b) Plagioclase zoning profiles for the Varvarco Tonalite. (c) and (d) Photomicrographs with cross-polarised light showing some analysed spots of amphibole (red), biotite (green) and plagioclase (yellow). (e) Amphibole classification diagrams of Leake *et al*. (1997). (f) Al^{IV} vs. $Al^{VI} + Fe^{+3} + 2Ti$ +"A″ graph (Kawakatsu & Yamaguchi, 1987), shows that nearly all amphiboles have a good 1:1 fit between vertical and horizontal axes. This suggests that charge compensation due to the introduction of Al^{IV} was accomplished by both the edenitic and tschermakitic substitutions.

Figure 11: Biotite compositional classification. (a) Biotite classification (Al^{IV} as a function of its Fe/(Fe+Mg) ratio; Deer *et al*. 2013). (b) Biotite discrimination diagram after Foster (1960). (c) Trioctahedrical classification diagram after Tischendorf *et al*. (1997). (d) Ternary diagram for discriminating between primary magmatic biotites and re-equilibrated and secondary biotites after Nachit *et al*. (2005).

Figure 12: (a) Map showing magnetic foliation planes (K1-K2 planes), defined as the plane perpendicular to K3 in the Varvarco Tonalite. Inset shows K3 distribution of the magmatic foliations. (b) Map showing magnetic lineation (K1 direction) in the Varvarco Tonalite. Inset shows K1 distribution of the magmatic fabrics. The stereonets represent contoured Kamb equal-area lower-hemisphere stereographic projections made with the software Stereonet 9.9.5 (Allmendinger *et al*. 2012; Cardozo & Allmendinger, 2013). The scale represents Kamb contours in standard deviation.

Figure 13: Domain state of the magnetite of the Varvarco Tonalite and Jurassic Host Granites. Diagram of Day *et al*. (1977). Hc = coercive force, Ms = saturation magnetisation and Mr =

remanent magnetisation, SD = single-domain, PSD = pseudo-single domain, MD = multidomain.

Figure 14: Comparison of AMS and of AARM ellipsoids showing that magnetite and paramagnetic minerals have fabrics with the same orientations. Equal area projection in geographic coordinate system.

Figure 15: Apatite fission track data of samples (a) VAR 5 and (b) BU4. Diagrams on the left of the figure show the radial distribution of ages of each grain, where the central age is marked in blue. Diagrams on the right, show the frequency histogram for obtained ages.

Figure 16: Schematic magma hybridisation processes proposed for the Varvarco Tonalite, based on the model of Barbarin (2005).

Figure 17: Geochemical signature of the magmas in equilibrium with amphibole and biotite from the Varvarco Tonalite. (a) to (d) Amphibole compositions of the Varvarco Tonalite plotted on the diagrams of Molina *et al*. (2009). (a) MgO vs. TiO_2. (b) Na_2O/K_2O vs. TiO_2. (c) Al_2O_3 vs. TiO_2. (d) TiO_2 vs. Temperature calculated using geothermometer of Putirka (2016). (e) and (f) Tectonic discrimination diagrams for biotites of the Varvarco Tonalite: (e) Al_2O_3 vs MgO and f) Al_2O_3 vs FeO_T (Abdel-Rahman, 1994).

Figure 18: Oxygen fugacity conditions of the magmas in equilibrium with the amphiboles and biotites of the Varvarco Tonalite. Data by Zaffarana *et al*. (2014) and Castro *et al*. (2011) are plotted for comparison. (a) log$fO2$ vs. temperature diagram by Ridolfi *et al*. (2010). Error bars

represent maximum log$fO2$ errors of 0.4 log unit and the expected σ (22 °C). (b) Diagram of Anderson & Smith (1995) showing the effect of $fO2$ on amphibole compositions in terms of $Fe_T/(Fe_T + Mg)$ vs. Al^{IV} (a.p.f.u.). (c) Ternary diagram for oxygen fugacity in biotites (Wones and Eugster, 1965). (d) logfO_2 vs T diagram (Wones & Eugster, 1965). Numbers represent 100*Mg/(Mg+Fe) ratios in biotites. Yellow circle shows an average of all biotite compositiosn from this study. Biotites by Zaffarana *et al*. (2014) overlaps with the yellow circle. Biotites by Castro *et al*. (2011) is shown in grey oval. Oxygen fugacity buffers are nickel-nickel oxide (NNO), hematite-magnetite (HM), quartz-fayalite-magnetite (QFM).

Figure 19: Cooling history of the Varvarco Tonalite. See main text for details.

Tables

Table 1: AMS sites of the Varvarco, Radales and Butalón plutons, Jurassic Host Granites and of the Guaracó Norte Formation. GPS data is given in latitude and longitude. N is the number of samples used in statistics. Km=(K1+K2+K3)/3 is the mean magnetic susceptibility (SI units). L is the magnetic lineation (K1/K3); F is the magnetic foliation (K2/K3); P is the degree of anisotropy (Jelinek, 1981); T=(lnF − lnL)/(lnF + lnL) is the Jelinek's parameter (Jelinek, 1981). K1, K2 and K3 are mean AMS eigenvectors which represent the maximum, intermediate and minimum susceptibility intensities, respectively. Dec, declination in degrees; Inc, inclination in degrees; C1a and C1b are the semiangles of the major and minor axes of the 95% confidence ellipse, respectively, calculated by the bootstrap method.

Site	Litology	GPS data	N	Kaver	K1d	K1i	C1a	C1b	K2d	K2i	C2a	C2b
V1	Varvarco Tonalite (main facies)	36^{0}48´36.1" S; 70^{0}40´14.6" W	5	5.98E-02	143.2	74.5	8.3	3.5	337.7	15.1	9.9	2.9
V2		36^{0}48´36.3" S; 70^{0}40´09.5" W	5	1.86E-02	137.2	47.8	23.9	19.5	5.2	31.2	32.4	20.5
V3		36^{0}48´36.4" S; 70^{0}40´04.3" W	7	1.15E-02	323.2	3.5	20.8	9.9	53.8	8.6	21.0	8.5
V6		36^{0}48´23.8" S; 70^{0}40´03.2" W	6	4.70E-02	68.7	59.2	18.6	6.7	338.0	0.4	33.5	8.4
V7		36^{0}48´15.7" S; 70^{0}39´55.0" W	6	1.23E-02	63.7	61.2	11.0	4.9	306.1	14.3	49.5	10.4
V8		36^{0}48´58.7" S; 70^{0}40´20.2" W	5	4.20E-02	124.9	53.5	21.6	10.3	28.3	4.9	21.6	16.4
V9		36^{0}48´47.8" S; 70^{0}40´15.1" W	7	6.49E-02	135.9	53.3	30.0	13.0	353.4	30.6	34.1	14.7
V17		36^{0}49´11.1" S; 70^{0}40´26.1" W	6	4.35E-02	119.1	50.6	40.1	4.9	219.8	8.7	39.5	11.9
V4	Qtz-dioritic dyke (Varvarco Tonalite)	36^{0}48´35.8" S; 70^{0}40´05.4" W	5	4.74E-02	119.7	38.3	12.0	3.8	329.5	47.7	13.5	3.6
V14	Butalón Tonalite	36^{0}57´46.0" S; 70^{0}41´12.0" W	5	3.74E-02	305.5	64.7	6.7	2.8	105.6	24.0	9.0	5.0
V15		36^{0}58´16.3" S; 70^{0}40´57.7" W	5	4.39E-02	191.5	14.9	46.7	7.2	64.3	66.2	46.7	15.2
V16		36^{0}59´03.2" S; 70^{0}41´24.9" W	5	4.94E-02	129.5	65.0	11.5	2.2	269.2	19.6	15.0	9.2
V5	Radales Aplite	36^{0}48´36.8" S; 70^{0}40´02.3" W	5	2.37E-03	152.7	50.6	20.2	7.1	318.2	38.5	20.7	10.2
V10	Jurassic Host Granites	36^{0}50´42.1" S; 70^{0}40´14.0" W	5	9.53E-04	120.0	33.5	30.4	12.1	261.7	49.9	46.0	12.7
V11		36^{0}50´42.1" S; 70^{0}40´14.0" W	5	3.16E-02	19.3	40.2	3.0	1.0	154.7	40.1	16.5	2.7
V12		36^{0}50´46.3" S; 70^{0}39´45.3" W	5	2.80E-02	135.5	30.2	22.1	4.1	4.2	48.7	21.8	6.4

V13	Guaracó Norte Fm.	36^{0}50´48.5" S; 70^{0}39´54.5" W	5	4.40E-04	92.4	63.6	55.2	6.2	331.2	14.5	55.4	10.6

K3d	K3i	C3a	C3b	K1	K2	K3	Lmean	Fmean	Pmean	Pjmean	Tmean
246.7	3.7	6.6	4.1	1.087	0.982	0.931	1.107	1.055	1.167	1.170	-0.312
258.6	25.3	32.7	15.9	1.023	0.997	0.980	1.026	1.017	1.044	1.044	-0.189
211.2	80.7	10.9	7.9	1.019	0.999	0.982	1.019	1.018	1.037	1.037	-0.051
247.7	30.8	31.9	6.2	1.050	0.986	0.963	1.065	1.024	1.091	1.094	-0.457
209.4	24.4	49.5	5.1	1.069	0.980	0.951	1.090	1.031	1.124	1.129	-0.478
294.7	36.1	18.9	3.3	1.049	1.017	0.934	1.031	1.089	1.123	1.128	0.479
252.1	18.3	25.6	9.4	1.039	1.004	0.957	1.035	1.049	1.086	1.086	0.154
316.6	38.1	12.9	10.1	1.035	1.014	0.951	1.020	1.067	1.088	1.093	0.524
222.1	15.2	10.2	5.6	1.048	1.005	0.946	1.043	1.063	1.108	1.108	0.185
199.0	7.6	9.2	4.8	1.037	1.006	0.957	1.031	1.051	1.084	1.084	0.250
286.5	18.1	15.4	7.1	1.013	1.005	0.982	1.008	1.024	1.032	1.034	0.522
4.6	14.9	13.5	2.3	1.038	1.005	0.957	1.033	1.050	1.084	1.084	0.202
53.9	7.2	12.0	8.3	1.025	1.004	0.971	1.021	1.033	1.055	1.055	0.220
16.5	19.4	43.6	8.0	1.016	0.998	0.986	1.018	1.013	1.031	1.031	-0.151
267.0	24.2	16.5	1.4	1.066	0.983	0.951	1.084	1.034	1.121	1.125	-0.420
241.5	25.4	11.3	3.2	1.015	1.006	0.979	1.009	1.029	1.037	1.039	0.533
235.3	21.6	15.1	6.0	1.008	1.005	0.987	1.003	1.018	1.021	1.023	0.681

Table 2: Mineral compositions analysed by electron microprobe in the Varvarco Tonalite. a) Plagioclases (Pl). b) Amphiboles (Amp). c) Biotites (Bt). In this table the results given by amphibole-only thermometers of Ridolfi *et al*. (2010) (equation 1), Ridolfi & Renzulli (2012) (equation 2) and Putirka (2016) (equation 5) were added, as well as the results from the geothermometers of Ridolfi *et al*. (2010) (equation 4) and Ridolfi & Renzulli (2012) (average between equations 1a and 1b). In table 2c, temperatures are calculated with the geothermometer of Henry *et al*. (2005).

Table 2a

Mineral	Pl	Pl	Pl	Pl	Pl	Pl	Pl	Pl	Pl	Pl	Pl
Texture	rim	centre	rim	centre	centre	centre	rim	rim	rim	centre	centre
Analysis	9	10	21	22	25	26	27	28	31	32	33
SiO_2	59.32	56.99	60.05	54.44	52.57	52.87	52.91	58.91	57.07	55.46	55.95
TiO_2	b.d.l.	0.02	0.02	b.d.l.	0.03	b.d.l.	b.d.l.	b.d.l.	b.d.l.	0.01	0.03
Al_2O_3	24.73	26.62	24.48	28.08	29.31	29.15	29.19	25.68	26.79	28.12	27.38
Cr_2O_3	b.d.l.	b.d.l.	b.d.l.	b.d.l.	b.d.l.	b.d.l.	b.d.l.	b.d.l.	0.05	b.d.l.	0.03
NiO	b.d.l.	0.06	b.d.l.	0.04	0.02	b.d.l.	b.d.l.	b.d.l.	b.d.l.	b.d.l.	b.d.l.
FeO_t	0.21	0.14	0.26	0.39	0.14	0.17	0.19	0.16	0.18	0.18	0.18
MnO	0.01	0.01	b.d.l.	0.05	b.d.l.	0.01	0.01	0.01	0.01	0.01	b.d.l.
MgO	0.02	b.d.l.	b.d.l.	b.d.l.	b.d.l.	b.d.l.	0.01	b.d.l.	0.02	0.01	b.d.l.
CaO	7.11	9.11	6.35	11.03	12.46	12.40	12.24	7.69	8.68	10.42	9.84
Na2O	7.53	6.45	7.90	5.38	4.57	4.74	4.66	7.24	6.58	5.78	5.90
K_2O	0.36	0.26	0.44	0.20	0.15	0.15	0.16	0.32	0.23	0.24	0.33
TOTAL	99.37	99.78	99.50	99.78	99.32	99.62	99.48	100.06	99.66	100.31	99.70
xAN	33.61	43.18	30.01	52.48	59.60	58.62	58.65	36.33	41.61	49.24	47.05

Pl	Pl	Pl	Pl	Pl	Pl	Pl	Pl	Pl	Pl	Pl
centre	centre	centre	centre	centre	rim	centre	centre	centre	centre	centre
34	35	36	37	38	39	40	41	42	43	44
55.99	54.18	53.53	55.05	54.34	59.03	56.32	52.01	55.35	54.76	55.80
0.03	b.d.l.	b.d.l.	b.d.l.	0.01	b.d.l.	b.d.l.	b.d.l.	b.d.l.	0.02	0.01
27.07	28.09	28.75	28.65	28.61	25.19	26.68	30.20	27.75	28.02	27.68
b.d.l.	0.01	0.05	b.d.l.	0.01	b.d.l.	b.d.l.	b.d.l.	0.01	0.01	0.01
b.d.l.	0.01	b.d.l.	b.d.l.	b.d.l.	b.d.l.	0.02	b.d.l.	b.d.l.	b.d.l.	b.d.l.
0.17	0.17	0.14	0.15	0.21	0.16	0.16	0.15	0.11	0.16	0.17
b.d.l.	b.d.l.	0.02	b.d.l.	0.04	b.d.l.	b.d.l.	b.d.l.	0.01	b.d.l.	0.02
b.d.l.	b.d.l.	0.01	0.01	0.02	0.01	b.d.l.	b.d.l.	b.d.l.	0.01	0.01
9.73	10.95	11.35	11.10	11.19	7.63	9.48	13.50	10.55	10.74	10.36

5.99	5.39	5.11	5.39	5.17	7.33	6.12	3.88	5.54	5.57	5.91
0.29	0.26	0.22	0.22	0.19	0.24	0.27	0.13	0.22	0.22	0.24
99.31	99.17	99.23	100.62	99.93	99.68	99.16	99.99	99.62	99.58	100.32
46.52	52.10	54.43	52.56	53.87	36.02	45.40	65.33	50.63	50.94	48.55

Pl	Pl	Pl	Pl	Pl	Pl	Pl	Pl	Pl
centre	centre	centre	rim	centre	rim	rim	rim	centre
45	46	59	60	66	67	71	73	74
55.41	56.54	53.25	56.55	47.90	56.36	56.42	55.68	53.65
b.d.l.	b.d.l.	0.01	0.02	0.02	0.02	b.d.l.	b.d.l.	0.03
27.94	27.01	29.05	26.85	32.50	27.74	27.07	27.07	26.99
0.02	b.d.l.	b.d.l.	0.01	b.d.l.	0.01	b.d.l.	b.d.l.	b.d.l.
b.d.l.	b.d.l.	0.01	b.d.l.	0.04	b.d.l.	0.04	0.07	0.04
0.17	0.21	0.21	0.31	0.17	0.26	0.22	0.19	0.15
b.d.l.	0.02	b.d.l.	b.d.l.	0.02	0.02	b.d.l.	b.d.l.	b.d.l.
b.d.l.	0.01	0.01	0.01	0.01	b.d.l.	0.01	0.01	0.01
10.25	9.50	11.93	9.06	16.01	9.39	9.45	9.31	10.57
5.79	6.14	4.88	6.48	2.41	6.17	6.11	6.10	5.18
0.19	0.25	0.17	0.23	0.08	0.18	0.26	0.19	0.21
99.84	99.77	99.57	99.57	99.26	100.16	99.65	98.71	96.89
48.89	45.45	56.90	43.05	78.23	45.23	45.40	45.26	52.34

Table 2b

Mineral	Amp	Amp	Amp	Amp	Amp	Amp	Amp	Amp	Amp	Amp
Analysis	2	3	4	5	6	13	14	16	47	48
Texture	rim	centre	centre	centre	rim			centre	centre	centre
SiO_2	50.36	48.50	49.33	51.13	49.59	50.77	52.85	53.83	43.37	43.64
TiO_2	0.40	0.65	0.43	0.33	0.36	0.22	0.16	0.12	1.61	1.69
Al_2O_3	3.85	5.30	4.42	3.69	4.12	3.65	1.80	1.26	8.45	8.39
Cr_2O_3	0.02	0.01	0.02	0.03	0.01	b.d.l.	0.04	0.03	b.d.l.	b.d.l.
NiO	b.d.l.	0.04	b.d.l.	0.06	b.d.l.	b.d.l.	b.d.l.	b.d.l.	b.d.l.	0.05
FeO_t	17.38	17.63	17.96	16.01	15.43	16.30	14.41	12.60	17.62	17.66
MnO	1.66	1.57	2.15	1.73	1.34	1.68	1.62	1.37	1.02	0.95
MgO	13.46	12.42	12.72	13.77	13.23	13.51	15.01	15.66	10.33	10.44
CaO	10.21	10.64	9.45	10.98	11.93	11.29	11.17	12.05	11.27	11.36
Na_2O	0.55	0.75	0.58	0.48	0.42	0.40	0.20	0.18	1.19	1.04
K_2O	0.28	0.42	0.29	0.25	0.25	0.24	0.08	0.06	0.76	0.72
TOTAL	98.26	97.97	97.39	98.52	96.79	98.10	97.45	97.21	95.64	96.03
Geothermometers (ºC)										
Ridolfi *et al*. (2010)-Eqn.1	773	800	750	752	717	742	703	672	841	837
Ridolfi & Renzulli (2012)-Eqn.2	343	459	313	470	774	515	449	550	876	851
Amph-only-Putirka (2016)-Eqn.5	666.26	699.34	668.48	668.90	682.23	663.59	639.80	642.81	791.41	785.93
Geobarometers (kbar)										
Ridolfi *et al*. (2010)-	0.5	0.7	0.6	0.5	0.5	0.5	0.3.	0.2	17	17

Eqn.4										
Ridolfi & Renzulli (2012)-Average between Eqn. 1a and Eqn. 1b	1.1	1.4	2.3	1	0.7	0.9	0.6	0.4	2	1.7

Amp	Amp	Amp	Amp	Amp	Amp	Amp	Amp	Amp	Amp	Amp
49	50	54	55	56	61	62	63	65	68	70
rim	rim	rim	centre	centre	centre	centre	centre	centre	centre	rim
51.08	53.53	45.54	44.51	43.84	48.09	48.40	44.60	48.34	44.61	46.33
0.16	0.09	0.66	1.12	1.65	0.96	1.03	1.64	1.16	1.66	0.65
2.55	1.20	6.61	7.74	8.17	6.15	6.20	8.36	6.23	8.63	6.56
0.04	0.03	b.d.l.	b.d.l.	0.04	0.03	0.03	b.d.l.	0.03	b.d.l.	b.d.l.
0.02	0.06	0.06	b.d.l.	b.d.l.	0.04	0.01	b.d.l.	b.d.l.	b.d.l.	b.d.l.
16.07	11.97	18.34	17.84	17.37	14.50	14.10	15.15	14.04	17.51	18.11
1.67	1.34	1.24	1.04	0.94	0.69	0.73	0.69	0.79	0.89	1.06
14.10	15.99	10.53	10.26	10.60	13.76	14.04	12.33	14.06	10.95	10.97
10.67	11.46	11.29	11.24	11.33	11.42	11.08	10.80	11.10	11.24	11.46
0.33	0.13	0.77	0.95	0.99	0.93	1.06	1.44	0.83	1.22	0.79
0.13	0.06	0.63	0.86	0.73	0.42	0.35	0.48	0.41	0.64	0.54
96.87	95.92	95.79	95.59	95.73	97.08	97.14	95.60	97.08	97.47	96.52
837	734	774	808	831	772	769	836	779	835	771
414	464	821	830	850	782	807	872	808	860	787
645.44	641.23	716.56	753.23	781.33	749.50	755.59	813.07	752.52	791.86	716.61
0.3	invalid	11	14	16	9	9	16	9	17	10
0.7	0.4	1.3	1.6	1.6	0.9	1.1	1.9	1	1.9	1.1

Table 2c

Mineral	Bt	Bt	Bt	Bt	Bt	Bt	Bt	Bt	Bt	Bt	Bt	Bt	Bt	Bt
Analysis	1	8	12	17	20	23	30	52	53	58	64	69	72	75
Texture	centre	centre	centre	centre	centre	centre	centre	centre	centre	*	*	centre	*	*
SiO_2	35.95	36.51	35.98	36.07	36.10	36.28	35.87	36.03	34.11	36.36	35.94	35.93	35.34	36.15
TiO_2	3.62	3.83	3.52	2.67	3.21	3.77	4.00	3.36	4.66	4.06	4.09	3.46	3.84	3.99
Al_2O_3	13.62	14.55	14.01	14.12	14.01	13.82	13.87	13.62	13.21	13.82	13.35	13.84	13.48	13.60
Cr_2O_3	0.04	0.03	0.02	0.04	b.d.l.	0.03	0.01	b.d.l.	0.02	b.d.l.	b.d.l.	b.d.l.	b.d.l.	b.d.l.
NiO	0.02	0.01	b.d.l.	b.d.l.	0.03	0.08	b.d.l.	0.02	b.d.l.	0.03	0.01	0.01	0.09	b.d.l.
FeO_t	19.65	18.70	19.63	19.64	20.27	19.68	20.77	20.56	20.66	18.62	17.84	20.60	20.49	17.88
MnO	0.81	0.81	0.69	0.82	0.70	0.72	0.72	0.60	0.58	0.31	0.38	0.63	0.50	0.29
MgO	11.33	11.40	11.50	12.00	11.44	11.48	10.65	11.23	9.96	12.29	12.35	11.07	10.90	12.76

CaO	0.04	0.06	0.01	0.04	0.02	0.03	0.08	0.02	1.16	0.03	0.04	b.d.l.	0.02	0.04
Na_2O	0.08	0.09	0.08	0.10	0.09	0.08	0.08	0.10	0.09	0.15	0.14	0.11	0.11	0.19
K_2O	9.43	9.64	9.65	9.63	9.52	9.47	9.24	9.43	8.63	9.50	9.20	9.61	9.57	9.05
P_2O_5	b.d.l.	b.d.l.	b.d.l.	0.02	b.d.l.	b.d.l.	0.01	0.01	0.03	b.d.l.	b.d.l.	b.d.l.	b.d.l.	b.d.l.
TOTAL	94.59	95.63	95.09	95.15	95.39	95.43	95.29	94.97	93.11	95.18	93.33	95.25	94.34	93.95
T(°C) (Henry et al. 2005)	728.14	733.13	723.56	689.18	709.61	732.41	733.47	715.09	744.45	746.37	753.34	717.22	731.73	751.74

* Small crystal included in amphibole

Table 3: Apatite fission track data. a) Central ages calculated with a calibration of 330.40 ± 20.16 Ma. n: number of measured grains. b) Kinetic parameters.

Sample	Lithology	n	U (ppm)	Dosimeter		Spontaneous		Induced		$P(x)^2$	Age dispersion	Central age (Ma) ± 1s
				ρD	*ND*	ρ_S	N_S	ρi	*N*i			
VAR5	tonalite	21	9.19	8.43	5000	2.61	131	5.61	281	90.72	0	67.5 ± 8.0
BU4	tonalite	13	14.18	8.42	5000	2.95	131	8.48	377	44.37	0.05	50.3 ± 5.8

Table 4: Summary of the temperatures and pressures calculated for the sample of the Varvarco Tonalite. In the amphibole-plagioclase barometer of Molina *et al*. (2015), T1 is the temperature obtained with Ridolfi & Renzulli (2012) geothermometer (equation 5) and T2 with the Putirka (2016) geothermometer (equation 5). Standard deviation of the data is signaled in the appropriate cases.

Sample name				**VARVARCO TONALITE**	
Analysed material				**Centres**	**Rims**
Calibration			**Calibration uncertainty**		
	Amp-Pl thermometer (Molina *et al*. 2021-expression A1 at 5 kbar)		± 50ºC	**623**-691	-
	Amp-Pl thermometer (Molina *et al*. 2021-expression A1 at 1 kbar)		± 50ºC	624-692	-
	Amp-Pl thermometer (Molina *et al*. 2021-expression A2 at 5 kbar)		± 50ºC	636-699	-
	Amp-Pl thermometer (Molina *et al*. 2021-expression A2 at 1 kbar)		± 50ºC	637-699	-
	Amp-Pl thermometer (Molina *et al*. 2021-expression B2)		± 50ºC	641-**703**	-
	Amp-Pl thermometer (Holland & Blundy 1994-expression B)		± 40ºC	784-716	-
	Amphibole data (available in Table 2b)	Amp-only thermometer of Ridolfi *et al*. (2010)-Eqn.1. Average data	± 35ºC	780	742
		Amp-only thermometer of Ridolfi & Renzulli (2012)-Eqn. 2. Average data	± 32ºC	717	614
		Amp-only thermometer of Putirka (2016)-Eqn.5. Average data.	± 30ºC	742	678
	Whole-rock data (calculated with sample BPN11 of Varvarco Tonalite from Kay et al. 2006)	Liquid-only-Molina *et al*. (2015)	± 35 to ± 45ºC	958	
		Liquid-only-Putirka (2016)-Eqn.3	± 33ºC	922	
	Biotite (available in Table 2c)	Henry *et al.* (2005)	± 12ºC	689-753	
Geobarometers (kbar)	Amphibole data (some of them are available in Table 2b)	Hammarstrom & Zen (1986) (average data)	± 3 kbar	3.47	-
		Hollister *et al*. (1987) (average data)	± 1 kbar	3.53	-

		Johnson & Rutherford (1989) (average data)	± 0.5 kbar	2.76	-
		Schmidt (1992) (average data)	± 0.6 kbar	3.99	-
		Ridolfi & Renzulli (2012)-Average between Eqn. 1a and Eqn. 1b	± 2.5 kbar	1.2	0.7
	Amp-Pl barometer (Anderson & Smith 1995)		± 0.6 kbar	3.13-2.26	-
	Amp-Pl barometer (Molina *et al*. 2015) at T1*		± 1.5 to ± 2.3 kbar	3.37-2.28	-
	Amp-Pl barometer (Molina *et al*. 2015) at T2**			2.64-1.83	-
	Amp-Pl barometer (Molina *et al*. 2015) at T3***			3.36-2.15	-

T1* (Ridolfi and Renzulli, 2012, Eqn.2)

T2**(Putirka 2016. Eqn.5)

T3*** (Molina *et al*. 2021-expression B2)

errors are 1 sigma standard deviations

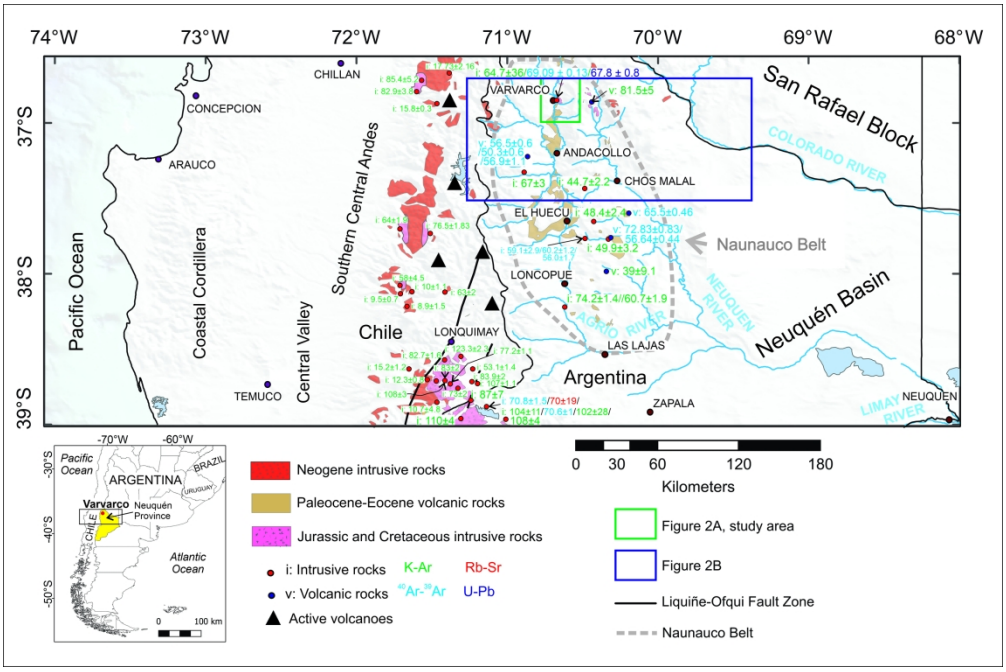

254x168mm (300 x 300 DPI)

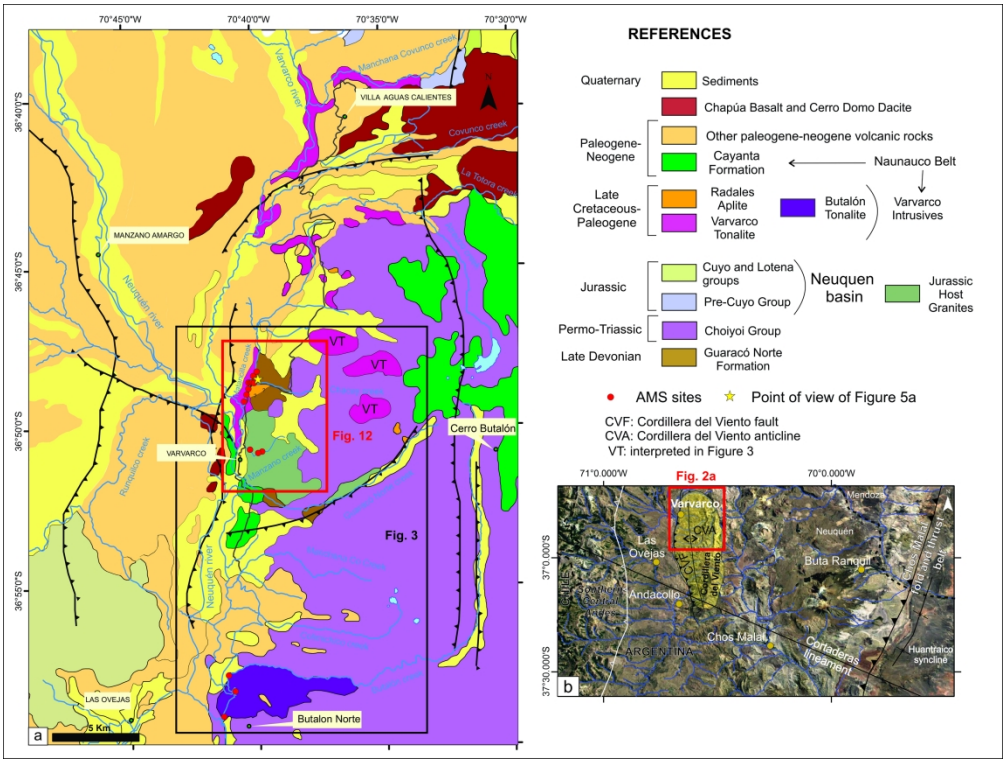

278x210mm (300 x 300 DPI)

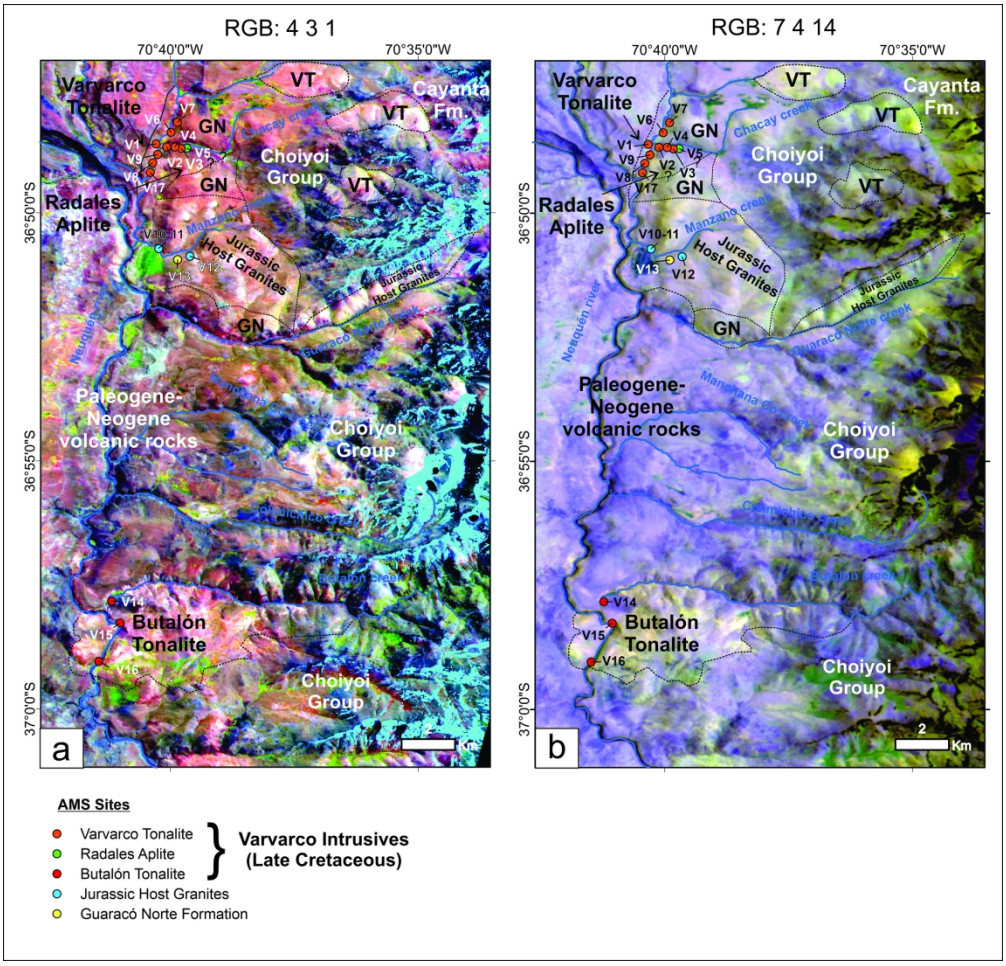

190x182mm (300 x 300 DPI)

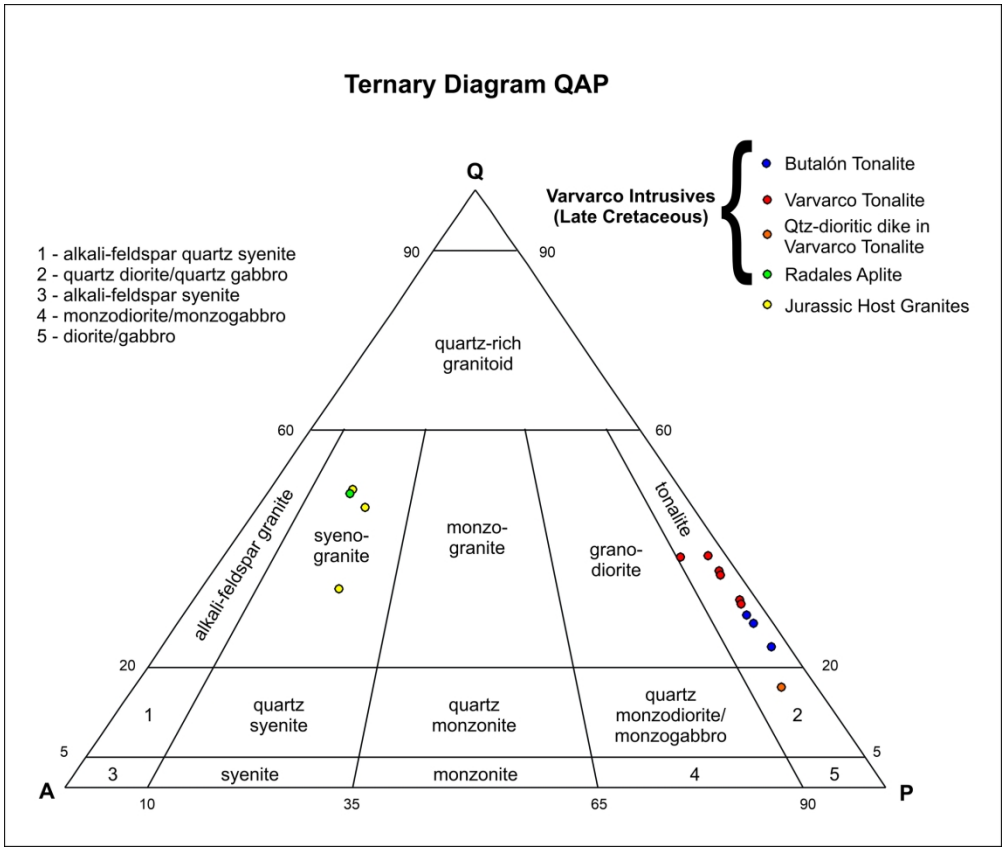

191x161mm (300 x 300 DPI)

GUARACÓ NORTE FORMATION, JURASSIC HOST GRANITES AND VARVARCO INTRUSIVES

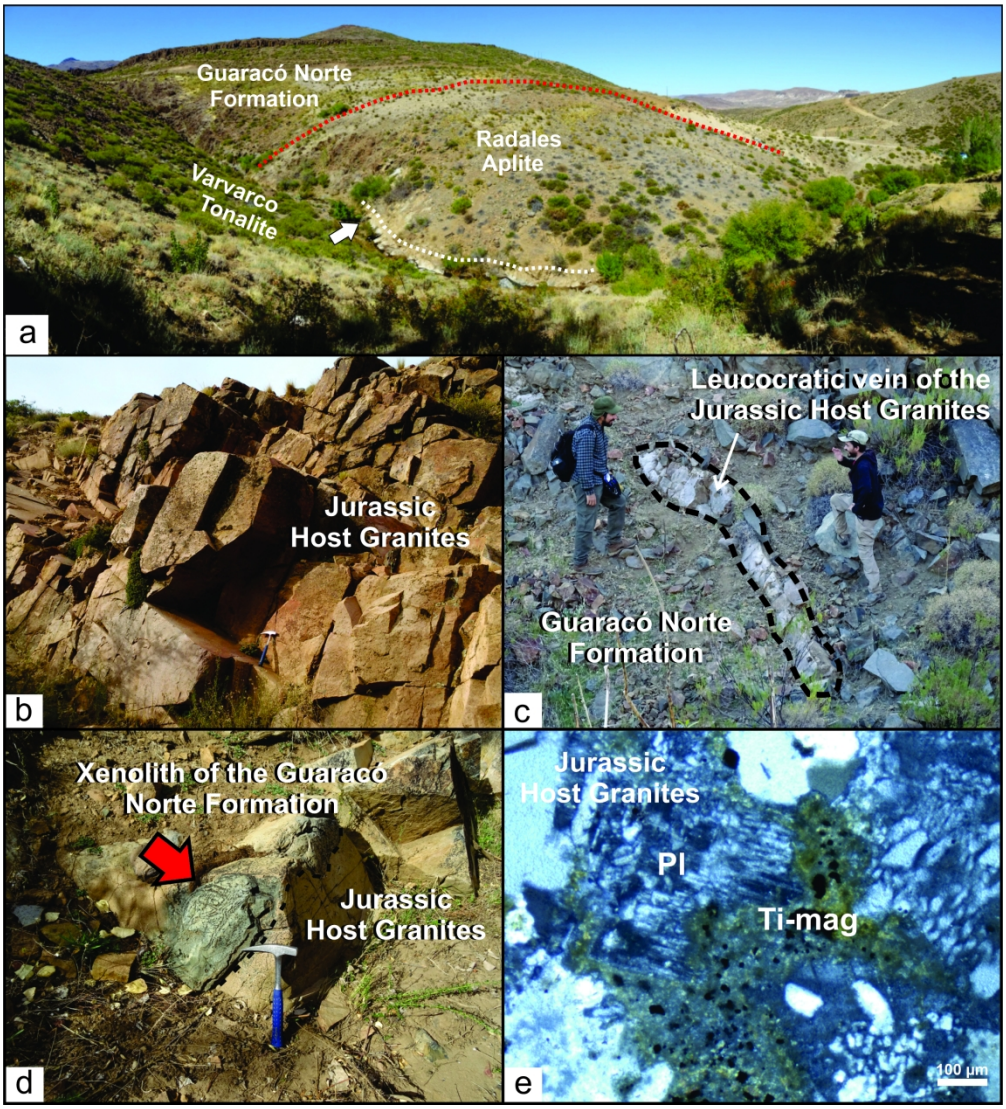

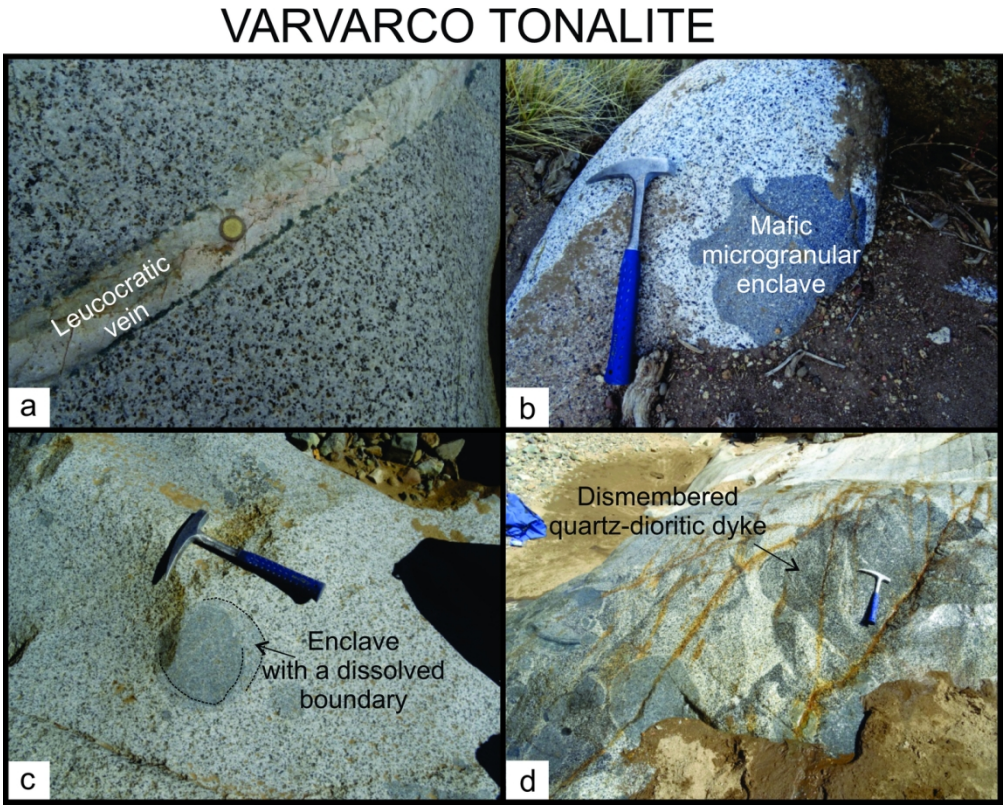

135x108mm (300 x 300 DPI)

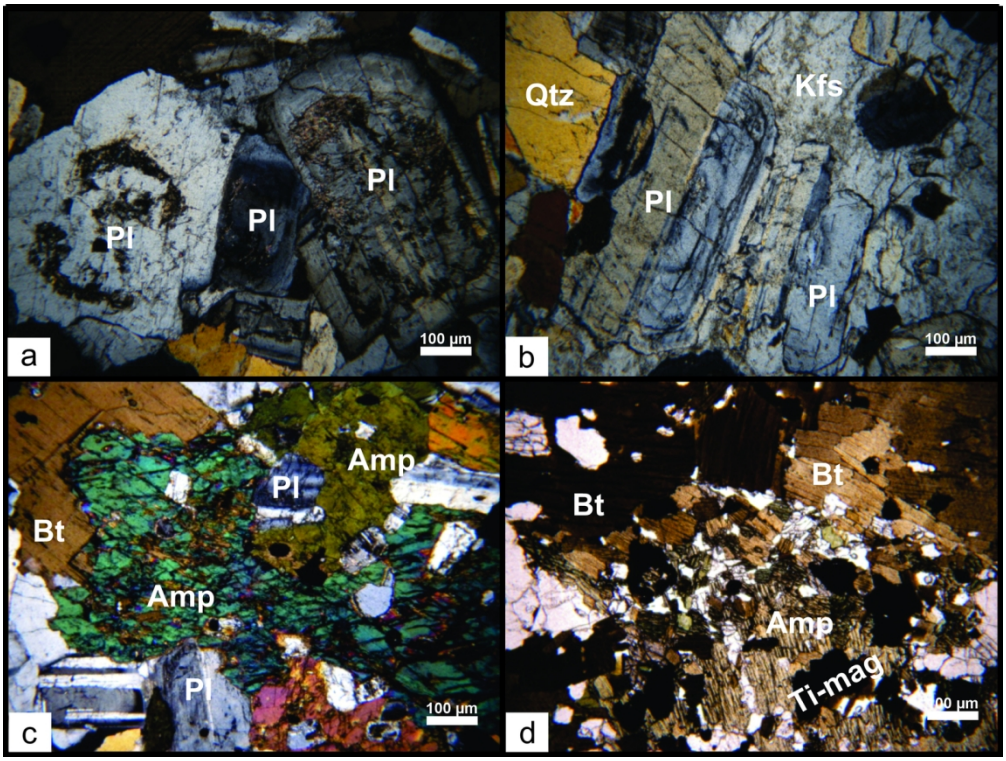

135x102mm (300 x 300 DPI)

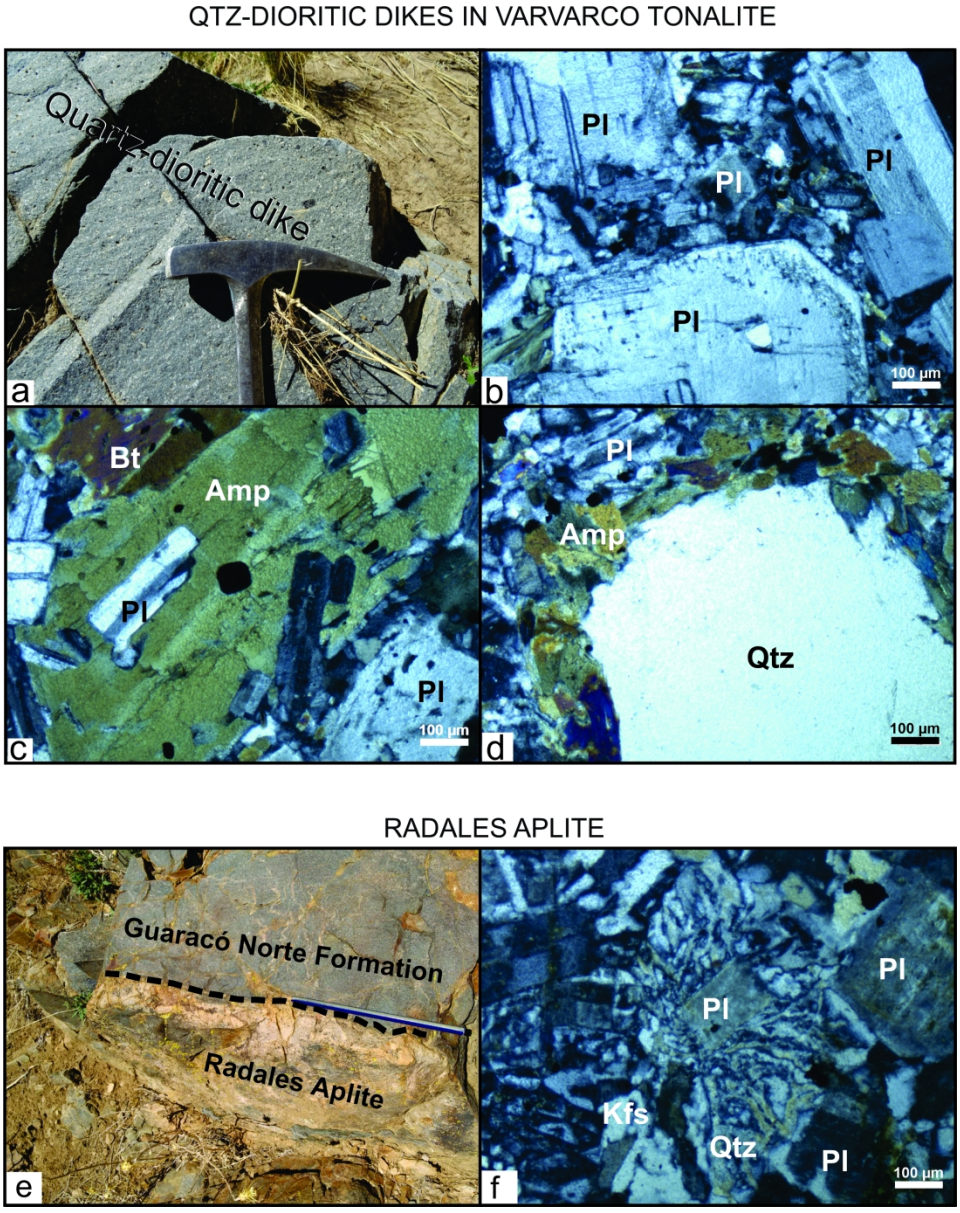
QTZ-DIORITIC DIKES IN VARVARCO TONALITE
Quartz-dioritic dike
a
Pl
Pl
Pl
Pl
100 µm
b
Bt
Amp
Pl
Pl
100 µm
c
Pl
Amp
Qtz
100 µm
d
RADALES APLITE
Guaracó Norte Formation
Radales Aplite
e
Pl
Pl
Kfs
Qtz
Pl
100 µm
f

BUTALÓN TONALITE

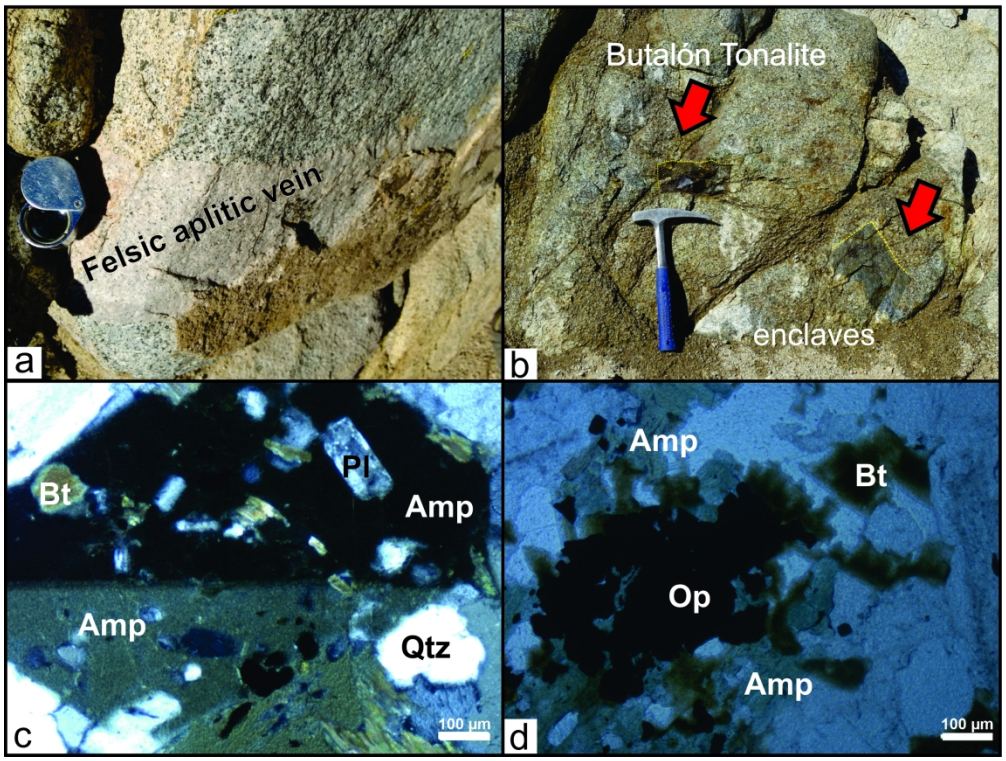

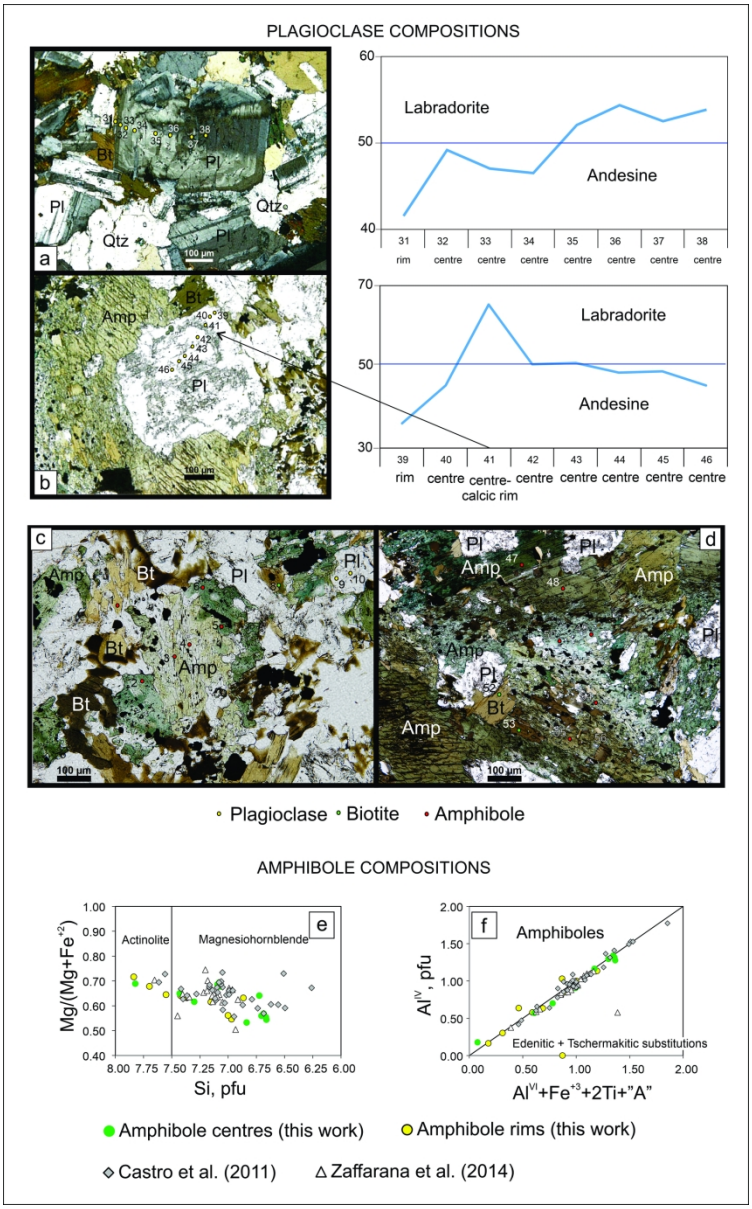

156x251mm (300 x 300 DPI)

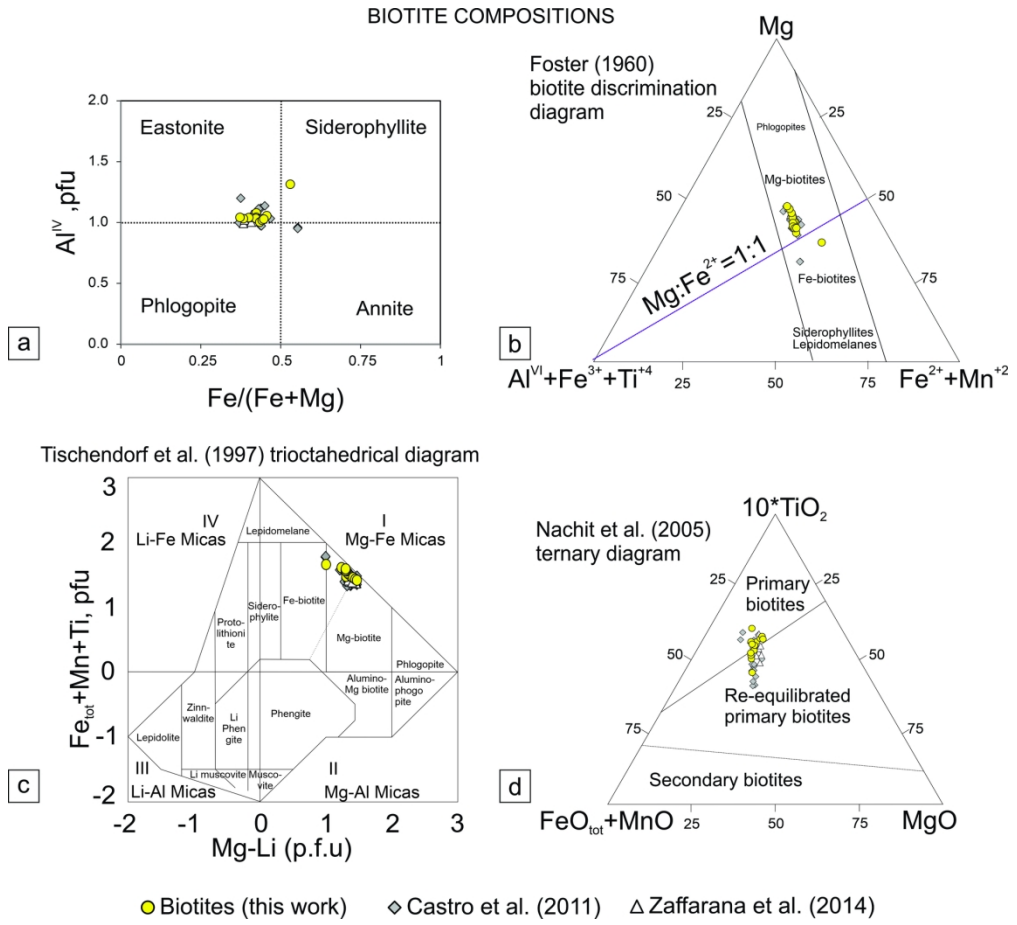

170x155mm (300 x 300 DPI)

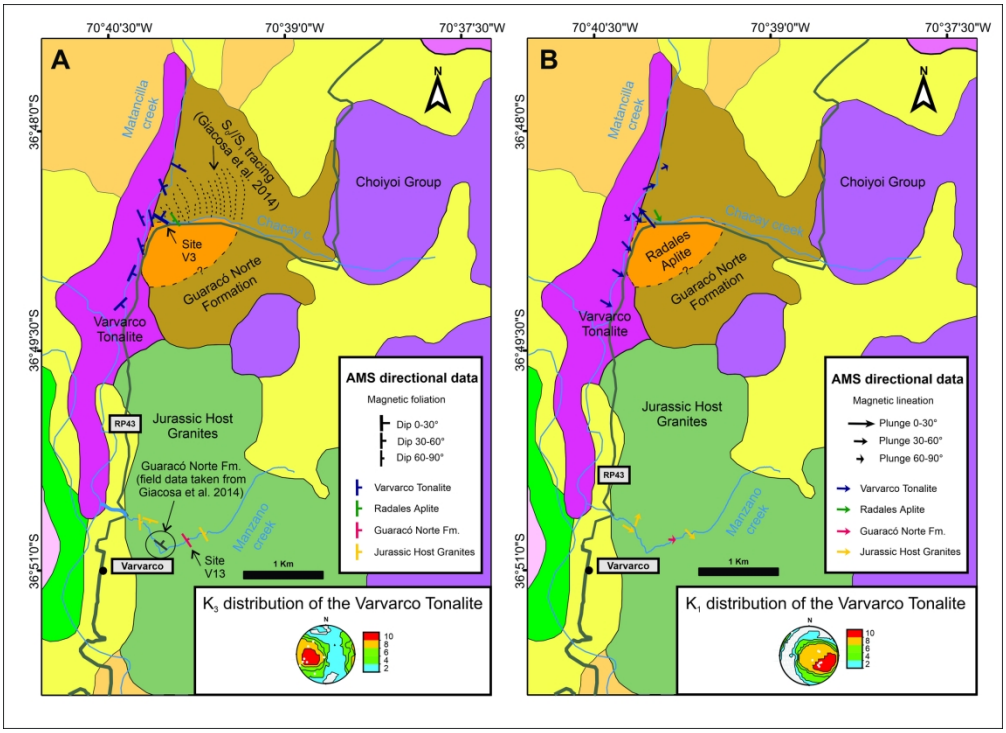

210x152mm (300 x 300 DPI)

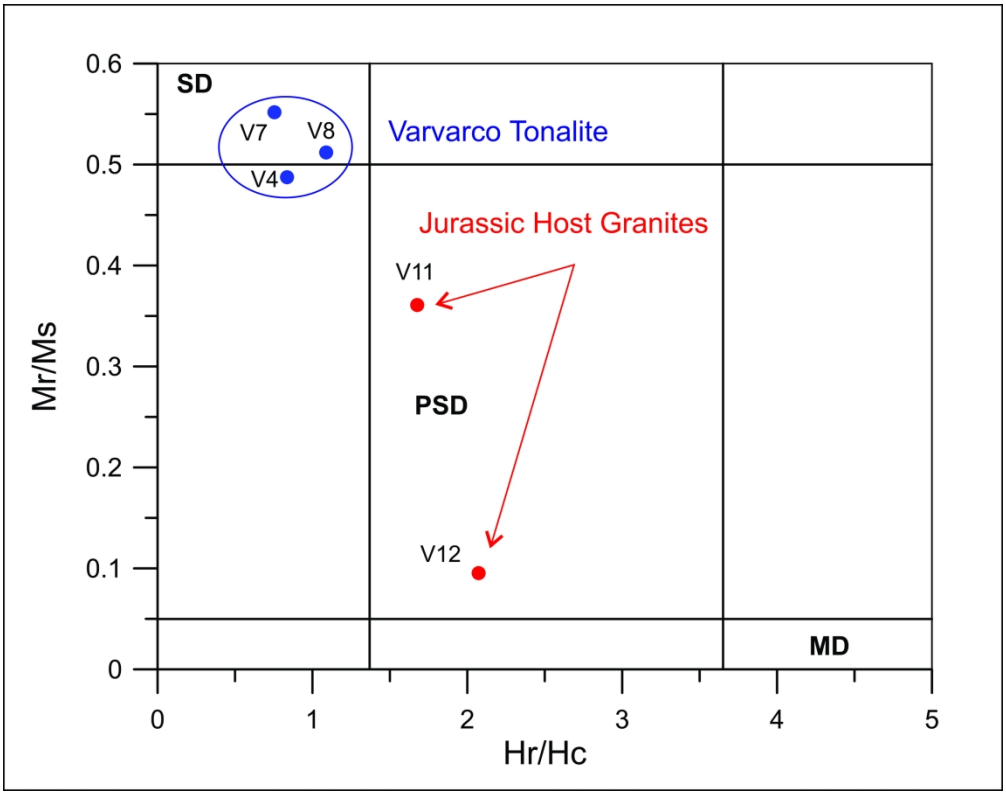

110x86mm (600 x 600 DPI)

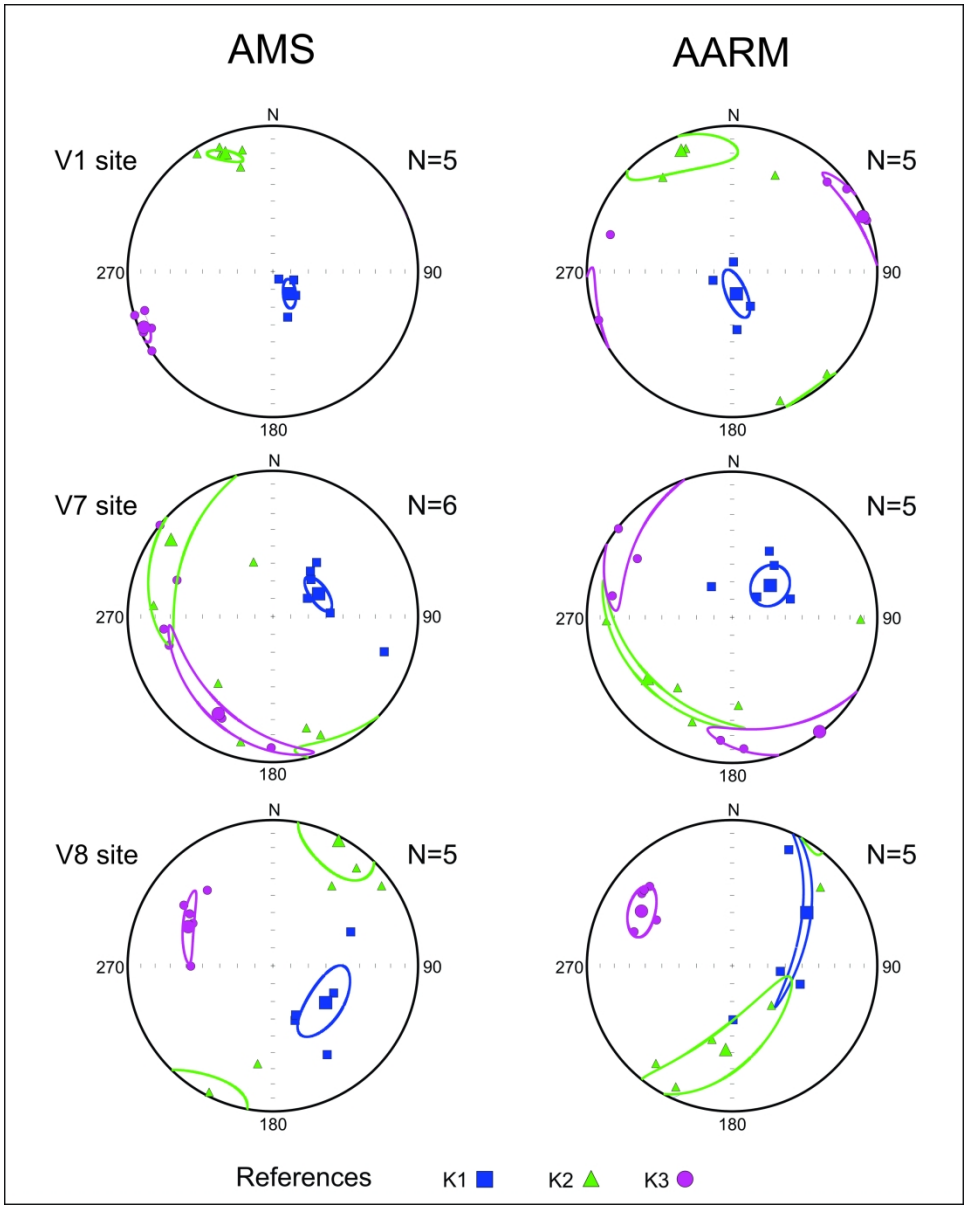

127x158mm (600 x 600 DPI)

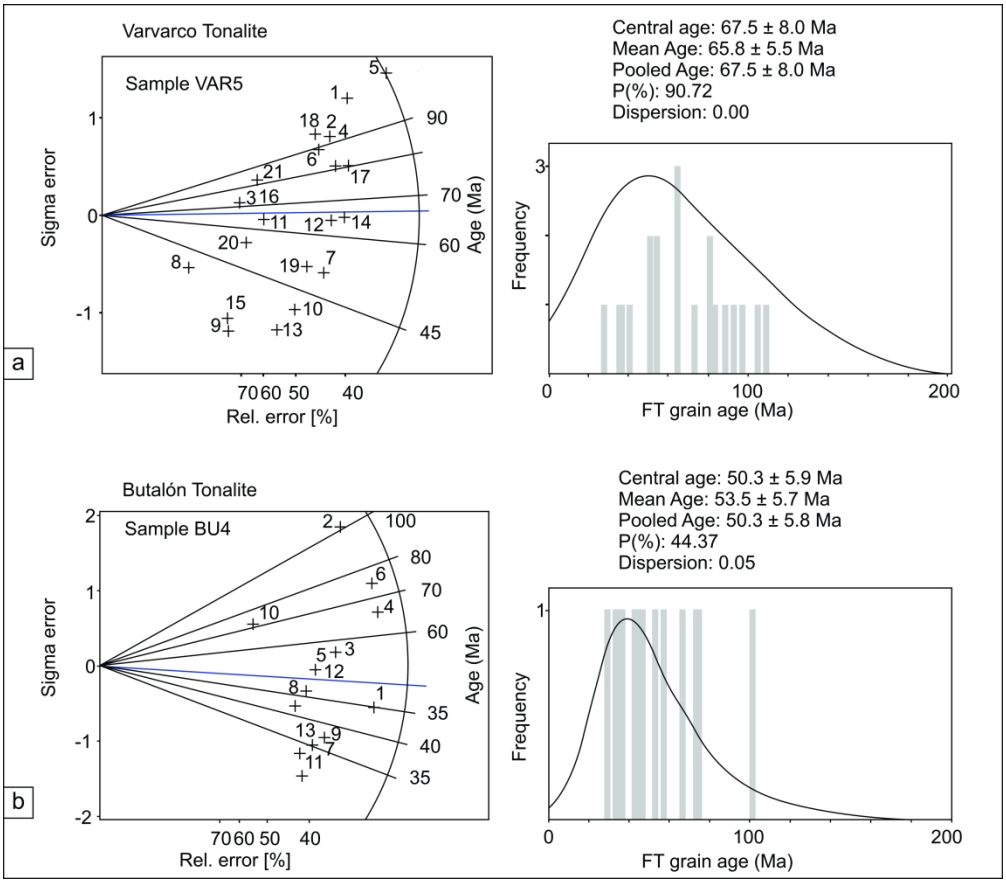

148x130mm (600 x 600 DPI)

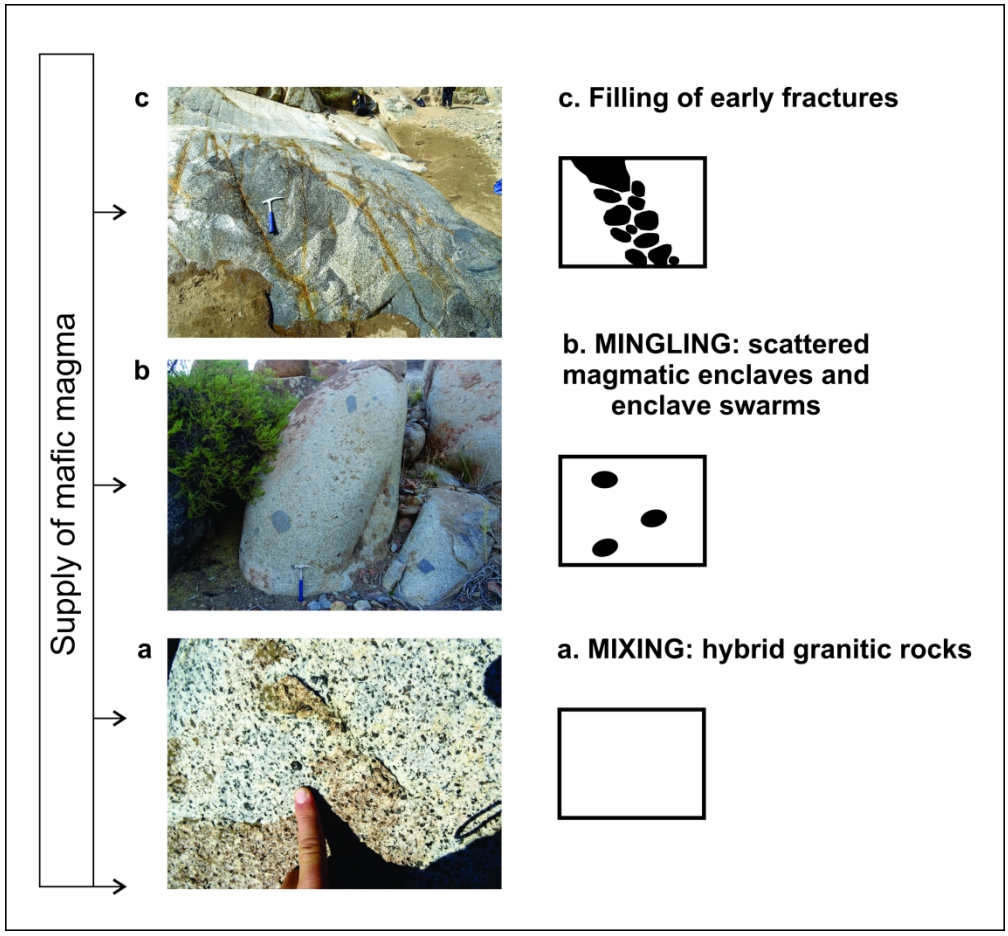

128x119mm (600 x 600 DPI)

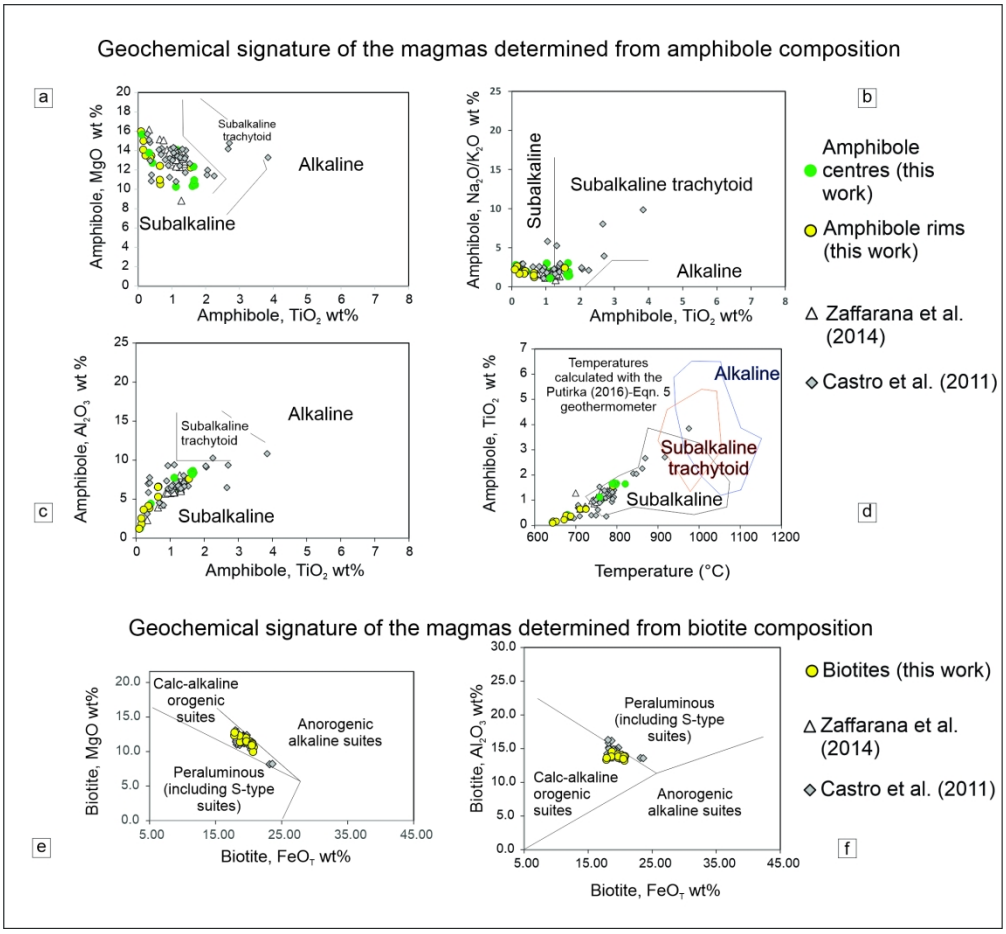
Geochemical signature of the magmas determined from amphibole composition
a
Amphibole, MgO wt %
Amphibole, TiO2 wt%
Subalkaline trachytoid
Alkaline
Subalkaline
b
Amphibole, Na2O/K2O wt %
Amphibole, TiO2 wt%
Subalkaline
Subalkaline trachytoid
Alkaline
Amphibole centres (this work)
Amphibole rims (this work)
Zaffarana et al. (2014)
Castro et al. (2011)
c
Amphibole, Al2O3 wt %
Amphibole, TiO2 wt%
Alkaline
Subalkaline trachytoid
Subalkaline
d
Amphibole, TiO2 wt %
Temperature (°C)
Temperatures calculated with the Putirka (2016)-Eqn. 5 geothermometer
Alkaline
Subalkaline trachytoid
Subalkaline
Geochemical signature of the magmas determined from biotite composition
e
Biotite, MgO wt%
Biotite, FeOT wt%
Calc-alkaline orogenic suites
Anorogenic alkaline suites
Peraluminous (including S-type suites)
f
Biotite, Al2O3 wt%
Biotite, FeOT wt%
Peraluminous (including S-type suites)
Calc-alkaline orogenic suites
Anorogenic alkaline suites
Biotites (this work)
Zaffarana et al. (2014)
Castro et al. (2011)

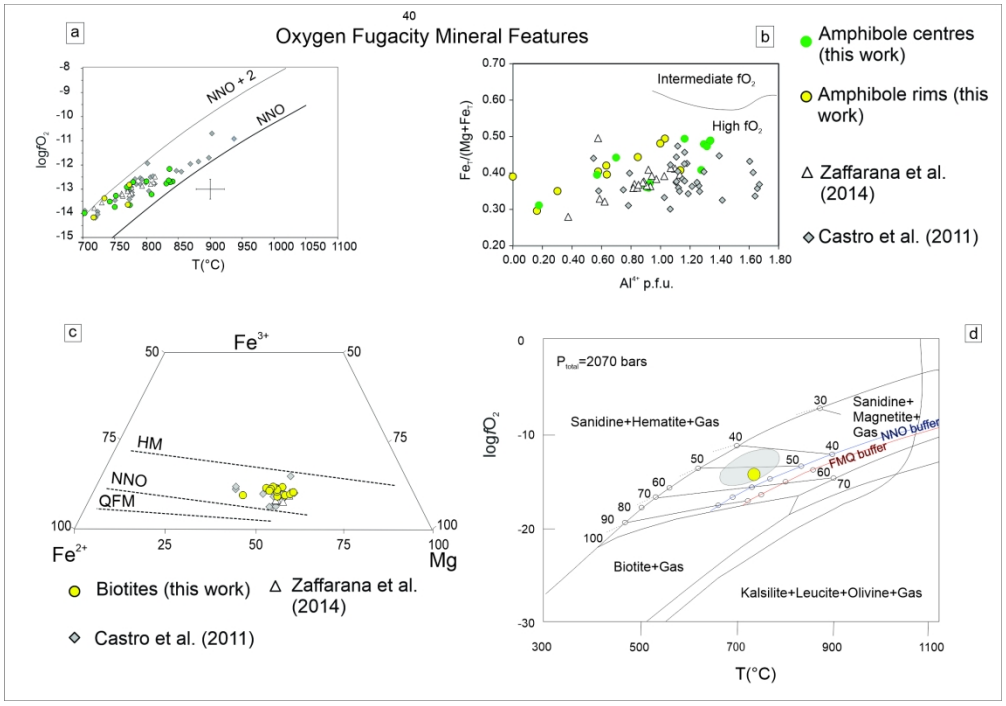
Oxygen Fugacity Mineral Features
a
b
c
d
NNO + 2
NNO
logfO2
T(°C)
Intermediate fO2
High fO2
Fe3+/(Mg+Fe2+)
Al iv p.f.u.
Amphibole centres (this work)
Amphibole rims (this work)
Zaffarana et al. (2014)
Castro et al. (2011)
Fe3+
Fe2+
Mg
HM
NNO
QFM
Biotites (this work)
Zaffarana et al. (2014)
Castro et al. (2011)
Ptotal=2070 bars
Sanidine+Hematite+Gas
Sanidine+ Magnetite+ Gas
NNO buffer
FMQ buffer
Biotite+Gas
Kalsilite+Leucite+Olivine+Gas
logfO2
T(°C)

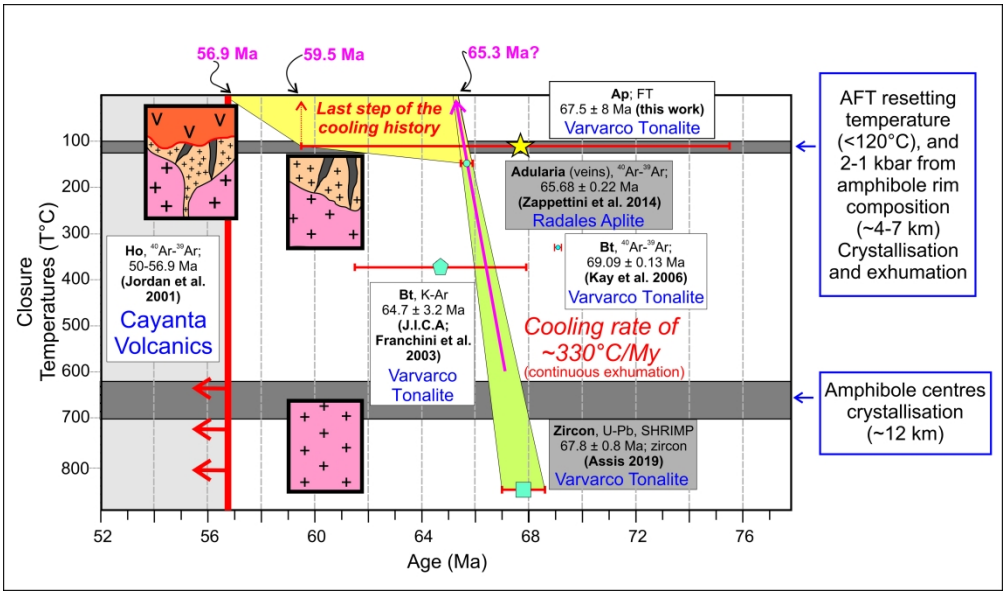

181x106mm (600 x 600 DPI)

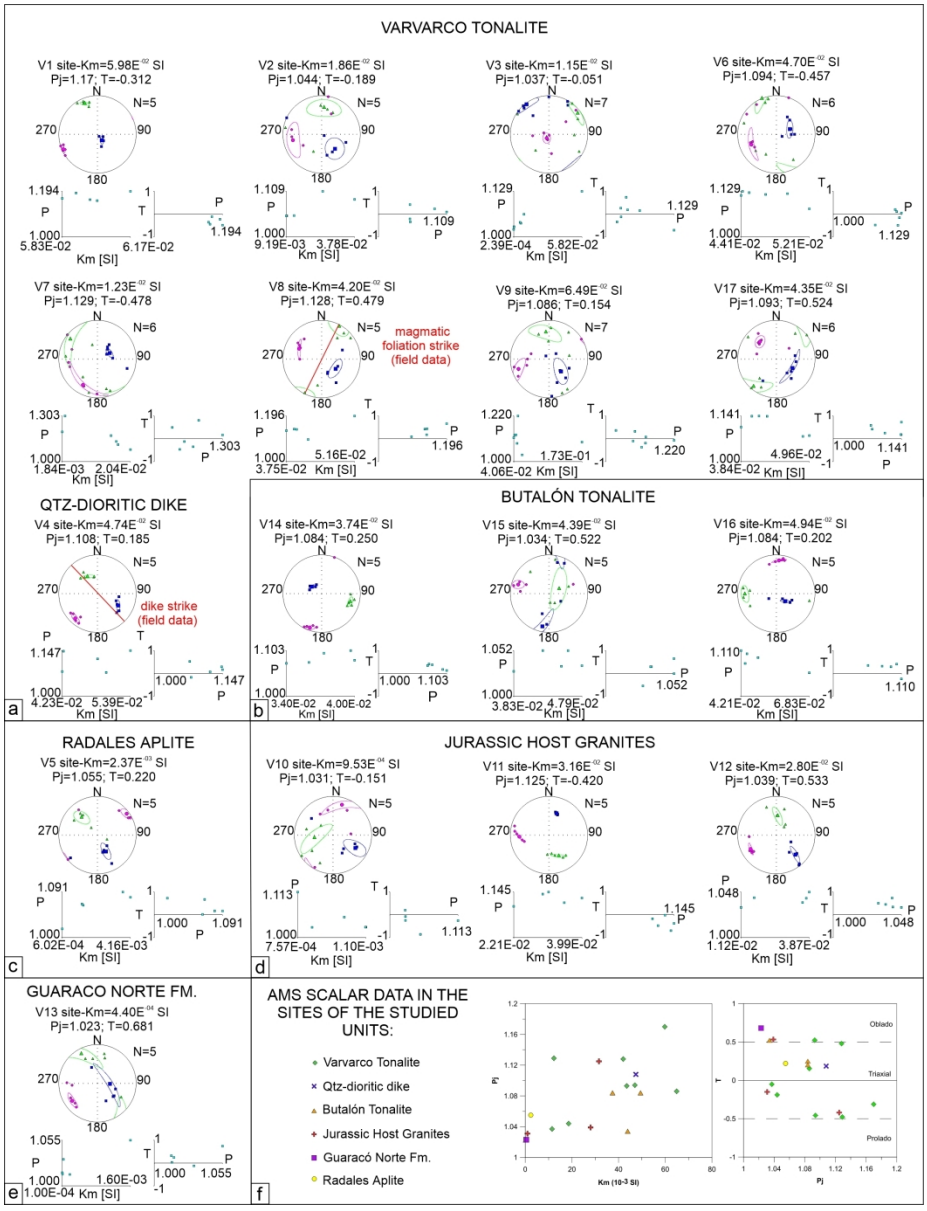

205x267mm (300 x 300 DPI)

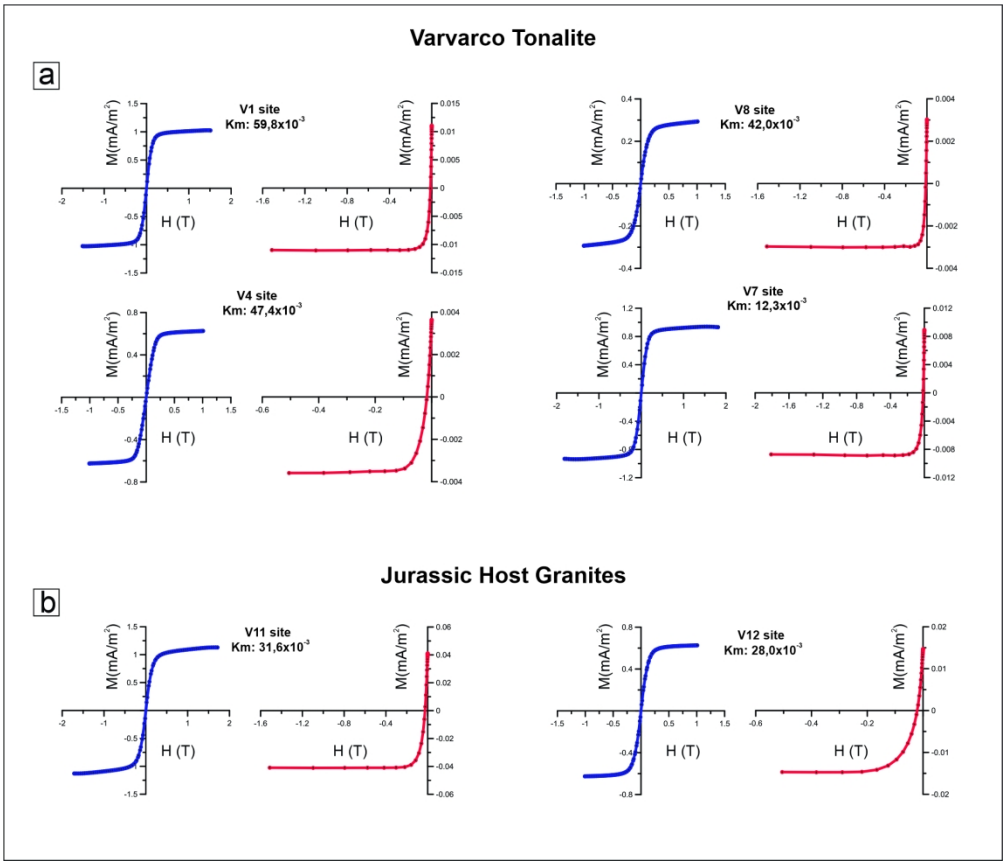

187x160mm (300 x 300 DPI)

Geological Magazine

Emplacement conditions and exhumation of the Varvarco Tonalite and associated plutons from the Cordillera del Viento, Southern Central Andes

Omar Sebastian ASSIS, Claudia Beatriz ZAFFARANA, Darío ORTS, Carla PUIGDOMENECH, Víctor RUIZ GONZÁLEZ, Gloria GALLASTEGUI, Natalia HAUSER, Ekaterina S. KISEEVA, José Francisco MOLINA and Sebastián PERNICH

Supplementary Material

Latitude (°S)	Longitude (°W)	Locality	Unit	Age	Material	Method	Source
Intrusive rocks							
36.56	71.39	Chile	Granitoid	17.73 ± 2.16	-	K-Ar	Muñoz & Niemeyer (1984)
36.71	71.64	Chile	Granitic rocks	76.5 ± 1.83	-	-	Compiled from Ramos & Folguera (2005)
36.72	71.57	Chile	Granitoid	85.4 ± 5.2	-	K-Ar	Gajardo (1981)
36.79	71.60	Chile	Granitoid	82.9 ± 3.8	-	K-Ar	Gajardo (1981)
36.82	71.51	Chile	Granitic rocks	83.9 ± 3.8	-	-	Compiled from Ramos & Folguera (2005)
36.85	70.67	Varvarco	Varvarco tonalite stock	64.7 ± 3 (K-Ar; J.I.C.A.) 69.09 ± 0.13 (^{39}Ar-^{40}Ar; Kay *et al*. 2006) 67.8 ± 0.8 (U-Pb; Assis 2019, inedit data)	whole-rock; biotite; zircon	K-Ar; ^{40}Ar-^{39}Ar; U-Pb	J.I.C.A. mentioned in Franchini *et al*. (2003); Kay *et al*. (2006); Assis (2019, unpub Thesis)
36.87	71.47	Chile	Granitoid	15.8 ± 0.3	-	K-Ar	Muñoz & Niemeyer (1984)
36.90	71.54	Chile	Granitic rocks	85.4 ± 5.2	-	-	Compiled from Ramos & Folguera (2005)
37.33	70.89	Los Maitenes	Tonalite stock	67 ± 3	whole-rock	K-Ar	Domínguez *et al*. (1984)
37.43	70.49	Co. Caicayen	Cerro Caicayen laccolith	44.7 ± 2.2	whole-rock	K-Ar	Llambías & Rapela (1989)
37.65	70.43	Cerro Del Diablo	Cerro Del Diablo laccolith	48.4 ± 2.4	whole-rock	K-Ar	Llambías & Rapela (1989)
37.70	71.72	Chile	Late Cretaceous granitic rocks	64 ± 1.9	-	-	Compiled from Ramos & Folguera (2005)
37.70	71.72	Chile	Granitoid	64 ± 1.9	-	K-Ar	Compiled from Ramos & Folguera (2005)
37.73	71.51	Chile	Late Cretaceous granitic rocks	76.5 ± 1.83	-	-	Compiled from Ramos & Folguera (2005)

37.73	71.51	Chile	Granitoid	76.5 ± 1.83	-	K-Ar	Compiled from Ramos & Folguera (2005)
37.77	70.48	Cerro Nevazón	Gabbro diorite	59.1 ± 2.9 (gabbro diorite)/56.0 ± 1.7 (diorite)/60.2 ± 1.2 (gabbro)	amphibole	^{40}Ar-^{39}Ar	Franchini *et al.* (2003)
37.77	70.33	Colipilli	Las Mellizas laccolith	49.9 ± 3.2	whole-rock	K-Ar	Llambías & Rapela (1989)
38.08	71.71	Chile	Granitoid	58 ± 4.5	-	K-Ar	Niemeyer & Muñoz (1983)
38.12	71.63	Chile	Granitoid	10 ± 1.1	-	K-Ar	Suárez & Emparan (1997)
38.12	71.41	Chile	Granitoid	63 ± 2	-	K-Ar	Suárez & Emparan (1997)
38.21	71.64	Chile	Granitoid	9.5 ± 0.7	-	K-Ar	Niemeyer & Muñoz (1983)
38.22	71.66	Chile	Granitoid	8.9 ± 1.5	-	K-Ar	Suárez & Emparan (1997)
38.22	70.62	Campana Mahuida	Hydrothermal biotite age	74.2 ± 1.4 / 60.7 ± 1.9	biotite	K-Ar	Sillitoe (1977)
38.55	71.30	Chile	Granitoid	123.3 ± 2.3	-	K-Ar	Suárez & Emparan (1997)
38.59	71.44	Chile	Granitoid	82.7 ± 1.6	-	K-Ar	Suárez & Emparan (1997)
38.63	71.38	Chile	Granitoid	53.1 ± 1.4	-	K-Ar	Suárez & Emparan (1997)
38.63	71.65	Chile	Granitoid	15.2 ± 1.2	-	K-Ar	Suárez & Emparan (1997)
38.63	71.23	Chile	Granitoid	53.1 ± 1.4	-	K-Ar	Niemeyer & Muñoz (1983)
38.70	71.28	Chile	Granitic rocks	123.2 ± 2.32	-	-	Compiled from Ramos & Folguera (2005)
38.70	71.53	Chile	Granitoid	12.3 ± 0.8	-	K-Ar	Suárez & Emparan (1997)
38.71	71.41	Chile	Granitoid	83 ± 2	-	K-Ar	Suárez & Emparan (1997)
38.71	71.47	Chile	Granitoid	108 ± 3	-	K-Ar	Suárez & Emparan (1997)
38.72	71.23	Chile	Granitoid	83.9 ± 2	-	K-Ar	Niemeyer & Muñoz (1983)
38.73	71.20	Chile	Granitoid	107 ± 1.1	-	K-Ar	Niemeyer & Muñoz (1983)
38.73	71.38	Chile	Granitoid	77.2 ± 1.1	-	K-Ar	Suárez & Emparan (1997)
38.76	71.33	Chile	Granitoid	73 ± 2	-	K-Ar	Niemeyer & Muñoz (1983)
38.77	71.48	Chile	Granitic rocks	82.66 ± 1.6	-	-	Compiled from Ramos & Folguera (2005)
38.83	71.43	Chile	Granitoid	10.7 ± 4.8	-	K-Ar	Niemeyer & Muñoz (1983)
38.84	71.24	Paso Icalma	Granodiorite	87 ± 7	amphibole	K-Ar	Latorre *et al.* (2001)

38.88	71.23	NW Aluminé Lake	Granodiorites and diorites	110 ± 4	biotite; amphibole	K-Ar	Latorre *et al*. (2001)
38.89	71.20	NW Aluminé Lake	Monzogranite	102 ± 28 / 104 ± 11 (K-Ar; Latorre *et al*. 2001) / 70.6 ± 1 / 70.8 ± 1.5 / (^{40}Ar-^{39}Ar; Gregori *et al*. 2011) 70 ± 19 (Rb-Sr; Cingolani *et al*. 1991)	biotite, amphibole, whole-rock	K-Ar; ^{40}Ar-^{39}Ar; Rb-Sr	Latorre *et al*. (2001); Gregori *et al*. (2011); Cingolani *et al*. (1991)
38.96	71.01	E Aluminé Lake	Monzogranite	108 ± 4	biotite and amphibole	K-Ar	Latorre *et al*. (2001)
Volcanic rocks							
36.86	70.44	Cerro Pelán	Naunauco Belt (andesitic sill)	81.5 ± 5	whole-rock	K-Ar	Linares (2001)
37.22	70.87	west of Andacollo	Cayanta Formation	50.3 ± 0.6 / 56.5 ± 0.6 / 56.9 ± 1.1	amphibole	^{40}Ar-^{39}Ar	Jordan *et al*. (2001)
37.99	70.34	South of Colipilli	Cayanta Formation	39 ± 9.1	amphibole	K-Ar	Llambías & Rapela (1989)
37.60	70.19	Cerro Naunauco	Cerro Naunauco andesitic laccolith	65.5 ± 0.46	amphibole	^{40}Ar-^{39}Ar	Zamora Valcarce *et al*. (2006)
37.77	70.33	Colipilli	Andesitic sill and volcanic bomb	56.64 ± 0.44 (andesitic sill) / 72.83 ± 0.83 (volcanic bomb)	plagioclase	^{40}Ar-^{39}Ar	Zamora Valcarce *et al*. (2006)

Supplementary Table S.1: Summary of the compiled ages of intrusive and volcanic rocks shown in Figure 1.

Sources for these data:

Cingolani, C., Dalla Salda, L., Hervé, F., Munizaga, F., Pankhurst, R. J., Parada, M. A., Rapela, C. W. 1991. The magmatic evolution of northern Patagonia; New impressions of pre-Andean and Andean tectonics. In *Andean Magmatism and Its Tectonic Setting* (eds R. S. Harmon & C. W. Rapela),. pp. 29–44. https://doi.org/10.1130/SPE265-p29

Domínguez, E., Aliotta, G., Garrido, M., Danieli, J. C., Ronconi, N., Casé, A. M. & Palacios, M. 1984. Los Maitenes-El Salvaje. Un sistema hidrotermal tipo porfírico. In *9º Congreso Geológico Argentino*. Actas VII. pp. 443–458.

Franchini, M., López-Escobar, L., Schalamuk, I. B. A. & Meinert, L. 2003. Magmatic characteristics of the Paleocene Cerro Nevazón region and other Late Cretaceous to Early Tertiary calc-alkaline subvolcanic to plutonic units in the Neuquén Andes, Argentina. *Journal of South American Earth Sciences* 16, 399–421. https://doi.org/10.1016/S0895-9811(03)00103-2

Gajardo, A. 1981. *Geología de la Hoja Concepción-Chillán. Escala 1:250.000. Región del Bío Bío. Mapas Geológicos Preliminares de Chile, No.4*. Instituto de investigaciones Geológicas.

Gregori, D. A., Rossi, A. & Benedini, L. 2011. Geocronología de la faja batolítica aluminé, provincia de neuquén, argentina. In *18º Congreso Geológico Argentino*, 3–4.

Jordan, T. E., Burns, W. M., Veiga, R., Pángaro, F., Copeland, P., Kelley, S. & Mpodozis, C. 2001. Extension and basin formation in the southern Andes caused by increased convergence rate: A mid-Cenozoic trigger for the Andes. *Tectonics* 20, 308–324. https://doi.org/10.1029/1999TC001181

Kay, S. M., Burns, W. M., Copeland, P. & Mancilla, O. 2006. Upper Cretaceous to Holocene magmatism and evidence for transient Miocene shallowing of the Andean subduction zone under the northern Neuquén Basin. In *Evolution of an Andean Margin: A Tectonic and Magmatic View from the Andes to the Neuquén Basin (35°-39°S Lat)*, pp. 19-60. Geological Society of America. https://doi.org/10.1130/2006.2407(02)

Latorre, C. O., Vattuone, M. E., Linares, E. & Leal, P. R. 2001. K-Ar ages of rocks from Lago Aluminé, Rucachoroi and Quillen, North Patagonian Andes, Neuquén, República Argentina. In *3º South American Symposium on Isotope Geology*, pp. 577–580. Pucon.

Linares, E. 2001. *Catálogo de edades radimétricas de la República Argentina. Parte I: Años 1957–1988. Parte II: Años 1988–2000*. Publicaciones de la Asociación Geológica Argentina. Serie F (Publicaciones en CD), N81, Buenos Aires.

Llambías, E. J. & Rapela, C. W. 1989. Las volcanitas de Collipilli, Neuquén (37ºS) y su relación con otras unidades paleógenas de la cordillera. *Revista de la Asociación Geológica Argentina* 44, 224–236.

Muñoz, J. & Niemeyer, H. 1984. *Hoja Laguna del Maule*. Servicio Nacional de Geología y Minería. Carta Geológica de Chile, No.64.

Niemeyer, H. & Muñoz, J.1983. *Hoja Laguna de La Laja, región del Bío-Bío. Escala 1:250.000*. Servicio Nacional de Geología y Minería. Carta Geológica de Chile, No.57.

Ramos, V. A. & Folguera, A. 2005. Tectonic evolution of the Andes of Neuquén: constraints derived from the magmatic arc and foreland deformation. *Geological Society, London, Special Publications* 252, 15–35. https://doi.org/10.1144/GSL.SP.2005.252.01.02

Sillitoe, R. H. 1977. Permo-Carboniferous, upper Cretaceous, and Miocene porphyry copper-type mineralization in the Argentinian Andes. *Economic Geology* 72, 99–103.

Suárez, M. & Emparan, C. 1997. *Hoja Curacautín, Regiones de la Araucanía y del Biobío*. Servicio Nacional de Geología y Minería. Carta Geológica de Chile, No.71, 105p., 1 mapa 1:250.000 (made by Emparan, C., Suárez, M. and Muñoz, J. 1992).

Zamora Valcarce, G., Zapata, T., del Pino, D. & Ansa, A. 2006. Structural evolution and magmatic characteristics of the Agrio fold-and-thrust belt. In *Evolution of an Andean Margin: A Tectonic and Magmatic View from the Andes to the Neuque´n Basin (35°-39°S Lat)*, pp. 125–145. Geological Society of America. https://doi.org/10.1130/2006.2407(06)